UPWELLING AND CROSS-SHELF TRANSPORT DYNAMICS ALONG THE PACIFIC EASTERN BOUNDARY

A Thesis
Presented to
The Academic Faculty

by

Vincent Combes

In Partial Fulfillment
of the Requirements for the Degree
Doctor of Philosophy in the
Earth and Atmospheric Sciences

Georgia Institute of Technology
August 2010

UPWELLING AND CROSS-SHELF TRANSPORT DYNAMICS ALONG THE PACIFIC EASTERN BOUNDARY

Approved by:

Dr. Emanuele Di Lorenzo,
Committee Chair
Earth and Atmospheric Sciences
Georgia Institute of Technology

Dr. Emanuele Di Lorenzo, Advisor
Earth and Atmospheric Sciences
Georgia Institute of Technology

Dr. Annalisa Bracco
Earth and Atmospheric Sciences
Georgia Institute of Technology

Dr. Judith A. Curry
Earth and Atmospheric Sciences
Georgia Institute of Technology

Dr. Jean Lynch-Stieglitz
Earth and Atmospheric Sciences
Georgia Institute of Technology

Dr. Kevin Haas
Civil and Environmental Engineering
Georgia Institute of Technology

Date Approved: July 2, 2010

ACKNOWLEDGEMENTS

It is a pleasure to thank the people who made this thesis possible.

It is difficult to overstate my gratitude to my Ph.D. supervisor, Dr. Emanuele Di Lorenzo. His enthusiasm, encouragement, and guidance had motivated me to pursue in the field of physical oceanography. He did become more than an advisor. I can not thank him enough for his trust by allowing me to live one year in Chile. That year, spent collaborating with Chilean researchers from the Universidad de Concepcion, had totally changed my life. Therefore, I also want to thank the entire "departamento de geofisica" for its hearty welcome. More specifically, the collaboration with Dr Samuel Hormazabal and Dr Carolina Parada has been an incredible opportunity for me and for my career. No doubt that I will maintain that special scientific and personal link with them. I would also like to thank the entire research group of my advisor and Dr Annalisa Bracco for providing a stimulating and fun environment.

I wish to thank all the colombians friends, all the salsa dancers from Chile and salsa dancers from Atlanta for making my PhD years unforgettable. A particular thanks to Sara Vieira for being both a 6-years EAS friend and for being a perfect salsa partner. I do not forget the fun moments spent with Jessica Hernandez, Anna Fidler and Nashiely Pineda.

I also would like to thank Olivier Cazeaux and Robin Durant for reasons that will be too long too enumerate.

Finally, "merci Papa, merci Maman et merci Seb". It is very difficult for me to summarize in few words all they brought to my life and how i am indebted to them for their support, their love and all the rest ... To them I dedicate this thesis.

TABLE OF CONTENTS

LIST OF TABLES

LIST OF FIGURES

SUMMARY

The Upwelling and Cross-shelf Transport Dynamics along the Pacific Eastern Boundary is explored using a high resolution ocean model for the last 60 years. Three ocean circulations have been modeled. From North to South, we investigate the dynamics of the Gulf of Alaska (GOA), the Califonia Current System (CCS) and the Humboldt Current System (HCS, also known as the Peru-Chile Current System, PCCS). Each region is studied separately and appear respectively in chapter 3,4 and 5.

The marine ecosystem of the Gulf of Alaska (GOA) is very rich despite a open ocean characterized by high nutrient and low-chlorophyll-a concentration. Recent observational studies suggest that advection of iron-rich coastal water is the primary mechanism controlling open ocean productivity. Specifically there is evidence that mesoscale eddies along the coastal GOA entrain iron-rich coastal waters into the ocean interior. Chapter 3 investigates the cross-shelf transport statistics in the GOA over the period 1965-2004. The statistics of coastal waters transport are computed using a model passive tracer, which is continuously released at the coast and at the surface. The passive tracer can thus be considered a proxy for coastal biogeochemical quantities such as silicate, nitrate, iron or oxygen, which are critical for explaining the GOA ecosystem dynamics. On average along the Alaska Current, we find that at the surface while the advection of tracers by the average flow is directed towards the coast consistent with the dominant downwelling regime of the GOA, it is the mean eddy fluxes that contribute to offshore advection into the gyre interior. South of the Alaskan Peninsula, both the advection of tracers by the average flow and the

mean eddy fluxes contribute to the mean offshore advection. On interannual and longer timescales, the offshore transport of the passive tracer in the Alaskan Stream does not correlate with large scale atmospheric forcing, nor with local winds (intrinsic vairiability). In contrast in the Alaska Current region (forced variability), stronger offshore transport of the passive tracer coincides with periods of stronger downwelling (in particular during positive phases of the Pacific Decadal Oscillation), which trigger the development of stronger eddies.

We investigate the low-frequency variability in the transport (cross-shore and alongshore) of coastal water masses in the Central and Southern California Current System (CCS) over the period 1950-2008. As for the GOA, our approach consists of an ensemble of passive tracers released in the numerical model to characterize the effects of linear (Ekman upwelling) and non-linear (eddy activity) circulation regimes on the statistic of low frequency advection of coastal waters in the central and southern CCS. By looking at the passive tracer concentration distribution, we find that the low-frequency upwelling and the surface offshore transport of the upwelled nutrient-rich coastal water are strongly correlated with the alongshore wind stress, and is coherent between the central and southern CCS. The offshore transport of the surface coastal water is nevertheless not coherent between those two regions, and has been found to be associated with mesoscale eddy activity, where both surface and subsurface waters propagate offshore mainly through cyclonic eddies. Our results also show that the poleward California Under Current, at about 200m depth, affects the alongshore transport and provides rich waters to the Central California dominant upwelling cell.

The Humboldt Current System (HCS) is the one of the world's most productive regions in fish landings, providing $\sim 20\%$ of the world marine catches despite covering less than 1% of the world's ocean surface. This high productivity results principally from the upwelling of nutrient-rich water in the photic zone. The similar

passive tracer approach is used to characterize the upwelling dynamics and offshore transport of coastal water masses. Different model experiments are conducted to explore the sensitivity of the HCS upwelling to different air-sea fluxes of momentum and atmospheric and oceanic teleconnections to ENSO. On average, we find that the model runs forced by ECMWF wind stress compare better with observations than the experiment forced by NCEP wind stress, with strong upwelling off Peru (5°S-16°S) and central Chile (27°S-34°S) and significantly weaker upwelling in the North Chile Region (18°S-24°S). Temporal variability is nevertheless well reproduced by NCEP, when comparing model and in situ coastal sea surface height anomaly data. There is evidence, in this region, that both changes in surface wind and coastally trapped Kelvin waves control the variability of the coastal upwelling. The effect of ocean remote forcing is assessed by comparing the output of two model simulations which does and does not include the presence of waves at their boundaries. The passive tracer approach indicates that, off the coast of Peru, the El *Niño* Southern Oscillation (ENSO) strongly modulates the strength of coastal upwelling principally due to the propagation of downwelling equatorial Kelvin waves (particularly strong during El *Niño* years) rather than changes in local wind stress. The Central Chile region is also found to be very sensitive to Kelvin waves generated at the equator, considerably reducing the upwelling during strong El *Niño* events. In addition to the upwelling variability, this study investigates the offshore transport of the coastal waters of South America. While the surface offshore transport of upwelled water is modulated by ENSO, mesoscale eddies and filaments also play an important role in the offshore transport of both the surface and subsurface coastal waters. Our results indicate that while cyclonic eddies mostly transport coastal waters in the surface layer, both cyclonic and anticyclonic eddies transport coastal waters in the subsurface.

The passive tracer experiments, performed in this study in the GOA, CCS, and HCS, therefore could provide a dynamical framework to understand the dynamics

of the upwelling/downwelling and offshore transport of nutrient rich coastal water and to interpret how it responds to atmospheric forcing. This also could reinforce our interpretation (and therefore predictions) in the changes in vertical and offshore advection of other important biogeochemical quantities, essential in understanding the Californian ecosystem variability.

CHAPTER I

INTRODUCTION

Eastern boundary currents (EBCs) in subtropical regions are usually considered separately from the gyre-scale circulation (basin-wide), due to their unique and separate dynamics. The EBCs are commonly known as the Canary Current (North Atlantic), the Benguela Current (South Atlantic), the Humboldt Current (South Pacific) and the most studied California Current (North Pacific). The four EBCs share a same equatorward, narrow, shallow and generally extremely eddy-rich characteristics. Near the shore, equatorward winds (trade winds) produce a shallow offshore surface Ekman flow, which get replaced by deep, cold nutrient-rich water, full of dissolved organics matter. This phenomenon, usually known as Ekman coastal upwelling, strongly impacts ecosystems. Indeed upwelling stimulates and supports the marine ecosystem (fig 1.1) from the base of the food web, by enhancing the availability of nutrient in the photic zone, thus encouraging the growth of phytoplankton. Grazers such as krill and copepods are then attracted by this supply of phytoplankton. At the top of the food chain, larger predators will also respond to the change of the lower trophic levels. Satellites can even captures such upwelling regions, through the spatial structure of the sea surface temperature (colder) and chlorophyll (higher concentration) fields.

Figure 1.2a shows a model sea surface temperature (SST; from a 10km resolution global ocean model, described in section 2.4) for April 2007. The low SST, off the coasts of California, Peru-Chile, Canary Islands and the west coast of South Africa, clearly shows the surface signature of the four upwelling cells that bring deep cold coastal waters to the surface. Superimposed on the SST field, figure 1.2a shows a dominant equatorward surface wind stress, driving the upwelling. In addition to
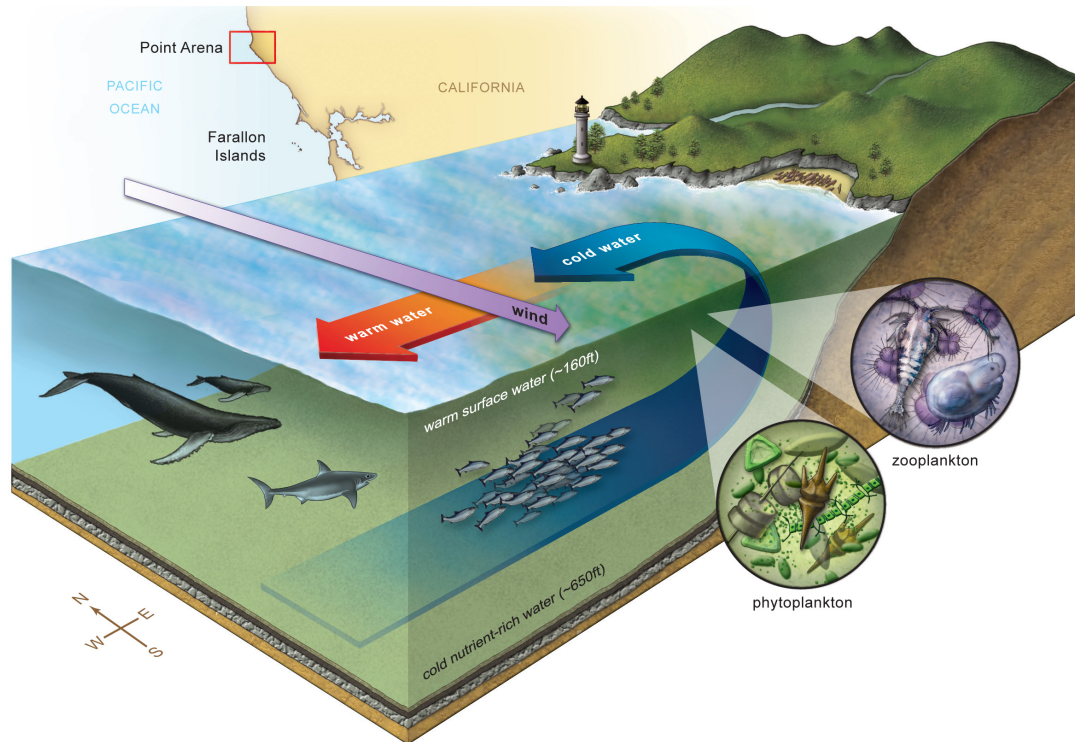
Figure 1.1: Upwelling Illustration by Fiona Martin ©2006

the variability of the coastal surface wind, the water column stratification, coastal topography, and latitude-dependence of the Coriolis parameter also play an important role in the characteristics of the upwelling (Chavez and Messie, 2009 [16]). The satellite chlorophyll-a on figure 1.2b shows spatial similarities with the SST field, in particular in the EBCs regions. The chlorophyll-a field also gives an indication of the high productivity of those EBCs regions, maintained by the advection of the nutrient-rich deep waters to the photic zone.

Another feature of the EBCs is the year-round presence of a subsurface poleward flow (∼200m depth off Chile). Some of its characteristics include a more saline and lower oxygen concentration core than the surrounding waters. This feature, as we will see for the Humboldt Current System (Peru-Chile) and California current system (CCS), plays an important role in the transport (mixing) between low latitudes and high latitudes. More specifically, chapter 5 (chapter 4) will show that a part of the upwelled waters off Central Chile (Northern California) are originated from

the subsurface waters off the coast of Peru (Central California). The dynamics and variability of the poleward flow in EBCs are however poorly understood.

History has shown drastic changes of the ecosystems in the EBCs, significantly impacting the economy and fisheries industry. Some examples include a migration of cold-living Peruvian anchovy to the cooler Chilean waters during strong El *Niño* events and a collapse of the sardine populations off the California coast in the 1950s. Following those tremendous changes, a sampling program of the physical and biological properties off the coast of southern California (the California Cooperative Oceanic Fisheries Investigation; CalCOFI) now provides us a unique long-term (1949-present) hydrographic dataset. Those in-situ data allow a better understanding of the coastal ocean variability and changes in biogeochemical quantities off California. Off the Peruvian coast, no such program has yet been funded, despite that the size of the productive habitat and primary productivity are considerably reduced during El *Niño* years (Chavez and Messie, 2009 [16]). The deepening of the thermocline, during those events, makes the surface waters warm and nutrient poor, impacting the distribution of species. However on average, the upwelling in that region, which occurs throughout most of the year, provides to the country of Peru one of the world's largest marine fisheries for sardines and anchovies.

Motivated by the fact that history show that upwelling dynamics highly impact coastal productivity, the present dissertation characterizes the interannual upwelling fluctuations, both off the coast of California and the coast of Peru-Chile. Not only does our study looks at the coastal upwelling variability, but it also looks at the offshore propagation of the nutrient-rich coastal upwelled waters, important in the mixing/transport of biogeochemical quantities to the open ocean. In addition to the EBCs of the HCS and CCS, this dissertation also presents a physical description of the Gulf of Alaska (GOA) ocean dynamics. The marine ecosystem of the GOA is very rich despite a open ocean characterized by high nutrient and low-chlorophyll-a

concentration and a coastal downwelling condition. Common to the three studied regions, this study will show the importance of mesoscale eddies (cyclonic and/or anticylonic) in the cross-shore exchange of coastal water masses. The eddy transport statistics are however different between the HCS, the CCS and the GOA.

A more detailed introduction for each region is provided in chapters 3-5. The dissertation is organized as followed. Chapter 2 describes the ocean model (the Regional Ocean Modelling System; ROMS) and forcing, used in this study. Chapters 3, 4 and 5 investigate the coastal dynamics and offshore transport variability of coastal water masses respectively in the Gulf of Alaska, the California Current System and the Peru-Chile Current System. Finally, each chapter will characterize separately the effects of mesoscale eddies in the offshore transport of coastal water masses.

Chapter 3, on the GOA dynamics, is a combination of the published articles Combes, V. and Di Lorenzo, E., 'Intrinsic and forced interannual variability of the gulf of alaska mesoscale circulation', Progress in Oceanography, vol. 75, no. 2, pp. 266-286, 2007 and Combes, V., Di Lorenzo, E., and Curchitser, E., 'Interannual and decadal variations in cross-shelf transport in the gulf of alaska', Journal of Physical Oceanography, vol. 39, no. 4, pp. 1050-1059, 2009.

Chapter 4, on the HCS dynamics, has been submitted in full as Combes, V., Di Lorenzo, E., Gmez, F., Hormazabal, S., Strub, T.P., Putrasahan, D., Sasaki, H., Taguchi, B. and Sasai, Y., 'Modeling Interannual and Decadal variability in the Humboldt Current upwelling system', submitted to Journal of Physical Oceanography, 2010.

Chapter 5, on the CCS dynamics, has been submitted in full as Combes, V., Chenillat, F., Di Lorenzo, E., Rivire, P., Ohman, M., N. and S. J. Bograd, 'Cross-shore transport variability in the California Current System: Ekman Upwelling vs. Eddy Regime', 2010.
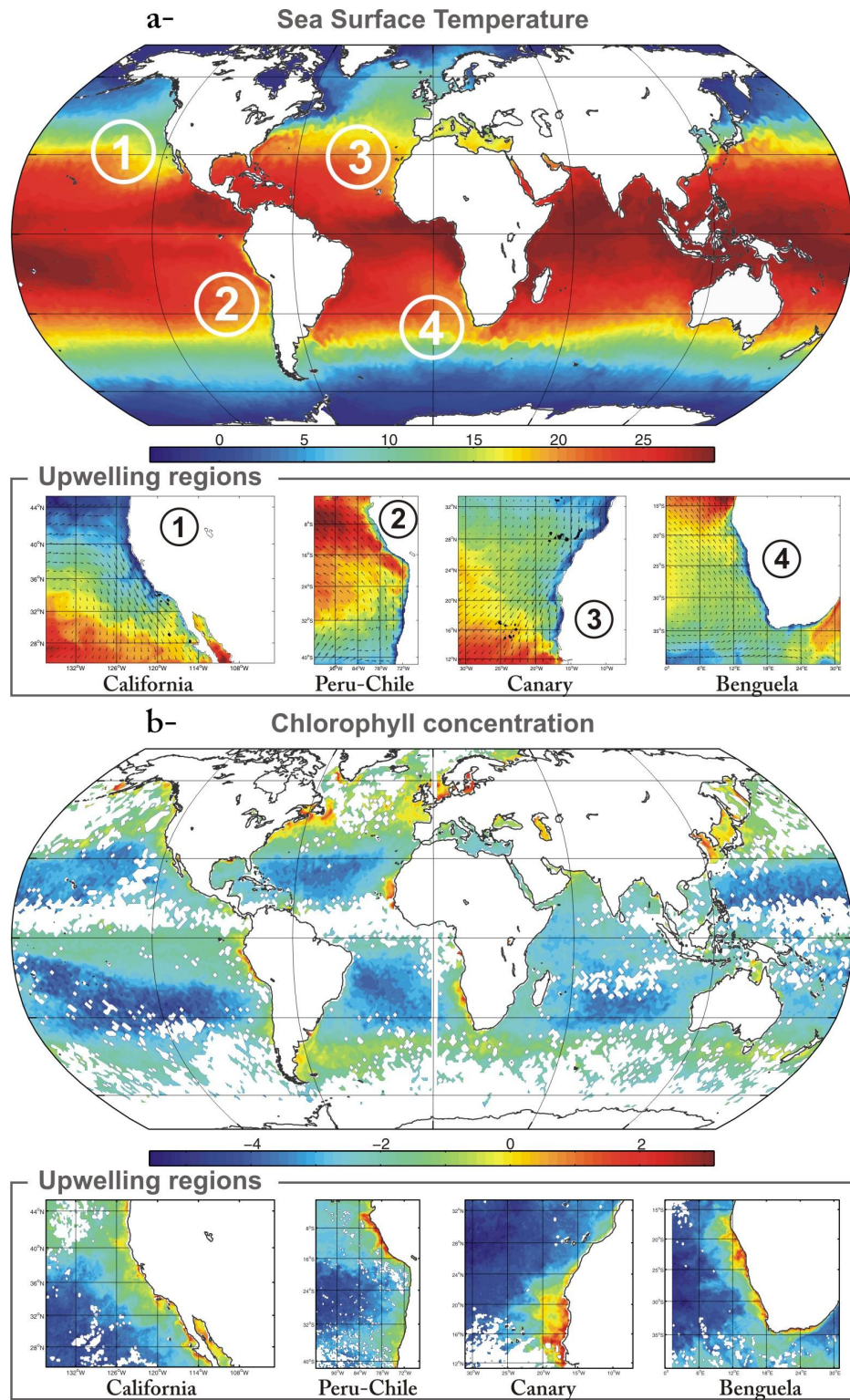
Figure 1.2: (a) model (Ocean Model for the Earth Simulator) sea surface temperature and (b) chlorophyll-a concentration for April 2007

CHAPTER II

THE REGIONAL OCEAN MODELLING SYSTEM (ROMS)

2.1 *Model formulation*

This chapter briefly describes the Regional Ocean Modelling System (ROMS), used throughout this dissertation to characterize the dynamics of the GOA, CCS and HCS.

The primitive equations (respectively the momentum balance, the evolution of temperature and salinity, the equation of state, the hydrostatic approximation and the continuity equation) in Cartesian coordinates (x,y,z) are written as followed:

$$\frac{\partial u}{\partial t} + \vec{v} \cdot \nabla u - fv = -\frac{\partial \phi}{\partial x} + F_u + D_u$$

$$\frac{\partial v}{\partial t} + \vec{v} \cdot \nabla v + fu = -\frac{\partial \phi}{\partial y} + F_v + D_v$$

$$\frac{\partial T}{\partial t} + \vec{v} \cdot \nabla T = F_T + D_T$$

$$\frac{\partial S}{\partial t} + \vec{v} \cdot \nabla S = F_S + D_S$$

$$\rho = \rho(T, S, P)$$

$$\frac{\partial \phi}{\partial z} = -\frac{\rho g}{\rho_o}$$

$$\frac{\partial u}{\partial x} + \frac{\partial v}{\partial y} + \frac{\partial w}{\partial z} = 0$$

where (u, v, w) are the 3D velocity components, T the potential temperature, S the salinity, ρ the density, ϕ the dynamic pressure, f the Coriolis parameter, g the acceleration of gravity, D the diffusive terms and F the forcing terms.

ROMS (Haidvogel et al., 2000 [36]; Shchepetkin and McWilliams, 2005 [86]), a descendent of the S-Coordinates Rutgers University Model (SCRUM), is a three dimensional, free-surface, hydrostatic, eddy-resolving primitive equation ocean model. The model employs orthogonal curvilinear coordinates in the horizontal and terrain-following coordinates (also know as σ-coordinates) in the vertical with higher resolution at the surface. The vertical coordinate is described in on section 2.2. The primitive equations are solved using a split-explicit time-stepping scheme, which allows the separation of the barotropic and baroclinic components of the momentum equations with internal and external time steps. Some model configuration options include a KPP scheme for vertical mixing in the surface boundary (Large et al., 1994 [51]) and implicit horizontal mixing associated with the third order upstream bias scheme (Shchepetkin and McWilliams, 1998 [85]). A complete report of the model numerics, open boundary conditions and mixed layer parameterizations can be found in Shchepetkin and McWilliams (1998) [85] and Large et al. (1994) [51].

Previous studies have already used ROMS successfully to simulate eastern boundary systems (California Current System: Di Lorenzo et al., 2005 [29]; Benguela System: Penven et al., 2001 [75]; Peru System: Penven et al., 2005 [74]). Figure 2.1 shows the regional domains (white boxes) where the ROMS physical ocean model has been applied during my PhD. The simulations, discussed in that dissertation, are labeled on the figure 2.1 GOAN, NEPD, CCS, PCCS and PCCS-WEST. The specific model configurations for each of those regions will be discussed in their corresponding sections. Experiments conducted on the Kuroshio - Oyashio Extension (KOE) and on the Mediterranean sea (MED) are available on the Georgia Tech Ocean and Climate Data Server (currently hosted on http://www.o3d.org/datatemp/), but not analyzed in this study.
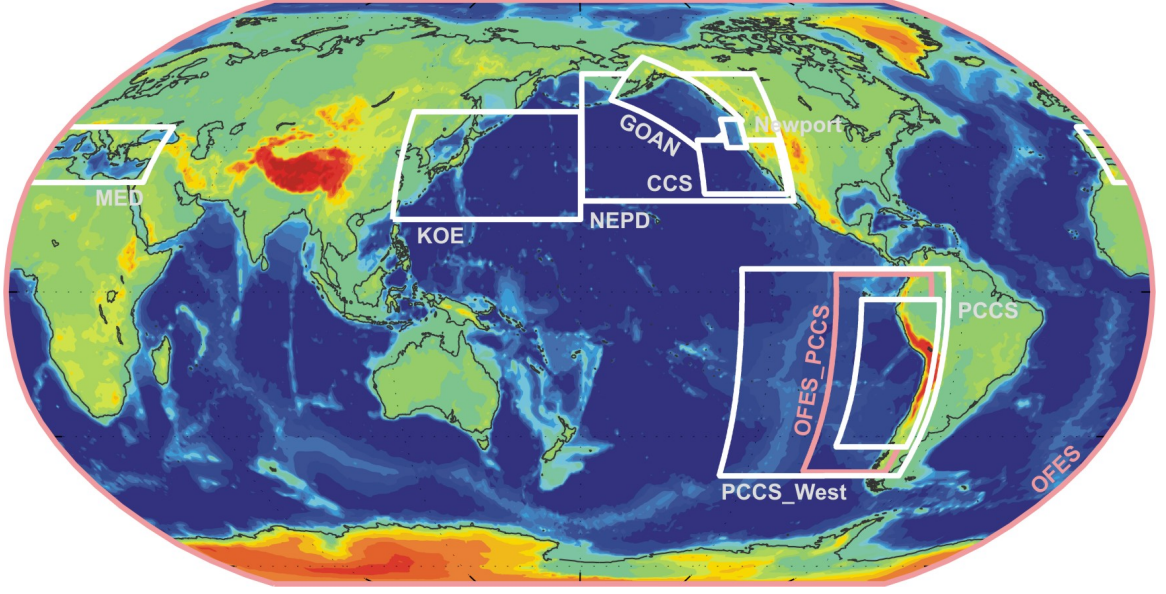
Figure 2.1: Depiction of regions of experiments using the ROMS model (white boxes), along with regions were OFES output is available (pink boxes).

2.2   The σ-coordinates system

In ROMS, the primitive equations are discretized in the vertical on σ-coordinates, also known as 'terrain-following coordinates'. As in Song and Haidvogel (1994) [90], the change of coordinates from cartesian to σ-coordinates (-1 $\leq \sigma \leq$ 0) is written as followed:

$$z = \zeta(1+s) + h_c\sigma + (h - h_c)C(\sigma)$$

$$C(\sigma) = (1 - \theta_b)\frac{sinh(\theta_s\sigma)}{sinh(\theta_s)} + \theta_b\frac{tanh[\theta_s(\sigma + \frac{1}{2})] - tanh(\frac{1}{2}\theta_s)}{2tanh(\frac{1}{2}\theta_s)}$$

where we choose to have more resolution above h$_c$. From the equation above, characteristics of the σ-coordinates include: $\sigma = 0$ for z = ζ(x,y) = sea surface height, σ = -1 for z = h(x,y) = bottom bathymetry and the higher the value of θ_s (θ_b), the more resolution is apply at the surface (bottom). Figure 2.2 illustrates two σ-surfaces configurations, one with higher resolution at the surface (θ_s, θ_b)=(7,1) and one with a uniform resolution in the vertical (θ_s,θ_b)=(0.001,0). In the model simulations, presented throughout the dissertation, we generally use $\theta_s = 5$ and θ
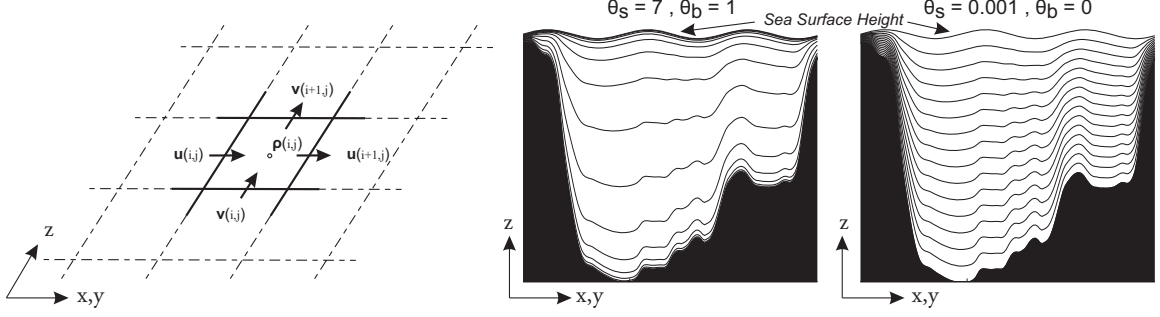
Figure 2.2: ROMS Arakawa C grid and two examples of σ-surfaces with (θ_s, θ_b)=(7,1) and (θ_s, θ_b)=(0.001,0)

$_b = 0.4$, in order to resolve better the ocean dynamics over the mixed layer (with $h_c \sim 10$m).

Using the transformation $\frac{\partial}{\partial z} = \frac{1}{H_z}\frac{\partial}{\partial s}$ (where H_z(x,y,s) represents the thickness of the σ-surfaces), the vertical boundary conditions are given by:

at the surface, σ=0	at the bottom, σ=-1
$\left(\frac{\nu}{H_z}\right)\frac{\partial u}{\partial s} = \tau_s^x(x,y,t)$	$\left(\frac{\nu}{H_z}\right)\frac{\partial u}{\partial s} = \tau_b^x(x,y,t)$
$\left(\frac{\nu}{H_z}\right)\frac{\partial v}{\partial s} = \tau_s^y(x,y,t)$	$\left(\frac{\nu}{H_z}\right)\frac{\partial v}{\partial s} = \tau_b^y(x,y,t)$
$\left(\frac{K_T}{H_z}\right)\frac{\partial T}{\partial s} = \frac{Q_T}{\rho_o c_p} + \frac{1}{\rho_o c_p}\frac{dQ_T}{dT}(T - T_{ref})$	$\left(\frac{K_T}{H_z}\right)\frac{\partial T}{\partial s} = 0$
$\left(\frac{K_S}{H_z}\right)\frac{\partial S}{\partial s} = \frac{(E-P)S}{\rho_o}$	$\left(\frac{K_S}{H_z}\right)\frac{\partial S}{\partial s} = 0$
$\Omega = 0$	$\Omega = 0$

where $\tau_s^{x,y}$ and $\tau_b^{x,y}$ are the surface wind stress and bottom stress, Q_T the surface heat flux and $E - P$ the evaporation minus precipitation (surface water flux). In particular, this transformation is clearly very convenient in the computation of the vertical velocity Ω (while in the z coordinate it is written as $w = \frac{\partial \zeta}{\partial t}$ and $w + \vec{v}\cdot\nabla h = 0$). Surface forcings (i.e. fresh water fluxes, heat fluxes and wind stress) used in the model simulations are listed in the next section.

2.3 Surface Forcings

For the surface fluxes and momentum stress, our model experiments have been forced by data from three sources: the National Center for Environmental Prediction/National Center for Atmospheric Research reanalysis (NCEP/NCAR), the European Centre for Medium-Range Weather Forecasts (ECMWF) and QuikSCAT satellite (QSCAT).

The NCEP/NCAR reanalysis provide a 60-years record of atmospheric fields. This global data assimilation combines data from land surface, ship, aircraft and satellite. A complete description can be found in the NCEP/NCAR 40-year Reanlysis project from Kalnay et al., 1996 [44]. This data set will provide to our studies the wind stress, surface heat fluxes, short wave radiation and surface water fluxes (in the form of Evaporation minus Precipitation) fields from 1950 to 2007. The native resolution of the data is on a 2.5^o x 2.5^o grid, which presents non-negligible coastal differences when compared directly with satellite-retrieved data. However, comparisons with coastal in-situ data will show (in chapters 3-5) that the interannual variability of the SSH is well reproduced.

The ERA-40 is a re-analysis of meteorological observations from September 1957 to August 2002 produced by the ECMWF. As in NCEP/NCAR, the observations used in ERA-40 were accumulated from many sources. Uppala et al., 2005 [101] gives a detailed description of the available observational data, including their time and spatial coverages. Uppala et al., 2005 [101] also describes the data assimilation system used for ERA-40. This data set will provide us the 1^ox1^o surface wind stress driving the ocean model for the HCS. In particular, major differences with the NCEP/NCAR wind stress can be observed along the Pacific coast of South America. The impact of these differences on the ocean dynamics will be discussed on chapter 5.

Finally, SeaWinds on QuikSCAT derives the wind stress from measuring backscatter from the ocean surface (http://podaac.jpl.nasa.gov/DATA_CATALOG/ quikscat-info.html) on a 0.5^ox0.5^o grid, providing a more accurate and realistic coastal wind stress. A blended version (QSCAT observations and NCEP analyses) has been used. According to http://www.cora.nwra.com/~morzel/blendedwinds.qscat.ncep.html, 'it creates global fields by retaining QSCAT wind retrievals in swath regions, and in the unsampled regions (between swaths and in data gaps) augmenting the low-wavenumber NCEP fields with a high-wavenumber component that is derived from monthly regional QSCAT statistics'. Compared to the 60-years data from NCEP / NCAR, the QSCAT time range (September 1999 - Present), is less appropriated in the discussion of the interannual ocean variability, and also misses the strong El *Niño* events in 1982-83 and 1997-98. Most of the model experiments performed in that dissertation were therefore forced with time-dependent surface wind stress from NCEP/NCAR or ECMWF.

2.4 Boundary Forcings

The 3-Dimensions physical variables (temperature, salinity and velocities), needed for model boundary forcings, were mainly provided by the World Ocean Atlas (WOA), by the Simple Ocean Data Assimilation (SODA) or by the Ocean Model for the Earth Simulator (OFES).

The WOA (Levitus et al., 1994 [54]) consists of a climatology of global fields of in situ ocean properties (including ocean temperature, salinity, dissolved oxygen, phosphate, nitrate, ...). Those variables are available on a 1^ox1^o spatial resolution with 33 vertical levels. Because the ocean velocities are not provided, the components of the ocean currents will be derived from temperature and salinity, assuming the flow geostrophic (this data set therefore cannot be used at lower latitudes).

For model domains that would include an open boundary at lower latitudes, an

alternative to the WOA is SODA. SODA consists of a reconstruction of historical global ocean climate variability for sea surface height, temperature, salinity and ocean currents. The methodology is described by Carton et al., 2000 [14].

The Ocean Model for the Earth Simulator (OFES; Masumoto et al., 2004 [62], Sasaki et al., 2004 [83], Sasaki et al., 2006 [82]) is an eddy-resolving global ocean model that covers 75° S to 75° N with a 0.1^o (10km) horizontal resolution with 54 vertical levels. A 50-year spin-up run was performed using climatological mean forcing from NCEP/NCAR and restoring conditions to observed temperature and salinity fields from the World Ocean Atlas (WOA). Following the spin-up, the model has been forced by daily mean heat and salinity fluxes from the NCEP/NCAR reanalysis. Two integrations of the model are available, driven either by daily mean wind stress forcing of NCEP/NCAR reanalysis (from 1950 to 2007) or by daily mean QSCAT (from 1999 to 2007). The OFES output will be used for the open boundary forcings and initial condition for the ROMS experiments. The OFES model also includes a simple nitrogen-based Nitrogen-Phytoplankton-Zooplanton-Detritus (NPZD) pelagic model (Oschlies, 2001). NPZD model initialization and spinup are described in Sasai et al, 2006 [81]). This would also be an alternative way from WOA to provide boundary and stable initial condition for future ROMS-NPZD experiments.

2.5   A passive tracer approach

A passive tracer approach has been chosen to illustrate the cross-shelf transport dynamics along the Pacific eastern boundary. The transport pathways and statistics associated in particular with the mesoscale circulation are characterized using a passive tracer advection-diffusion equation with a decay term.

$$\frac{\partial P}{\partial t} + \underline{u} \cdot \nabla P = A_H \nabla_H^2 P + \frac{\partial}{\partial z}\left(A_V \frac{\partial P}{\partial z}\right) - \frac{P}{\tau} + Q(x, y, z)$$

where P is the passive tracer concentration (no unit), A_H the horizontal diffusivity set to 5 $m^2 s^{-1}$ (however, no analyses on the sensitivity of that value has been made),

A_V the vertical diffusivity obtained by a KPP scheme (large et al, 1994 [51]), Q a time independent source term and τ is the decay timescale. The decay term is introduced to track the transport patterns of the passive tracer from its source within the timescale set by τ. This term is needed to avoid an infinite growth of passive tracer concentrations in the model domain interior. The timescale τ is set from 1-4 years, depending on the region of study (GOA, CCS, HCS). The source term is set to 1 along the coast. We choose to release the tracer continuously in the surface layer for the GOA (mainly coastal downwelling condition) but in the subsurface for the CCS and PCCS in order to also quantify the strength of the coastal upwelling of those regions. A precise description of the regions where tracer has been injected is provided in each chapter corresponding to each Pacific eastern boundary.

CHAPTER III

THE GULF OF ALASKA (GOA) CIRCULATION

3.1 Introduction

Observational and modeling studies suggest that decadal-scale variability in the Gulf of Alaska (GOA) gyre circulation is strongly controlled by changes in the atmospheric forcing (Lagerloef, 1995 [49]; Cummins and Lagerloef, 2004 [27]). Decadal and inter-annual variability in wind stress over the GOA is correlated with the Pacific Decadal Oscillation (PDO) and the Southern Oscillation. Intensification of the Aleutian low during 1976/77, also referred to as the climate shift (Miller et al., 1994 [68]) modified the surface ocean circulation of the GOA (Capotondi et al., 2005 [13]; Miller et al., 2005 [69]). More specifically, Miller et al. (2005) [69] suggest that an intensification of the Alaskan Stream occurred after the 1976/77 climate shift, although the Alaska Current and eddies generated on the eastern GOA remain mostly unchanged. In addition to local changes in surface winds, coastally trapped Kelvin waves generated in the tropics during the El *Niño* Southern Oscillation (ENSO) affect the GOA circulation (Meyers and Basu, 1999 [67]).

Despite the numerous observational studies over the northeast Pacific Ocean (Meyers and Basu, 1999 [67]; Crawford, 2002 [23]; Strub and James, 2002 [94]; Brickley and Thomas, 2004 [11]; Ladd et al., 2005 [47]), important aspects of the GOA dynamics (e.g., mesoscale activity) have been rarely studied or modeled, and thus are not well understood. Some modelers have nevertheless focused their studies on mesoscale circulation in the GOA, such as Haida or Sitka eddies (Melsom et al., 1999 [66]; Di Lorenzo et al., 2005a [28]). Okkonen et al. (2001) [72] have also suggested that eddy

variability is dominated by the local response to wind forcing along the Alaska Current (eastern GOA basin) and is non-deterministic in the Alaskan Stream (western GOA basin).

Eddies in the GOA have already been studied for several decades using available observations (Tabata, 1982 [97]). In the eastern GOA basin, three major groups of eddies have been identified according to the location of their formation, Yakutat, Sitka and Haida (Fig 3.1). These three eddy groups share common features, such as an anti-cyclonic rotation (up to 0.4 m sea surface height anomaly) with a warmer and less saline core above 100 m depth. (Tabata, 1982 [97]; Crawford, 2002 [23]). The generation and migration of these eddies, which can survive for more than three years, is well documented in satellite observations (Thomson and Gower, 1998 [99]; Crawford, 2002 [23]). Haida and Sitka eddies mostly propagate offshore while the Yakutat eddies propagate alongshore along the Alaskan Stream. While previous studies attribute the generation of these large eddies to baroclinic instability of the coastal currents (Thomson and Gower, 1998 [99]; Murray et al., 2001 [70]), a more recent numerical investigation by Di Lorenzo et al. (2005a) [28] suggests that the most southern eddy, the Haida eddy, can develop without instabilities by simple advection of buoyant water masses around Cape St. James (southern tip of Queen Charlotte Island). These advected water masses generate patches of buoyant flow with anticyclonic circulation which merge to generate larger eddies when the flow around the cape is strong. For the more northern Sitka and Yakutat eddies a more detailed modeling study of their formation has not been completed.

In addition to the eddies developed in the eastern boundary along the Canadian coast, the western basin (here defined as west of 150 W) also exhibits enhanced eddy activity. Along the Alaskan Stream, eddies have been both observed (Crawford et al., 2000 [26]) and modeled (Okkonen et al., 2001 [72]) and tend to propagate southwestward along the Aleutian peninsula. In the Shelikof sea valley (north GOA basin)
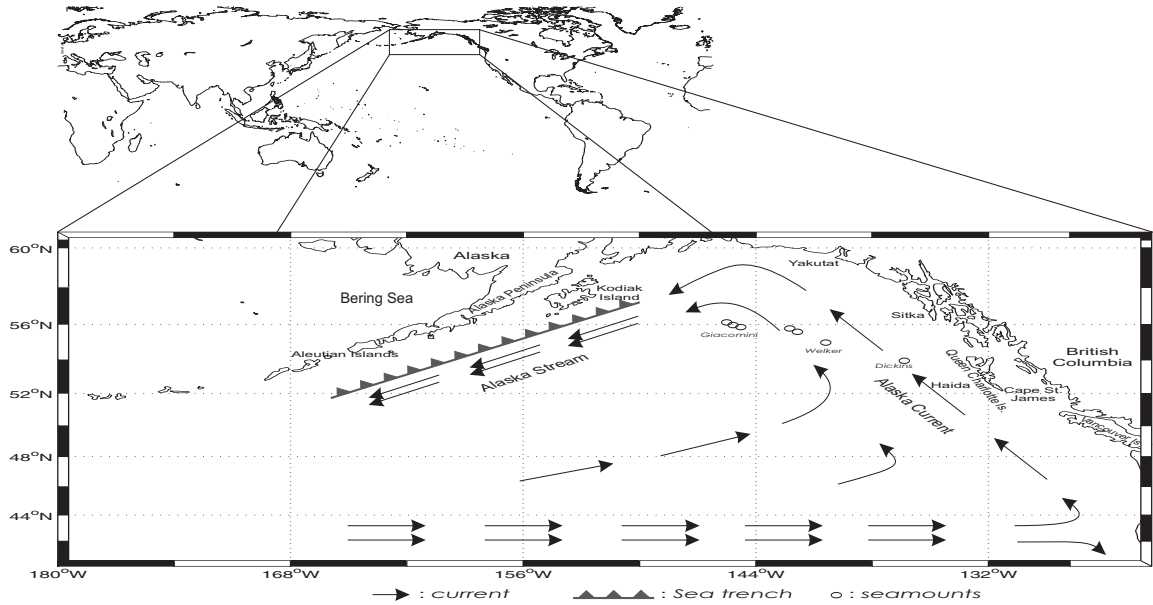
Figure 3.1: Map of the domain (Gulf of Alaska: GOA)

Stabeno and Hermann (1996) [93] find a good agreement between eddies generated by a model and observations, however their study does not diagnose the eddy dynamics.

Understanding the dynamics of eddies and other mesoscale physical processes is critical for predicting how tracer exchanges between inshore and offshore water masses will respond to changes in atmospheric and ocean state (e.g. ENSO, PDO, global climate change). Eddies have several direct implications on the climate and biology of the GOA, because of their important role in cross-shelf transport. A recent study suggest that about 35-60% of northward heat transport during winter is carried offshore by the Haida eddies (Crawford, 2005 [24]). Crawford (2005) [24] estimates that 15% of the total river freshwater input between the Columbian River and 54N is transported by these eddies. Nutrient exchanges (Whitney and Robert, 2002 [104]; Ladd et al., 2005 [47]) and iron transport (Johnson et al., 2005 [43]) also occur vertically in the core of eddies. The eddy induced transport is also linked to the biological productivity in the offshore high nutrient low Chlorophyll-a (HNLC) waters of the Alaskan gyre (Crawford et al., in press). Links between eddy transport, water mass properties and biota have also been reported in the GOA western basin (Okkonen et al., 2003 [73])

16

and eastern basin (Mackas and Galbraith, 2002 [57]). At the higher trophic levels the link between mesoscale processes and species distributions/abundance has not been fully established. However fish communities have been found to respond strongly to large-scale atmospheric changes, such as the 1976/77 climate shift (Mantua et al., 1997 [58]; Litzow et al., 2006 [55]). Some of these changes may potentially be related to changes in eddy transport statistics as hypothesized by Miller et al. (2005) [69] in a study of the Steller sea lions decline in the western GOA. Other important mechanisms for cross-shelf fluxes in the GOA include episodic upwelling, surface Ekman transport, upwelling seaward of a coastal wind jet and topographic steering (Stabeno et al., 2004 [92]).

This chapter is organized as follows. Section 3.2 compares the intrinsic (western basin) vs forced (eastern basin) interannual variability of the GOA mesoscale circulation. Section 3.3 discusses the interannual and decadal variations in cross-shelf flux in the eastern (Alaska Current region) and western (Alaskan Stream region) GOA basin. Each section will provide a summary and discussion of the results

3.2 Intrinsic and forced interannual variability of the GOA mesoscale circulation

In order to further clarify the mean, seasonal and interannual response of the GOA mesoscale circulation to atmospheric changes, we conduct numerical investigations with a high-resolution ocean model. Three ensembles, forced by the last 55 years of NCEP/NCAR wind stress reanalysis (Kalnay et al., 1996 [44]) and heat fluxes corrected using the NOAA extended SST (Smith and Reynolds, 2004 [88]), are used to separate the intrinsic and forced variability in the GOA. The primary goals of this section are to (1) understand how the surface circulation and eddy statistics are controlled by atmospheric forcing at the seasonal and interannual timescale, and (2) separate the intrinsic and forced variability in the GOA.

3.2.1 Experiments setup and domain

The Regional Ocean Modeling System, described in chapter 2, is used to investigate the forced and intrinsic variability of the Gulf of Alaska circulation.

The grid extends northward from 25^oN to 61^oN and westward from 111^oW to 179^oW. The average spatial resolution is between 19 km (South) to 13.4 km (North) with 30 vertical levels (with higher resolution at the upper ocean layer), that is to say a total number of 1,697,280 points (latitude x longitude x depth = 272 x 208 x 30). Although this resolution is of the same order of the Rossby deformation Radius, the model is eddy permitting and is able to capture qualitatively the large-scale Haida and Sitka eddies (diameters $\geq$ 200 km) along the eastern side of the GOA and the eddy centers along the Alaskan Stream. The domain of interest for this study includes all of the Gulf of Alaska from Washington State and presents open boundaries in the south and west. Along these open boundaries we use a modified radiation boundary condition (Marchesiello et al., 2001 [60]) together with nudging to observed monthly mean climatologies (Levitus et al., 1994 [54]). The nudging is stronger (timescale of 1 day) if the direction of the flow is inward and weaker (timescale of 1 year) for the outflow.

In order to avoid large pressure gradient errors (Mellor et al., 1994 [65]), the model bathymetry is obtained by a smooth interpolation from David T. Sandwell and Walter H. F. Smith bathymetry (Smith and Sandwell, 1994 [89]; Sandwell and Smith, 1997 [80]).

Experiment 1 (Table 3.1) consists of three ensembles, each forced by the last 55 years of NCEP/NCAR (National Center for Environmental Prediction/National Center for Atmospheric Research) wind stress reanalysis (Kalnay et al., 1996 [44]) and by heat fluxes corrected using the NOAA (National Oceanic & Atmospheric Administration) extended SST (Smith and Reynolds, 2004 [88]). The freshwater surface fluxes are set to a corrected monthly climatology derived during an 80 year

Table 3.1: Table of Experiments

	Run length	Initial conditions	Open boundaries	Surface forcing (monthly-means)
Experiment 1	163 years (53 + 55 + 55)	Levitus et al. (1994)	Temperature, salinity and geostrophic velocity derived from Levitus et al. (1994) + nudging	55 years wind stress of NCEP/NCAR heat fluxes corrected with NOAA extended SST fresh water fluxes from corrected climatology
Experiment 2				monthly climatological forcings derived from Experiment 1 forcing functions

long spinup run in which the surface salinity is nudged to the observed climatology
and the resulting flux correction is saved.

Experiment 2 differs from Experiment 1 in the surface forcing conditions, which
are prescribed to the monthly mean climatology. The initial and boundary conditions
remain unchanged. We refer to Experiment 2 as the "Unforced Run", in that there
is no forcing function with periodicity longer than the seasonal cycle. In contrast,
Experiment 1, which is forced by the time dependent NCEP winds and NOAA SST,
is referred to as the "Forced Run".

For the initial condition, zonal and meridional velocity, sea surface height, temper-
ature, and salinity are obtained from Levitus data (1994) [54]. The initial conditions
of the ensembles 2 and 3 use respectively the final states of ensemble 1 and ensemble
2. At the open boundaries all model integration use the modified radiation condition
(Marchesiello et al., 2001 [60]) and nudging to prescribed monthly climatologies for
temperature, salinity and geostrophic velocity derived from Levitus et al. (1994) [54].
The geostrophic velocity is computed using the bottom as the reference level of no
motion.

3.2.2 Mean and interannual circulation

The circulation in the GOA is mainly described by the subarctic gyre (Fig 3.1).
On the eastern boundary of the GOA basin, the North Pacific Drift diverges into
the southward California Current and the northward Alaska Current. The Alaska
Current is rich in meanders and eddies, such as Haida and Sitka along the eastern
boundary. As the Alaska Current flows along the Alaska Peninsula it becomes the
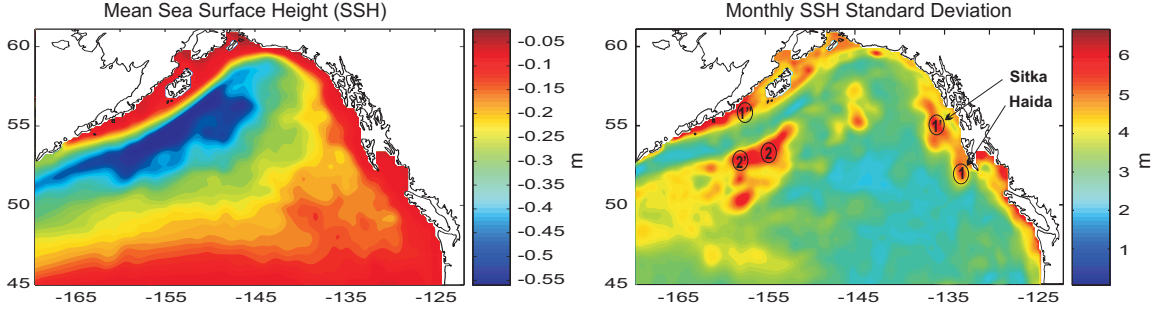
Figure 3.2: Mean and standard deviation of the sea surface height (SSH

Alaskan Stream, which has a more developed and richer eddy field associated with the strong instability of the mean currents (Melsom et al., 1999 [66]). Near the Kodiak Island, the Alaskan Stream is narrow (about 50 km) and strong (50 cm.s^{-1}) (Stabeno et al., 2004 [92]). The currents are principally in geostrophic balance and consequently follow lines of constant dynamic height with the largest values on the right. The model mean circulation, represented in Fig 3.2 by the sea surface height (SSH), is mostly consistent with this view described in the literature. In the eastern basin we find a broad northward current, corresponding to the Alaska Current, and an intensification of surface currents along the Aleutian Islands in the location of the Alaskan Stream. A map of the SSH standard deviation (Fig 3.2) shows high variance in regions of intense eddy variability along the southern edge of the Alaskan Stream, along the eastern basin, and in the coastal regions where the variability is directly forced by changes in the atmospheric winds (a discussion follows in Section 3.2.4). On the eastern boundary, maxima of standard deviation are found in the generation sites of the Haida and Sitka eddies. A corresponding region of high variance is not found at the location of the Yakutat eddy, which is not well represented in the model.

A closer inspection of the model mean momentum budget for the surface layer confirms (Fig 3.3a) that the dominant balance is geostrophic, with a stronger Alaskan stream (0.4 m.s^{-1}) following the topographic slope in the northwestern basin and a weak northward flow in the eastern basin. The model geostrophic flow along the

coast results from the ocean adjustment to the mean downwelling conditions in the eastern basin and upwelling along the topographic slope in the western basin. This is inferred from the model Ekman currents averaged over the surface layer (Fig 3.3b) and the corresponding vertical fluxes of temperature (Fig 3.3c), which show regions of surface divergence in the west and convergence in the east. A detailed analysis of the temperature budget shows that the dominant balance is between the vertical and the horizontal flux. The next largest term in the budget, although still small compared to the advection terms, is the surface heat flux (Fig 3.3d). On average the surface heat fluxes are warming the Gulf of Alaska except in regions of strong downwelling (see blue areas in Fig 3.3c and d) where the strong horizontal convergence of surface warmer water tends to heat the atmospheric marine boundary layer and cool the ocean surface.

To investigate the interannual modulation of the mean circulation we compute the first Empirical Orthogonal Function (EOF) of the model sea surface anomaly (SSHa), where the anomalies are defined by removing the seasonal cycle. The resulting EOF 1 (Fig 3.4a) explains 30 % of the total variance and has the same structure as the mean circulation. Therefore temporal modulations in the amplitude and sign of this pattern, which are inferred from the Principal Component 1 (PC 1; Fig 3.4e) of the three ensemble members, reflect interannual and decadal changes in the mean circulation. The spread of the PCs 1 of the ensemble members is very small suggesting that changes in the mean circulation are mainly forced. Indeed strong interannual modulations of the PCs 1 correspond to changes in the monthly PDO index (defined as the leading principal component of North Pacific monthly sea surface temperature variability) with a significant correlation of 0.64 (Fig 3.4f). Intensification of the gyre scale circulation is evident after the 1976-1977 climate shift, as well as during 1955-1960, 1965-1970 and more gradually during 1990-1998. Weakening of the circulations is evident during 1970-1975 and 1986-1991.
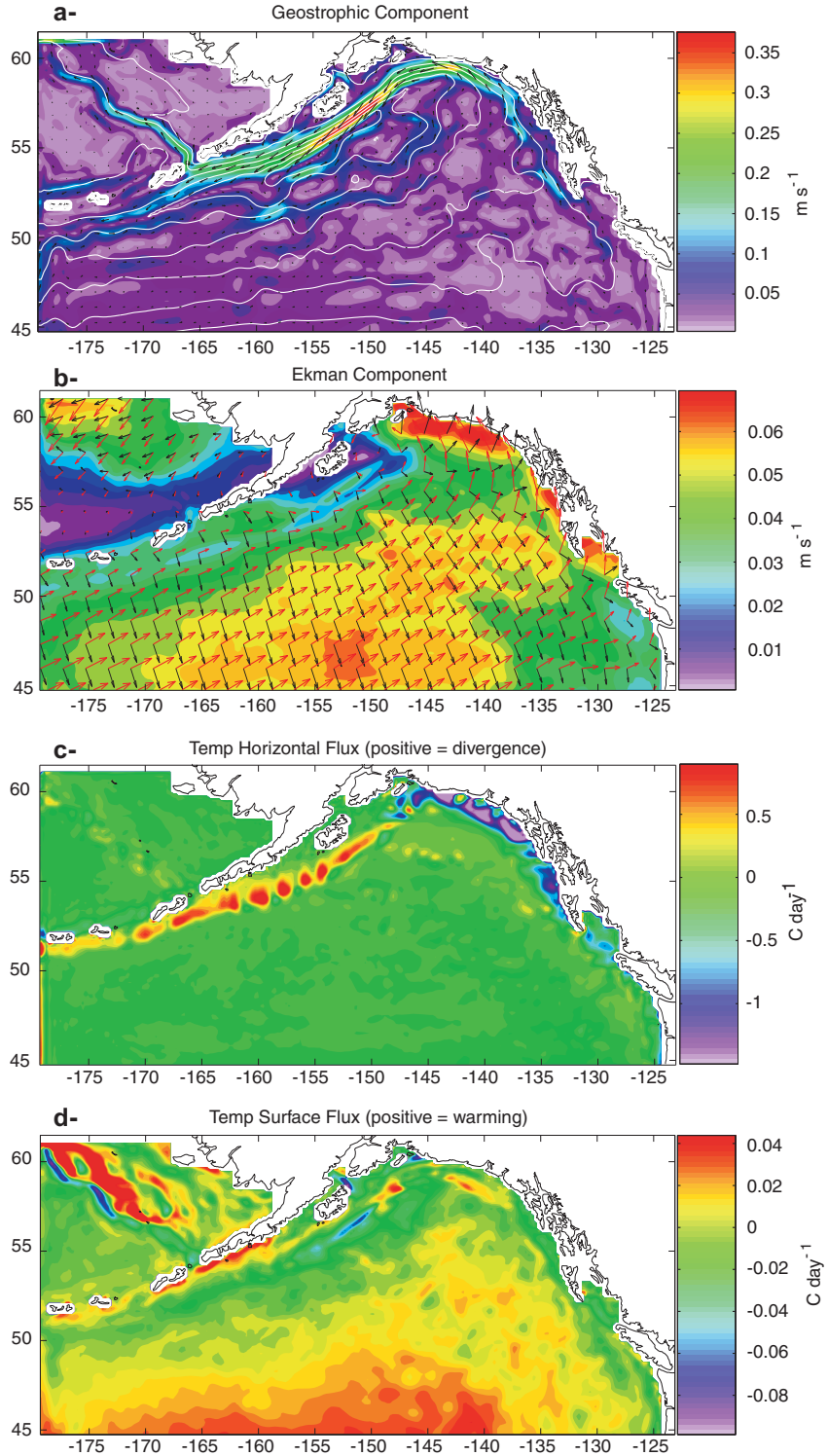
Figure 3.3: (a) Mean geostrophic surface currents, with mean SSH contours (white lines). (b) Mean Ekman transport in the model surface layer. The red arrows indicate the direction and intensity of mean surface wind stresses. (c) Temperature horizontal flux, positive regions indicate upwelling. (d) Temperature surface flux, positive indicates that the ocean is warming due to the atmospheric heat flux.

22
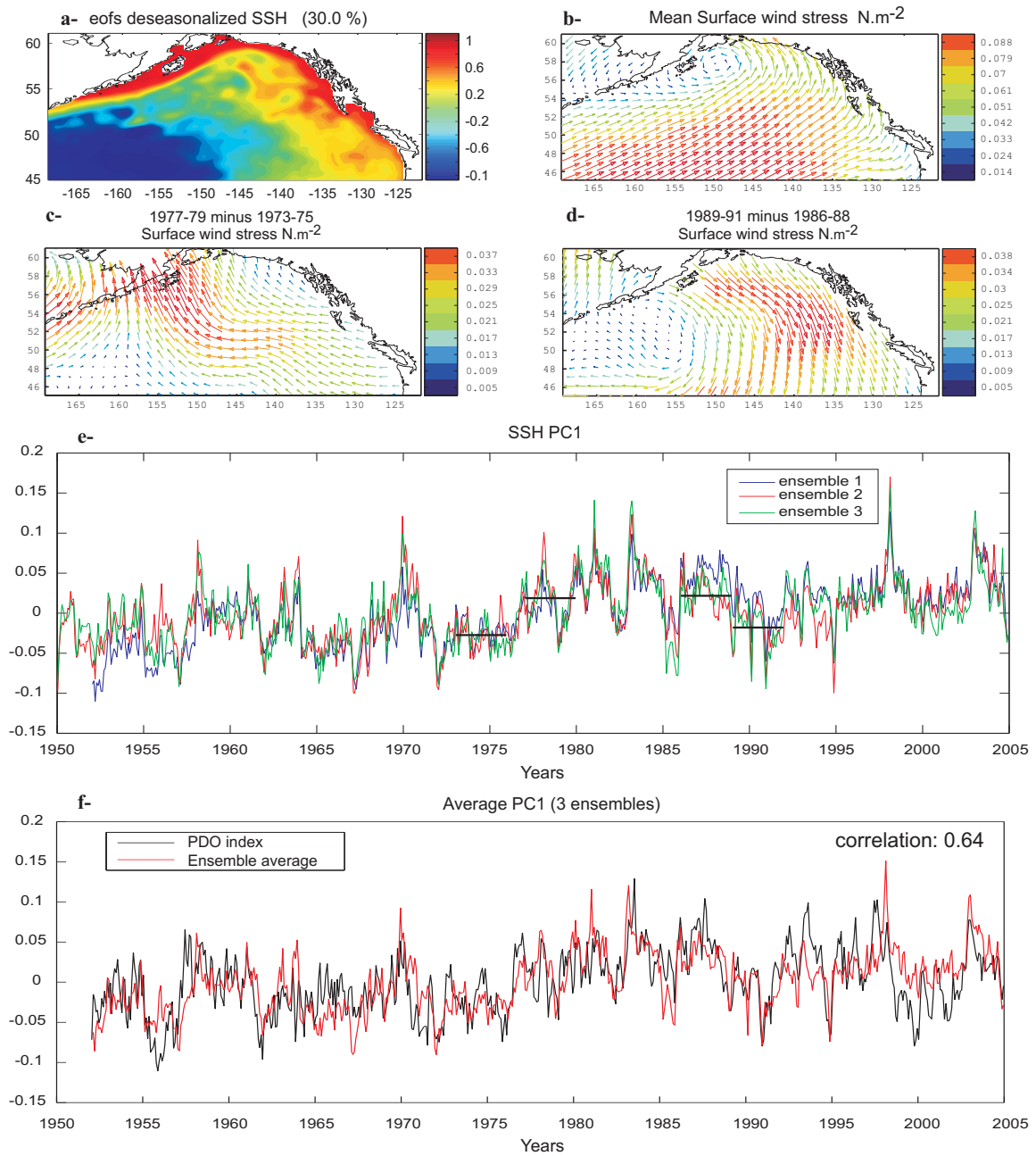
Figure 3.4: (a) First empirical orthogonal function (EOF 1) of the sea surface height after removing the seasonal cycle. EOF1 explains 30.0 % of the total variance. (b) Mean surface NCEP wind stress. (c) and (d) show the difference in surface wind stress for selected periods (black horizontal lines in (e)). (e) PC 1 for the three forced model ensembles. (f) Comparison between PDO index and PC1 ensemble average.

Composite maps of the difference in surface winds (Fig 3.4c and d) suggest that the gyre intensifies during anomalous southeasterly winds (stronger Aleutian low) and weakens when the winds are predominantly anomalous northwesterly. A detailed analysis of the model momentum and tracer budgets reveals that these extrema in the mean circulation are indeed forced by changes in the surface wind stresses (Fig 3.5 illustrates an example for the 1976 shift). In particular we find a strengthening of the gyre when the Ekman transport tends to converge mass towards the coastal boundary in the central Gulf of Alaska (Fig 3.5b). This condition is also associated with stronger than usual downwelling along the eastern boundary (Fig 3.5c) and upwelling along the Alaskan Stream. The contribution of surface heat fluxes is small compared to the mechanical forcing. The adjustment process of the gyre scale circulation in response to the interannual and decadal changes of the PDO and ENSO can be summarized as follows. When the GOA experiences stronger anomalous southeasterly winds (positive phase of the PDO as well as ENSO) there is net convergence of surface mass (downwelling conditions) in the central and eastern coastal boundary induced by Ekman transport (Fig 3.5b). This generates higher coastal SSH (Fig 3.5a) and lowers the coastal isopycnals. The resulting geostrophically adjusted currents (Fig 3.5a) intensify the gyre scale circulation. The opposite situation occurs during stronger anomalous northwesterly winds (negative phase of the PDO). In the next section we continue to explore the ocean adjustment process to changes in the forcing by investigating how the changes in the winds are reflected in the eddy scale circulation.

3.2.3   The seasonal and interannual eddy field

To gain confidence in the degree of realism of the model simulation, we compare the model seasonal SSH anomalies to the one derived from the AVISO satellite maps (Fig 3.6). These maps (http://www.jason.oceanobs.com) merge data from T/P or
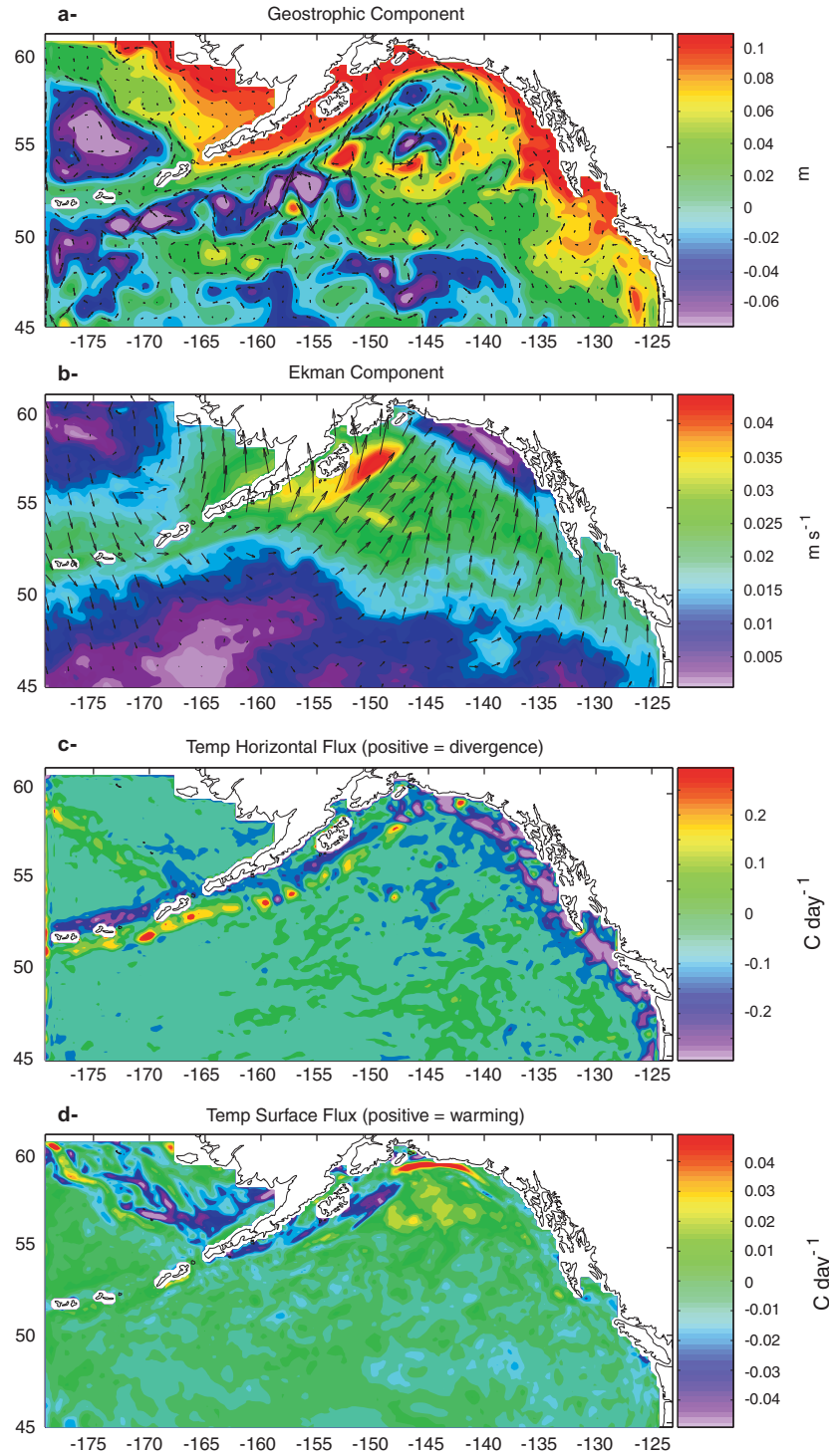
Figure 3.5: Difference maps for the periods (1977/80) minus (1970/75). (a) Difference in SSH and Geostrophic surface currents. (b) Difference in Ekman transport in the model surface layer. (c) Difference in temperature horizontal flux, negative regions indicate stronger downwelling conditions after 1976. (d) Difference in temperature surface flux, positive indicates that the ocean is warming due to the atmospheric heat flux.

JASON-1+ERS-1/2 and Envisat satellites to produce sea level anomalies at weekly resolution from October 1992 to January 2005 on a 1/3 x 1/3 Mercator grid. An annual oscillation of the SSHa along the coast is evident in both the model and satellite data. Consistent with Strub and James (2002) [94] observational results, the SSHa along the coast is positive during the winter months and negative in summer, leading to a strong SSH gradient (stronger downwelling current) in winter and weak SSH gradient (weak current) in summer. From the analysis of the model budget terms, we find that this oscillation is driven from the seasonality in the wind stress and consequent Ekman currents. Following the winter downwelling conditions along the coast in the eastern basin, a clear westward propagation of the SSHa is evident in both model and satellite during March through July. As the positive SSHa detaches from the coast a rich eddy field develops off the shelf. Anticyclonic eddies become a prominent feature, particularly in the model where the signature of the seasonal development of the Haida and Sitka eddies is stronger when compared to satellite observations. In the western basin we also find a stronger mesoscale signature in July and August. Although both model and AVISO seasonal SSHa maps use the same time range, from January 1993 to December 2004, the satellite maps reveal an overall higher SSH anomalies in the gyre interior between August and October and lower between January and May.

The seasonal propagation of eastern eddy field is also reflected in the eddy kinetic energy (EKE) phase map (Fig 3.7b). Along the coast the seasonal maxima is reached in January when the stronger current develop on the shelf in response to the stronger downwelling conditions. During late spring/summer the EKE peak is found further away from the coast in the eastern basin and reflects the seasonal development of the eddy field. During the fall the seasonal peak moves further offshore in the gyre interior. The amplitude of the seasonal EKE is strongest on the shelf where the currents are directly forced by the winds (Fig 3.7a).
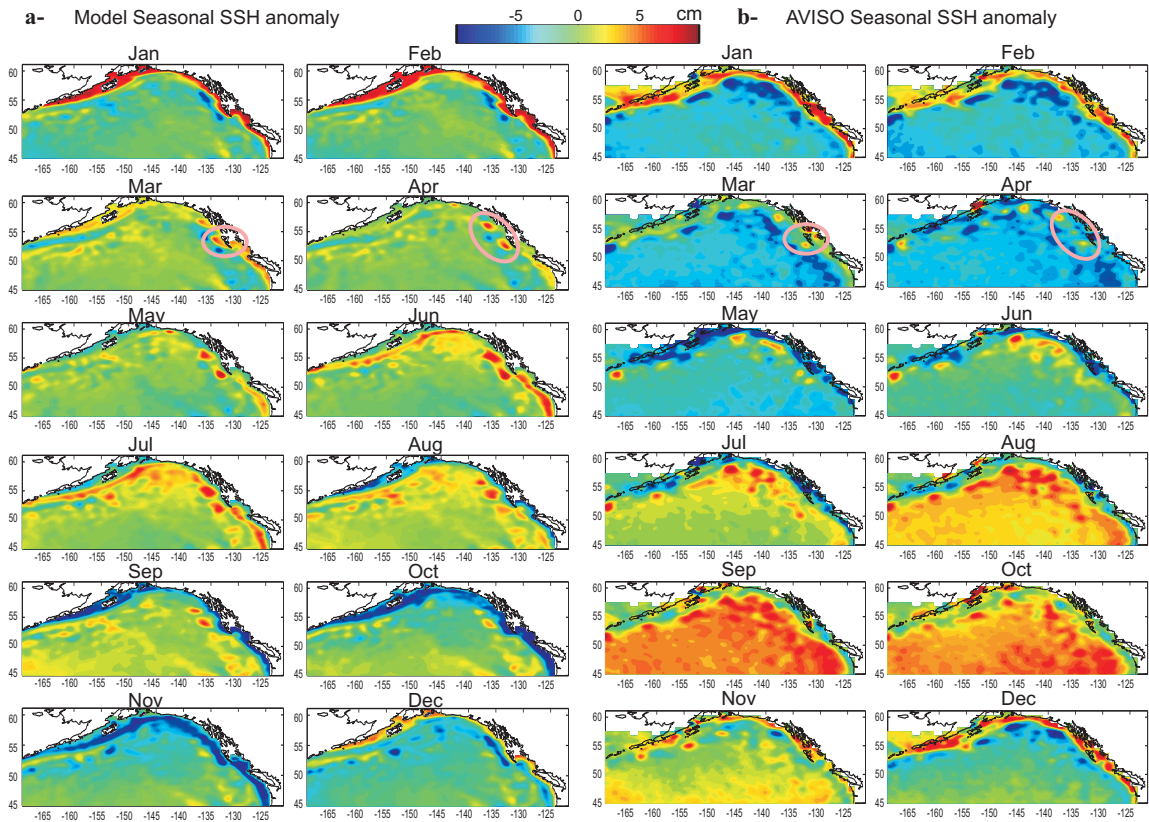
Figure 3.6: Model (a) and AVISO (b) SSH seasonal anomalies derived from 1993 to 2004.
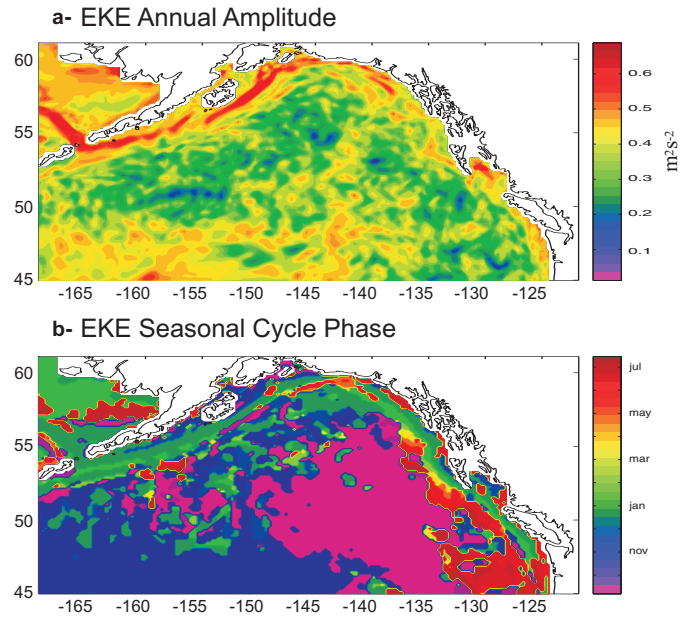
Figure 3.7: (a) Annual amplitude of the eddy kinetic energy (EKE) and (b) EKE seasonal cycle phase.

To better isolate the development of the large anticyclone along the eastern boundary we perform an analysis of the model SSHa EOFs 1 and 2 along the east coast (Fig 3.8). Consistent with the seasonal maps, the EOFs shows a spatially coherent excitation of SSHa along the coast (EOF 1) followed by offshore propagation (EOF2). The major anticyclonic eddies in EOF 2, Haida and Sitka, are captured by the model and exhibit substantial interannual variability as evident by the corresponding PCs (Fig 3.8c). Though the two EOFs are uncorrelated, a 1 year low pass filter of PC1 and PC2 (Fig 3.8c) shows a 200 days lag average, which confirms that the development of the two anticyclonic cores in EOF 2 (corresponding to Sitka and Haida eddies) follow the SSHa of EOF 1. The two EOFs explain more than 54 % of the variance. The same EOF analysis is performed for the specific region around the Queen Charlotte Islands, where Haida eddies are generated (figures not shown here). From this analysis we infer the speed of eddy propagation of 1.3 km day 1, which is consistent with previous estimates of 1.12 0.35 km day^{-1} by Gower and Tabata (1993) [34]. The PCs show that some of the largest events over the entire record correspond to strong El *Niño* years, 1982-1983 and 1997-1998. A table showing the year and month when large eddy events are found (Fig 3.8d) reveals that large Haida and Sitka eddies are mainly generated during winter months (December, January, February, March) and are phase locked with the seasonal cycle. Therefore, interannual changes in the amplitude of the generated eddy are reflected in interannual modulation of the seasonal cycle.

To further clarify the relationship between the modeled eddies and El *Niño* years, we perform the same EOF analysis for the three model ensembles and isolate the forcing patterns corresponding to large eddy events (Fig 3.9). We find that PCs 1 of all ensembles are correlated above 0.9 (Fig 3.9b and h) corroborating the hypothesis of a strongly forced regime. For the Haida region, a composite analysis of the winter wind patterns during times when PC1 is greater than 1 and less than 1, shows that
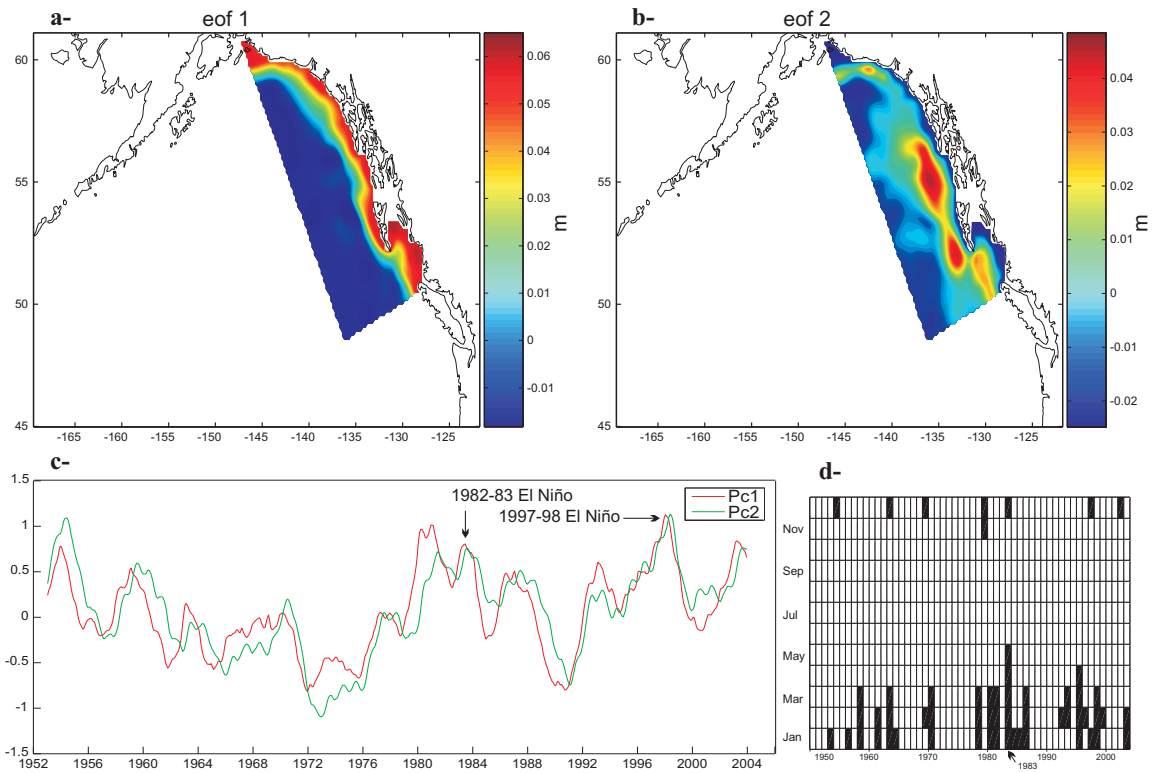
Figure 3.8: (a) EOF 1 and (b) EOF 2 of SSHa. (c) The red curve (green curve) is the principal component associated to EOF1 (EOF2), using a 1 yr lowpass filter. (d) Matrix showing the times when large Haida and Sitka eddies (EOF2) are formed in the model simulation.

29

the winds are predominantly southwesterly (Fig 3.9c and d). However if we take the differences between the composites and the mean winds we find that during times of higher amplitude eddies (PC 1 $\geq$ 1) the winds are strongly downwelling (Fig 3.9e) and therefore capable of exciting stronger SSHa. In contrast during times of weaker amplitude eddies the winds have upwelling favorable anomalies (Fig 3.9f). The same analysis performed for the Sitka region leads to the same results (Fig 3.9g-l), mainly that stronger eddies are excited by stronger winter downwelling winds. An inspection of the composite map of the winter wind stress anomalies during the 1982 and 1997 El *Niños* (Fig 3.10) confirm the existence of stronger downwelling winds, therefore explaining the observed correlation between El *Niño* and large eddy events. In contrast the La-Nina events of 1970 and 1988 show upwelling favorable winds and reduced eddy amplitude.

Excitation of positive SSHa along the coastal boundary can also be attributed to coastally trapped Kelvin waves of equatorial origin. Indeed Meyers and Basu (1999) [67] indicate that Kelvin waves are a source of interannual variability in the coastal current along western North America. However, in this study we used a monthly mean climatology southern open boundary condition from Levitus et al. (1994) [54], which does not include these tropically generated Kelvin-like waves. Nevertheless a comparison of the model coastal sea level with in situ records and satellite data in various coastal locations (Sitka, Neah Bay, Seward, Yakutat, Kodiak and Sand Point; Fig 3.11) indicate that the model hindcast is able to explain a very large fraction of the in situ sea level variance. For example at Sitka the model explains 41 % of the in situ observations variance, which is more than the satellite (21 %). At other locations, except Yakutat, the model generally compares more favorably than the satellite with in situ data explaining between 40 % and 70 % of the tidal gauges variance. The poor performance of the satellite data in the nearshore region has been reported before by Strub and James (2002) [94] who performed analysis of coastal
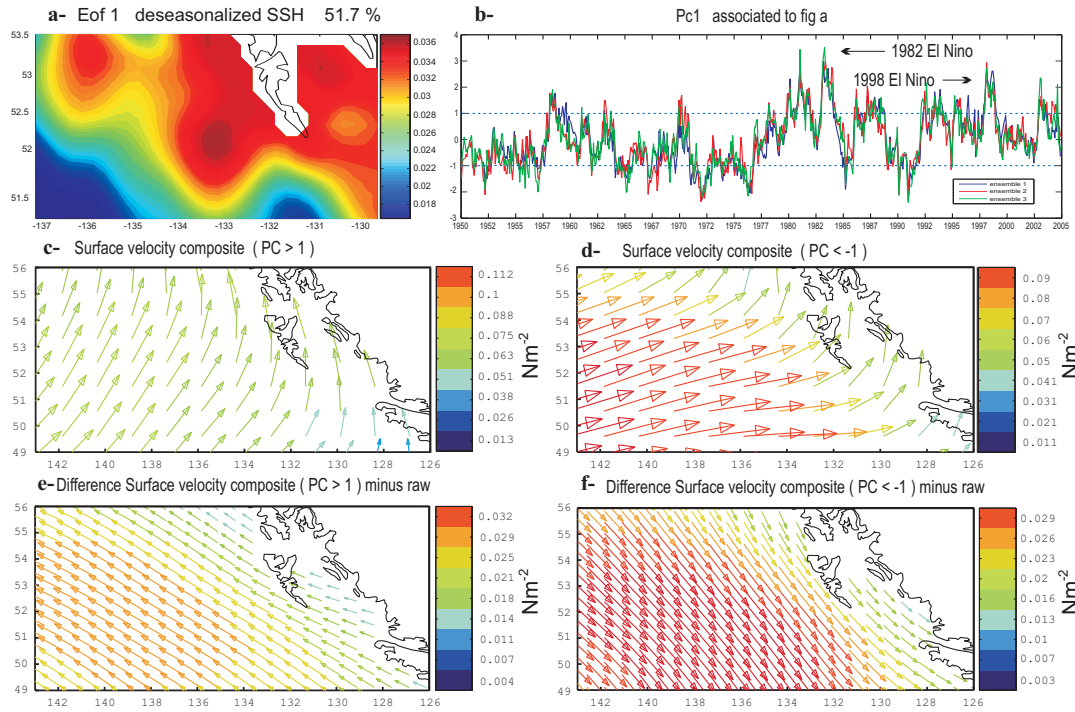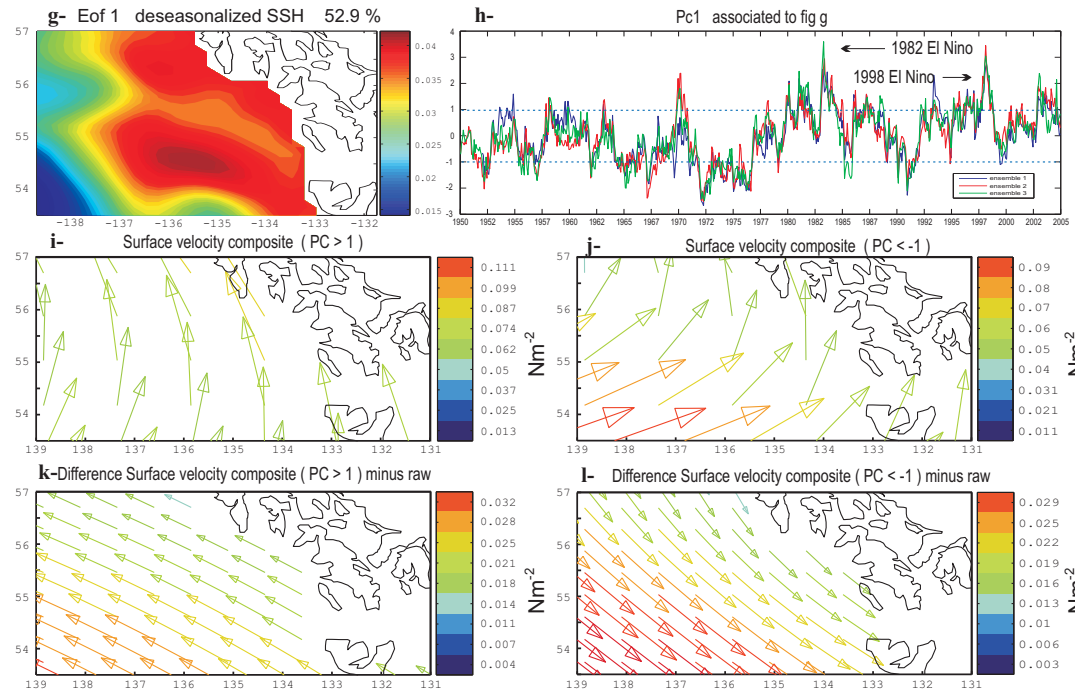
Figure 3.9: (a) EOF 1 and (b) PC 1 of SSHa in the region of formation of Haida eddies. (c) Wind stress composite maps for PC 1 ≥ 1, (d) for PC 1 ≤ -1. (e) Wind stress anomaly composite maps for PC 1 ≥ 1, (f) for PC 1 ≤ -1. (g-l) same as (a-f) but for Sitka region.
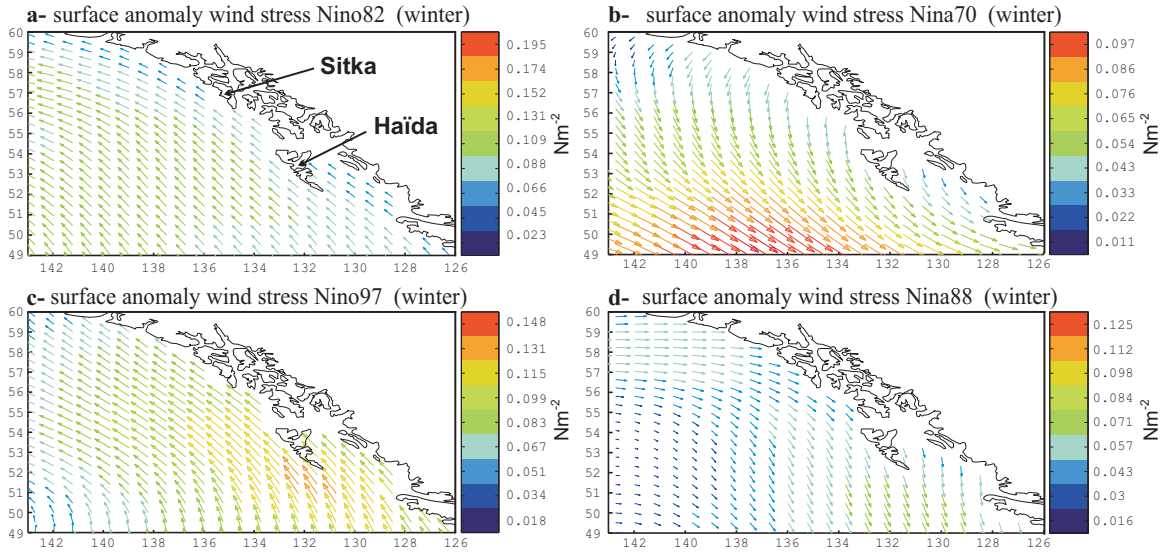
Figure 3.10: NCEP surface wind stress anomaly (with respect to the 1950 2004 period) for the El *Niño* winters (a) 1982 - 1983, (c) 1997 1998 and (b) La *Niña* winters 1970 1971, (d) 1988 1989.
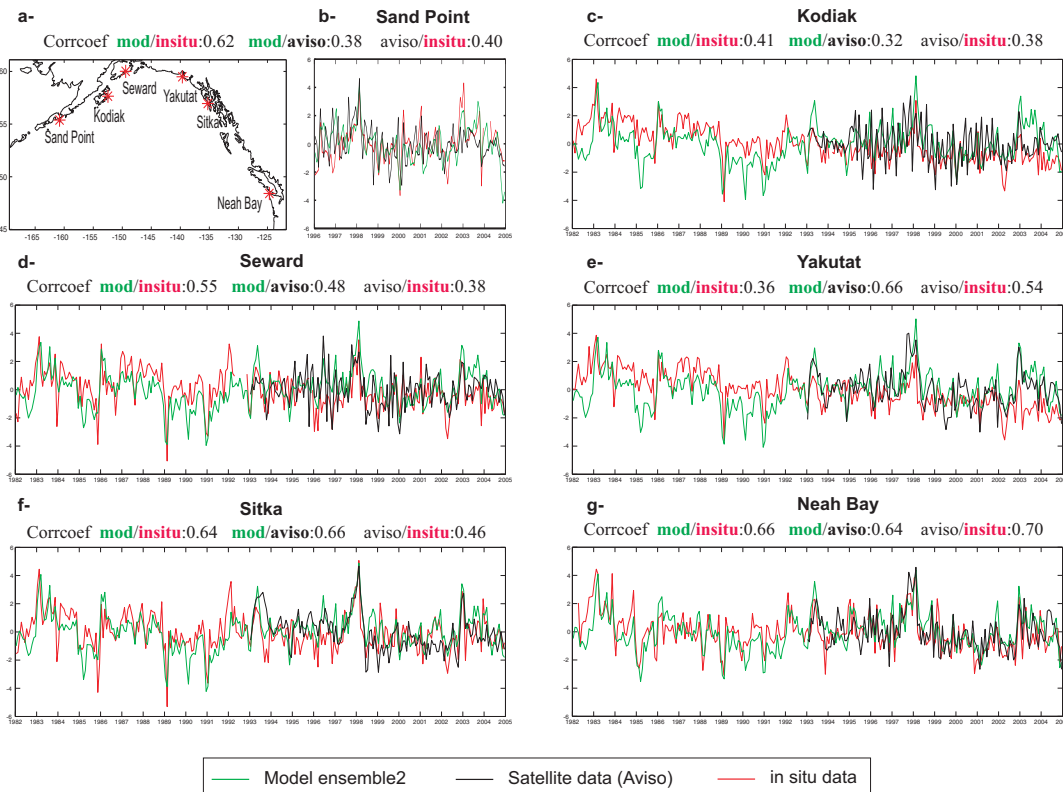
Figure 3.11: Comparison of the coastal deseasonalized SSH for Sand point, Kodiak, Seward, Yakutat, Sitka, and Neah Bay between the model output (green line), AVISO/TOPEX (black line) and GLOSS fast delivery data (red).

32

tide gauge and altimeter data to generate a merged sea level anomaly product for the Northeast Pacific. At Yakutat the correlation is not very high as the model does not reproduce Yakutat eddies very well. High correlations with in situ data are also found at coastal locations along the Alaskan Stream. From these results, which are consistent with Strub and James (2002) [94] observational results, we conclude that most of the interannual variability in the eastern boundary eddies and over the shelf, is locally forced by the winds, although coastally trapped waves may still contribute to additional variance.

We now discuss a dynamical framework to understand the relationship between the forcing and the development of large scale eddies in the eastern boundary. Previous studies suggest that the seasonal and interannual development of the mesoscale eddy field results from instability associated with the seasonal mean coastal currents and buoyancy gradients (Thomson and Gower, 1998 [99]; Melsom et al., 1999 [66]; Okkonen et al., 2001 [72]; Murray et al., 2001 [70]). However other studies suggest alternative generating mechanisms that rely on linear dynamics (Di Lorenzo et al., 2005a [28]). For this reason we attempt to reframe the current and previous findings in the context of instability of linear Rossby waves. This follows from the observation that EOF 1 and EOF 2 (Fig 3.8) are consistent with a linear excitation and propagation of a Rossby wave. LaCasce and Pedlosky (2004) [45] show using an idealized setup, that Rossby waves excited at the eastern coastal boundary are subject to baroclinic instability, in particular when the growth rate of the instability is fast compared to the time it takes for the wave to cross the ocean basin. Because the phase speed of Rossby waves decreases with increasing latitude, first mode baroclinic Rossby wave phase speeds are extremely slow in the Gulf of Alaska (about 1-2 km/day from Chelton and Schlax (1996) [18]). Indeed during winter, following the strong downwelling condition, the linear adjustment process to the positive sea level perturbations (seasonal in Fig 3.6a, interannual in Fig 3.8) leads to radiation of Rossby waves that

would take about 6 months to propagate away from the coastal boundary where they are excited. This timescale agrees with the observed and modeled SSHa propagation away from the east coast during winter and spring (Fig 3.8). However, LaCasce and Pedlosky (2004) [45] theory predicts that the excited Rossby waves become unstable at higher latitudes and will not have time to coherently propagate in the gyre interior. Both model and observations (Chelton and Schlax, 1996 [18]) support this view and do not show a meridionally coherent westward phase propagation.

To verify if the LaCasce and Pedlosky (2004) theory is applicable for the Gulf of Alaska, we compare the propagation timescale of the waves with the typical growth rate of baroclinic instability in the Gulf as inferred by the Eady index (Lindzen and Farrell, 1980) defined:

$$\sigma_E = 0.31 \frac{f}{N} \frac{du}{dz}$$

where f is the Coriolis parameter (s^{-1}), $N^2 = -\frac{g}{\rho_0} \frac{d\rho}{dz}$ represents the static stability (s^{-2}) and ρ the density of water (kg.m^{-3}). In the computation, we consider u as the current speed. The Eady index, σ_E, is then integrated between the surface and 100 m meters depth. Although σ_E describes the baroclinic instability of a zonal basic-state flow (Hoskins and Valdes, 1990) it still provides a rough estimate of the typical growth rate of the instabilities and is similar to the criteria used by LaCasce and Pedlosky (2004) which use the ratio between vertical shear and Rossby deformation radius. Fig 3.12 shows the model monthly mean maps of the Eady index, which exhibit a clear seasonal cycle with higher baroclinicity during winter. Between October and April along the coast where the SSHa is perturbed by the seasonal peak of downwelling winds, the Eady index has values between 4 and 7·10^{-6}s^{-1}. The corresponding timescale for the growth rate of the instability is 2-6 days, which is much too fast for the coastal disturbances to radiate away as Rossby waves.

The reoccurrence of large anticyclones at the same regional locations (e.g. Haida, Sitka and Yakutat) is not explicitly accounted for by the LaCasce and Pedlosky (2004)
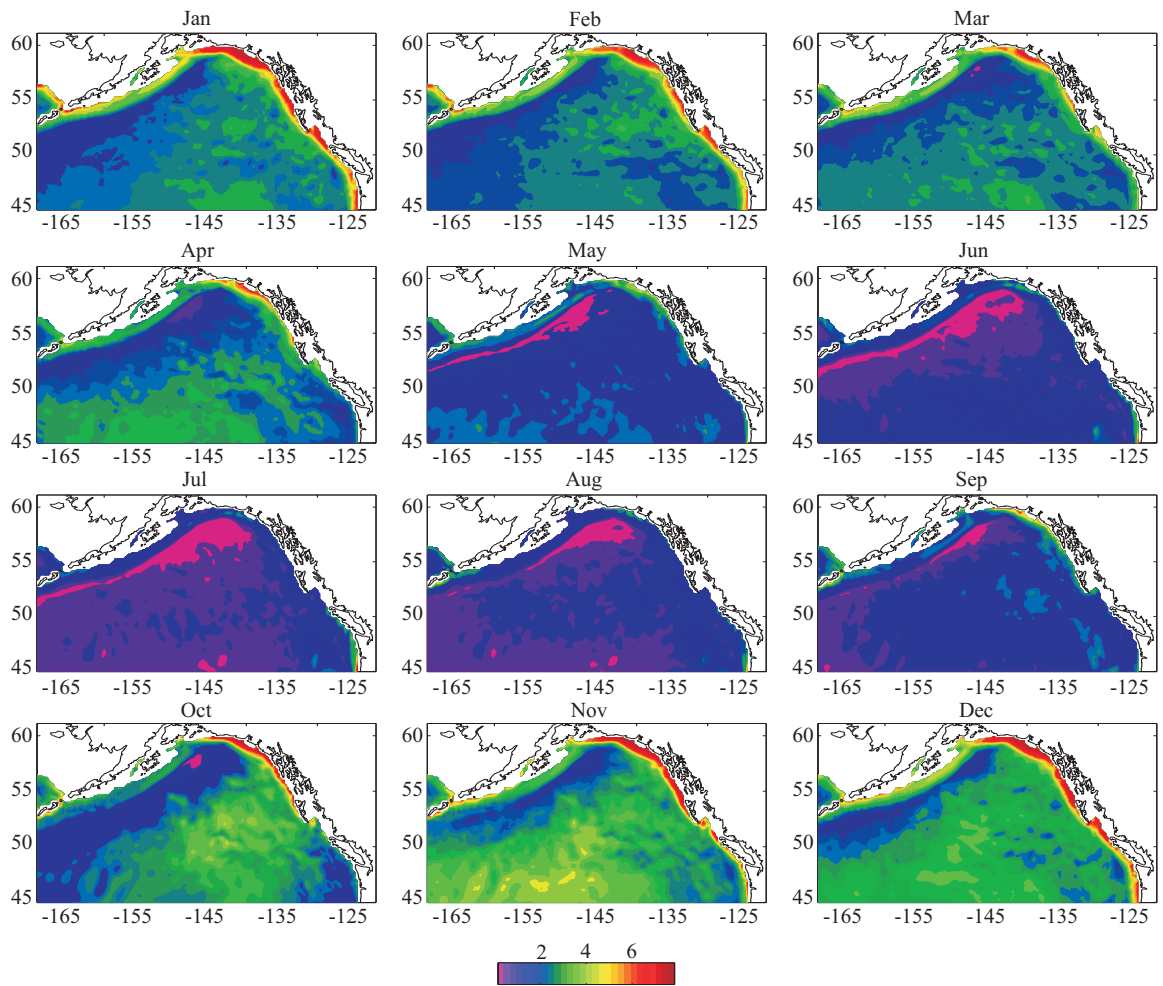
Figure 3.12: Seasonal variability of the Eady index, units in 10^{-6} s^{-1}.

theory. Nevertheless it is likely that during the linear phase of the ocean adjustment process to the wind induced isopycnal perturbations (EOF 1 and 2 Fig 3.8), the positive SSHa pattern is strongly influenced by the coastal and topographic geometry. This geographical focusing combined with the LaCasce and Pedlosky (2004) theory could explain why the amplitude of the eastern basin eddy field is proportional to the perturbation energy of the downwelling winds. Specifically during downwelling conditions in winter, the early response of the coastal ocean is linear with the onset of stronger poleward currents associated with the high coastal SSHa, and with the initial radiation of Rossby and topographically trapped waves. However because of the fast growth rate of the instability and the geographical focusing, most of the perturbation energy is locally trapped until converted into the eddy field. Although more detailed studies are needed, this energy trapping mechanism would explain the strong relationship between the perturbation amplitude of the winds and eddies.

3.2.3.2   Intrinsic regime in the Alaskan stream region

While the development of mesoscale eddies on the eastern GOA basin is modulated by changes in the wind stress, eddies along the Alaskan Stream (western basin) do not correlate with atmospheric forcing and their variability may be intrinsic (Okkonen et al., 2001 [72]). To separate the intrinsic and forced variability in the GOA we conduct an additional long-term (300 years) model run forced by climatological monthly mean surface fluxes (momentum, heat and freshwater; Experiment 2; Table 1; "Unforced run"). We then separate the SSH variance of the "Forced Run" and "Unforced Run" into seasonal (defined as all frequencies ≥ seasonal) and interannual (all frequencies lower than seasonal) (Fig 3.13a, b, d and e). First inspection of Fig 3.13a-c shows that both runs exhibit similar seasonal variances with higher values along the coast where the seasonal winds drive the coastal current. A map of the difference in seasonal variances (Fig 3.13c) shows that the "Unforced Run" has higher

variance at the generation sites of Haida and Sitka eddies. This is expected because the large interannual eddy events in these regions are phase locked with the seasonal cycle (see previous discussion of Fig 3.8), therefore some of the seasonal variance is shifted to the lower frequencies in the "Forced Run". If we now compare the maps for the interannual variance we find that the "Unforced Run" (Fig 3.13e) has strong variance in regions of high eddy activity in both the western and eastern basin. Since this model run has no forcing on periodicities higher than seasonal, regions of high variance must be associated with internal ocean (intrinsic) variability. To assess the degree of intrinsic variance we take the difference in variance between the Forced and Unforced (Fig 3.13f). Three important features can be isolated. First we observe that in the western basin (Fig 3.13f) there is no significant difference in interannual variance between the Forced and Unforced run. This confirms that most of the variance in the region of high eddy activity along the Alaskan Stream is intrinsic in nature. A second important feature in the difference map is in the shelf region along the western basin coastline. Here the "Unforced Run" has much less variance than the "Forced Run". This confirms that interannual changes in shelf circulation are mostly forced by the winds and it explains why the model "Forced Run" ensembles are so favorably correlated with in situ tide gauges (as shown before in the discussion of Fig 3.11). The third feature is in the eastern basin, where the "Forced Run" has higher variance along the eastern boundary. This result agrees with the findings of the previous section showing that interannual changes in the winds force large anticyclones eddy such as Haida and Sitka.

To further isolate the intrinsic and forced variability we compare timeseries from all Forced model ensembles in four selected regions of eddy activity, two in the western basin and two in the eastern basin (Fig 3.14a, c, e and g). These timeseries show that in the eastern basin (Fig 3.14a and c) the spread of the ensemble members is very low with shared variance above 42%. This confirms again the existence of a forced
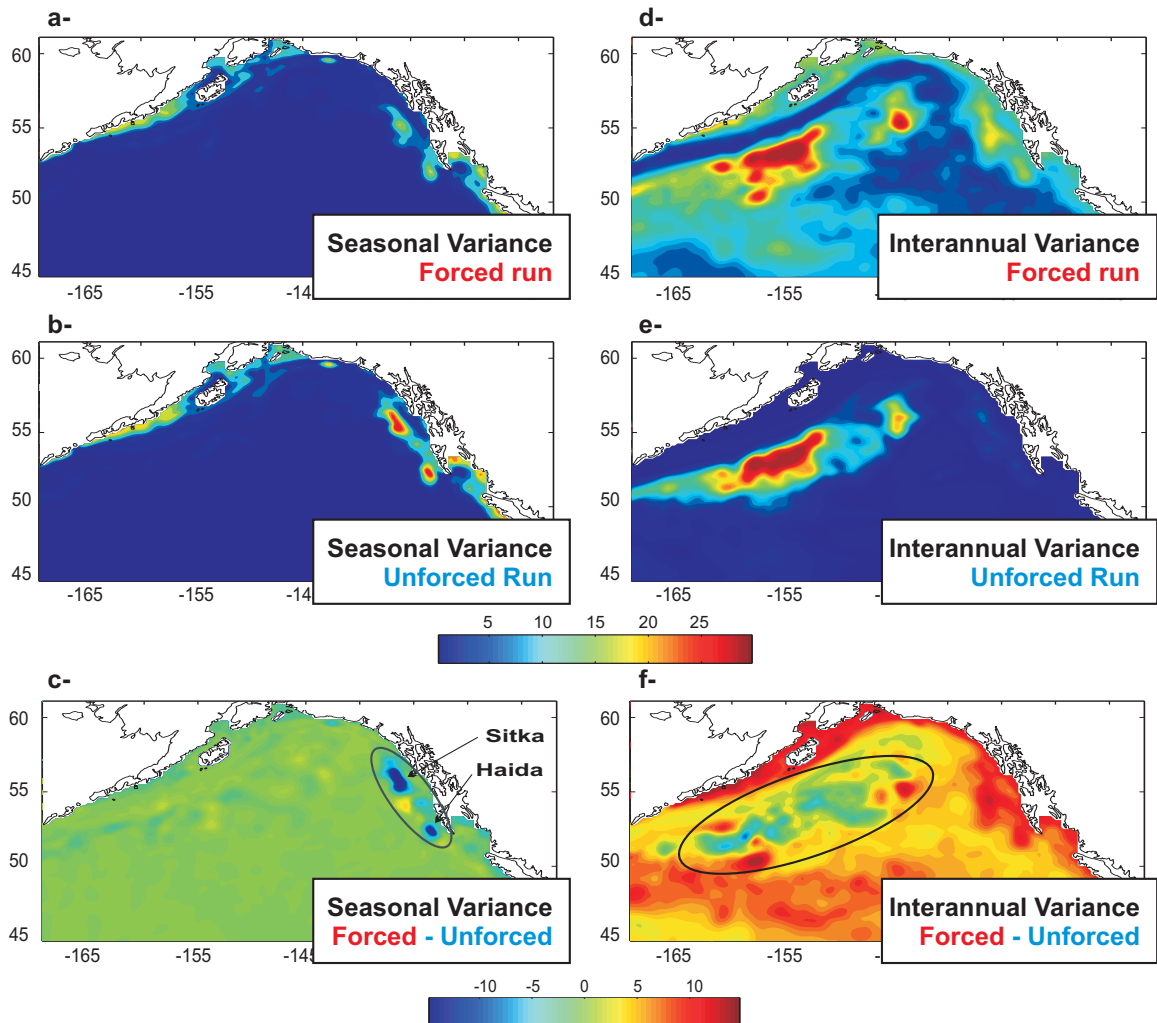
Figure 3.13: Model SSH variances (m^2) for the run forced by monthly NCEP wind stress (first row) and for the run forced by climatology monthly wind stress (second row). The difference between the two runs is shown in the 3rd row. The first (second) column shows the seasonal (interannual) variance.

regime. In contrast in the western basin the ensembles members share little variance (Fig 3.14e and g) and are mostly uncorrelated with each other. Some low frequency variability after 1990 is shared by all the ensemble members in the western basin, with an indication of a negative trend, however the amount of explained variance by this component is small. Interestingly a comparison with satellite data (not shown) reveals a similar negative trend over the last 10 years, however we did not pursue this aspect further as the temporal data coverage is short.

Although eddy variability in the western basin is intrinsic, one may expect that changes in variance from year to year can be related to changes in the mean ocean conditions or forcing function. To explore this concept we compare the 4-year running standard deviation for all ensembles (Fig 3.14, right column). On the eastern boundary inspection of the timeseries show a strong degree of correlation among all ensembles implying that interannual changes in eddy variance are also forced. In contrast in the western basin the spread among the ensemble members is high, although there are periods in the record when the ensembles are closer to each other. This reinforces the idea that changes in the forcing have a weak impact in modulating the eddy variance, along the Alaskan Stream, on interannual timescales.

We also investigate if ENSO teleconnected atmospheric forcing may play any role in changing the conditions for baroclinic instabilities. We quantify the ENSO effect by correlating the instability growth rate (the Eady Index) with the $Niño34$ index (Fig 3.15). The spatial pattern of the correlation shows that along the eastern boundary and northern Gulf of Alaska, an increase in the instability growth rate is positively correlated with positive ENSO phases. In contrast along the Alaskan stream in the region of high SSHa eddy variance, and in the gyre interior, we find a negative correlation indicating that during El $Niño$ the growth rate is reduced. However the amount of negative correlation is insignificant, which agrees with the hypothesis of the intrinsic nature of eddy variability in the western basin.
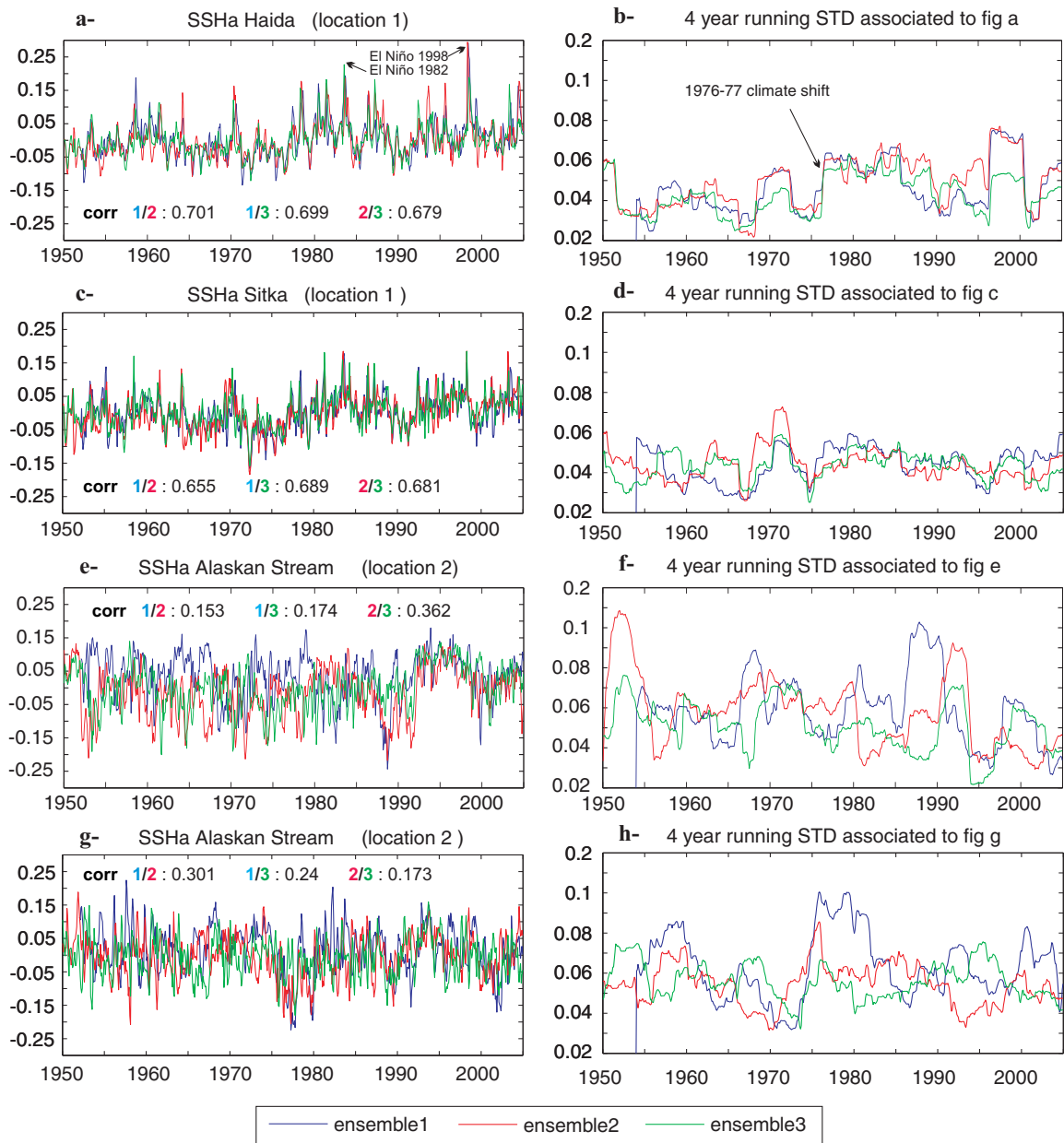
Figure 3.14: For the three ensembles (1, 2, 3), (a), (c), (e) and (g) show the SSHa respectively in the location 1, 1', 2 and 2' represented on Fig 3.2c. (b), (d), (f) and (h) show the 4 year running standard deviation associated to (a), (c), (e) and (g). (corr = correlation coefficient).
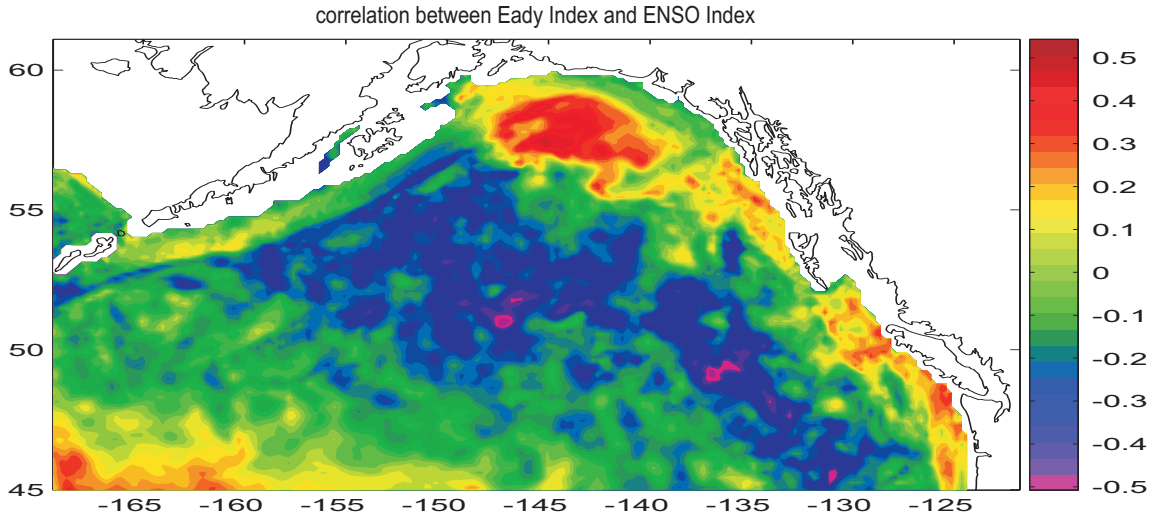
Figure 3.15: Map of the correlation between Eady index and ENSO index

3.2.4   Summary and conclusions

The adjustments of the Gulf of Alaska circulation to changes in large scale climate forcing has been investigated using three high resolution ensembles of a regional ocean model forced with the 1950–2004 NCEP/NCAR winds and NOAA SST corrected heat fluxes. Consistent with previous descriptions of the circulation we find that the mean currents are mainly geostrophic (Fig 3.3a) and maintained by Ekman downwelling conditions in the eastern basin and upwelling along the Alaskan Stream (Fig 3.3b and c). On interannual and decadal timescale the mean circulation is strongly modulated by changes in the large scale climate forcing associated with PDO and ENSO variability (Fig 3.4). The leading mode of spatial and temporal variability of the mean currents in the three model ensembles is significantly correlated with the PDO (0.64) and shows strong peaks during El *Niño* (e.g. 1997-1998). Intensification of the gyre scale circulation is found after the 1976-1977 climate shift, as well as during 1955-1960, 1965-1970 and more gradually during 1993-1995. A detailed analysis of the model momentum and tracer budget reveals that when the GOA experiences strong anomalous southeasterly winds (positive phase of the PDO after the 1976 shift and the 1997 ENSO) there is net Ekman convergence of surface mass (downwelling

41

conditions) in the central and eastern coastal boundary (Fig 3.5b). This generates higher SSHa (Fig 3.5a) and lower isopycnals along the coast. The resulting geostrophically adjusted currents (Fig 3.5a) intensify the gyre scale circulation. The opposite situation occurs during strong anomalous northwesterly winds (negative phase of the PDO).

Interannual changes in the surface winds are also reflected in modulations of the seasonal development of high amplitude anticyclonic eddies along the eastern basin, in particular at the location of the Haida and Sitka eddies. The generation of the large interannual eddy events during winter-spring, is phase-locked with the seasonal cycle and is consistent with a quasi-linear Rossby wave response to stronger winter southwesterly winds typical of El *Niño* (Fig 3.8 and 3.9). The high correlation between the amplitude of the eastern basin eddy and the perturbation energy of the downwelling winds is explained by the combined effect of geographical focusing and instability of Rossby waves at higher latitudes (LaCasce and Pedlosky, 2004 [45]). Specifically during downwelling anomaly conditions, the early response of the coastal ocean is linear with the onset of stronger poleward currents associated with the high coastal SSHa, and with the initial radiation of Rossby and topographically trapped waves (Fig 3.8). However because of the fast growth rate of the instability (Eady index maps Fig 3.12) and the geographical focusing associated with the coastal geometry, most of the perturbation energy in the Rossby wave response is locally trapped until converted into the eddy field.

In the western basin, the high core of interannual eddy variability south of the Alaskan Stream (Fig 3.13d) is not correlated with large scale forcing and appears to be intrinsic. Indeed a comparison of the forced and internal interannual variability from the three forced ensembles and a multi-century-long integration forced only with the seasonal cycle of winds, heat and freshwater, shows that the intrinsic variance alone explains most of the eddy variability (Fig 3.13f). The asymmetry between the

eddy forced regime in the eastern basin and the intrinsic regime in the western basin is also confirmed by timeseries of the ensemble members SSHa. These show that along the eastern boundary the spread is very low with shared variance above 42 % (forced regime). In contrast in the west, the ensembles members share little variance (Fig 3.14e and g) and are mostly uncorrelated (intrinsic regime), although some low frequency co-variability is evident after 1990.

We also explored the possibility that ENSO atmospheric teleconnections may impact the degree of baroclinicity in the western basin. However a spatial correlation analysis between the Eady index, which is a measure of the instability growth rate, and $Ni\tilde{n}o34$ index shows high correlations only along the eastern boundary and northern Gulf of Alaska but not in the centers of high eddy activity in the western basin.

Although the eddy variability in the western basin is intrinsic, interannual changes in the shelf circulation are forced by the winds (Fig 3.13f). A comparison of SSHa between tidal gauges and the three model ensembles forced with the NCEP winds, reveals that the model is able to explain between 40 % and 70 % of tidal gauges variance. This finding suggests that most of the shelf variability on interannual scale does not strongly depend on equatorially trapped waves, but rather on downwelling (upwelling) conditions associated with the large scale wind stress patterns.

This study provides a dynamical framework to interpret and predict how the GOA circulation has and will respond to large scale climate forcing. The model analyses suggest that the adjustment to large scale climate forcing of the coastal and gyre-scale mean circulations is predictable. On decadal and interannual timescale the most important aspect of the forcing is the overall strength of downwelling conditions along the coast, although the role of freshwater forcing has not been fully investigated. River runoff along the GOA is known to contribute to the cross-shore buoyancy gradients, which in turn strengthen the shelf circulation. Therefore decadal variation in river runoff may also lead to additional variability in the currents and their stability

properties. This study also supports the idea of an east-west asymmetry in the response of the mesoscale eddy circulations. In particular eddy activity in the eastern basin is strongly correlated with changes in downwelling favorable winds, while in the western basin the variability is mainly intrinsic. The link between stronger eddy in the eastern basin and downwelling winds has important climate implications. It allows predicting changes in the cross-shore transport of important biogeochemical quantities such as iron, oxygen and chlorophyll-a, which in a global climate change scenario may contribute to feedbacks in the HNLC region of the GOA. Within the dynamical and modeling framework presented in this study, further analyses with higher resolution nested models will better resolve the mixing statistics associated with the eddy field in eastern and western basin. Model representations of the GOA circulation are in fact very sensitive to the coastal and topographic geometry. As such the model results presented so far should be interpreted more qualitatively rather than quantitatively.

3.3 Interannual and Decadal Variations in Cross-shelf Transport in the GOA

The waters of the GOA and the Bering Sea provide more than half of the total annual fish catch for the United States. The central Gulf of Alaska reveals a high-nutrient/low-chlorophyll (HNLC) region with iron limitation (Harrison et al, 1999 [38]; Boyd et al., 2004 [10]). There is evidence that eddies, generated at the coast, impact iron distribution and therefore play a role in maintaining high-chlorophyll concentration. The mesoscale eddies generated along the Alaska Current (eastern basin) transport nutrients (Whitney and Robert, 2002 [104]; Ladd et al., 2005 [48]) and iron (Johnson et al., 2005 [43]) to the interior. More specifically, Batten and Crawford (2005) [5] observe higher concentrations of coastal zooplankton within the core of the eddies, collected by a Continuous Plankton Recorder between 2000 and 2001. Even though the correlation between eddy variability and changes in ecosystem

has not yet been fully established, the ecosystems have been noticed to respond to large-scale atmospheric variability (Mantua et al., 1997 [58]; Litzow et al., 2006 [55]).

The region is extremely productive at all trophic levels despite observations showing downwelling conditions along the coast (Stabeno et al., 2004 [92]), with stronger downwelling condition during winter months. On decadal time scales, the Pacific Decadal Oscillation (PDO) is the leading mode of North Pacific variability. Changes in the PDO are driven by changes in the Aleutian Low pressure system (Fig 3.16a and 3.16b), which also modulate coastal downwelling conditions. Okkonen et al (2001) [72] and Combes and Di Lorenzo (2007) [20] (section 3.2) show stronger mesoscale eddy activity, during years in which wind forcing promotes strong downwelling. This suggests that interannual and decadal modulations of the GOA open ocean ecosystems may be explained by exploring the statistics of eddy induced cross-shelf transport.

This section focuses on the seasonal and interannual variations in cross-shelf transport in the GOA, by looking at the distribution and variability of a passive tracer injected at the coast (see section 2.5). The tracer allows us to track coastal water masses and can be used as a proxy for coastal quantities such as iron. The goal of this study is to characterize the statistics of transport of the passive tracer and to understand how changes in atmospheric winds modify the distribution and transport of coastal water masses.

3.3.1 Data: Model and observation

As in the previous section, the model experiment is performed using the Regional Ocean Modeling System (chapter 2).

For that experiment, the domain now covers the coast from the Vancouver Island to the Alaskan Peninsula (Fig 3.16c). The grid has an average spatial resolution of 11km and uses 42 levels in the vertical, with higher resolution at the upper ocean layer. This resolution is able to capture large eddies in the western and eastern side

of the basin, which have an average diameter from 150 to 200 km (western basin: Crawford et al., 2000 [26]; eastern basin: Crawford, 2002 [23]). The initial conditions and open boundaries are obtained from an outer experiment, which is conducted with the same grid resolution on a larger domain that covers the entire northeast Pacific coast. This outer grid uses boundary conditions from a hindcast simulation using the Community Climate System Model (CCSM; Collins et al, 2006 [19]) version of the Parallel Ocean Program (POP; Smith and Gent, 2002 [87]). The surface forcing functions for the outer experiment (6 hourly forcing at 2° x 2° resolution) is obtained from the Common Ocean-Ice Reference Experiments (CORE), developed by Large and Yeager (2004) [50] and the air sea fluxes are parameterized using bulk fluxes (Fairall et al., 2003 [33]). Our regional nested model uses prescribed surface fluxes obtained by taking the monthly average flux resulting from the outer grid integration. We use the KPP scheme for vertical mixing in the surface boundary (Large et al., 1994 [51]) and implicit horizontal mixing associated with the third order upstream bias scheme (Shchepetkin and McWilliams, 2005 [86]).

On average, the ocean circulation in the GOA is characterized by a large scale cyclonic Alaskan gyre, with the broad Alaska Current on the eastern basin and a stronger Alaskan Stream along the Aleutian Islands (section 3.2). The model mean circulation, illustrated in Fig 3.16c, is consistent with this view and shows a surface current velocity up to 0.4 ms^{-1} in the western basin associated with a strong cross-shelf SSH gradient south of the Alaskan Peninsula (white lines on Fig 3.16c). Finally, a map of the SSH standard deviation (Fig 3.16d) indicates high variability all along the coast, where intense eddy variability is observed (Entire Basin: Ladd, 2007 [46]; western basin: Crawford et al., 2000 [26]; eastern basin: Tabata, 1982 [97]; Di Lorenzo et al., 2005 [28]).

To add confidence in the degree of realism of the eddy variability in the model simulation, we compare the model Eddy Kinetic Energy (EKE) to the one derived
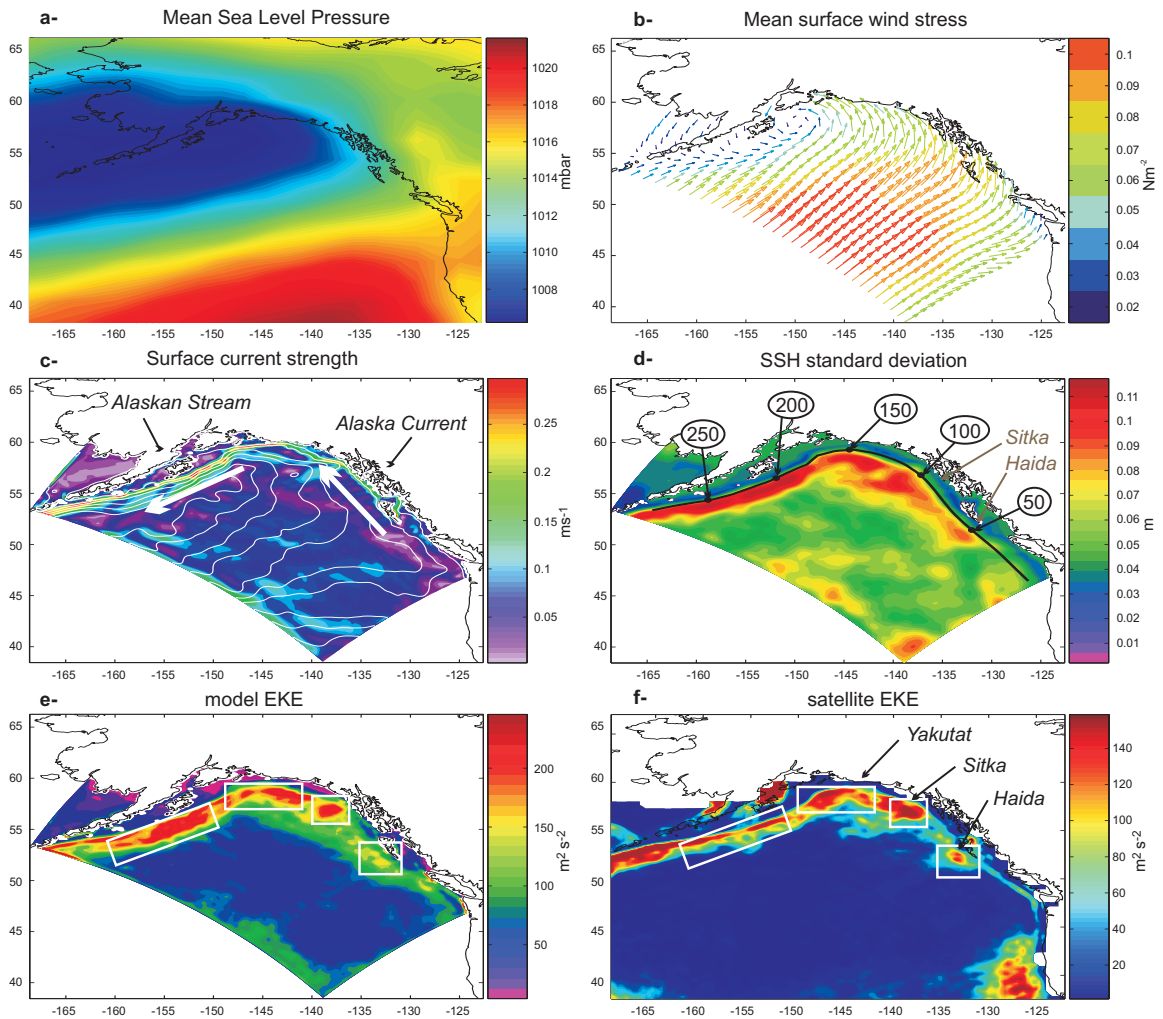
Figure 3.16: (a) Mean sea level pressure and (b) mean surface wind stress over the period 1965–2004. (c) Mean surface current strength (ms^{-1}), with mean SSH (white contours), and (d) SSH std dev. (e) Model EKE and (f) AVISO EKE

from the AVISO satellite maps (Fig 3.16e-f). The satellite EKE is calculated from the Sea Level Anomaly (merged data from T/P or JASON-1+ERS-1/2 and Envisat satellites available at http://www.jason.oceanobs.com), as defined by Ladd (2007) [46] by $EKE = \frac{1}{2}[\langle U_g'^2 \rangle + \langle V_g'^2 \rangle]$ where U_g' and V_g' are the geostrophic velocity anomalies. Consistent with Ladd (2007) [46], high values of EKE along the Alaska Current (eastern basin) and the Alaskan Stream (western basin) are evident both in the model and the satellite data. On the western GOA basin, eddy activity is constrained to the shelf break. On the eastern GOA basin, we notice the signature of three major eddy groups associated with a region of high EKE, usually named according to the location of their formation, Yakutat, Sitka and Haida (Tabata, 1982 [97]; Crawford, 2002 [23]). The eddies observed in the western and eastern basin show different dependencies with the atmospheric forcing reflecting different generation mechanisms. While eddies in the western basin are not directly affected by the atmospheric forcing, the development of mesoscale eddies on the eastern GOA basin is modulated by changes in wind-induced downwelling (Combes and Di Lorenzo, 2007 [20]; Henson and Thomas, 2008 [1]) and coastally trapped waves of tropical origin (Melsom et al, 1999 [66]). Eddies in the Alaskan Stream (western basin) are often a year or more old when they arrive in this stream, so their strength would also depend mainly on atmospheric conditions when and where they formed.

3.3.2 Results

The transport pathways and statistics associated with the mesoscale circulation in the model are characterized using a passive tracer advection/diffusion equation, detailed on chapter 2. For this experiment, the tracer is released continuously over a region from the coast to 50km offshore and from the surface to 50-m depth. The time scale τ is set to 4 years, which is the average time scale that eddies survive in the gyre after their generation at the coast (Crawford 2002 [23]). It also allows the modeled passive
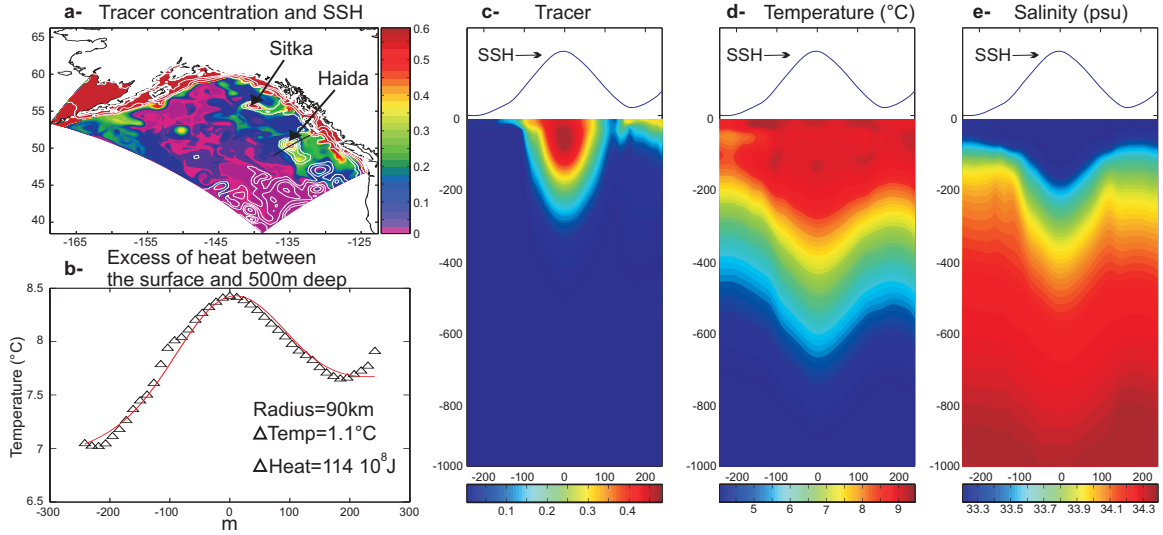
Figure 3.17: (a) Tracer concentration and SSH (white contours, contour interval is 5 cm from 0 to 20 cm) for August 1998. (b) The excess of heat across the eddy (the red curve is the fitted Gaussian of the model temperature). Vertical section of (c) tracer, (d) temperature, and (e) salinity.

tracer to live far longer than iron at the ocean surface. Iron seems mostly to be taken up by phytoplankton in the first spring of an eddy s life (Johnson et al. 2005 [43]).

We begin by testing if the passive tracer approach realistically tracks the transport of coastal waters associated with eddies generated at the coast. We focus on one model snapshot during August 1998 (Fig 3.17a). The eddy field in the eastern basin was dominated by eddies formed during the El *Niño* of the preceding winter (Melsom et al, 1999 [66]; Henson and Thomas, 2008 [1]), in particular the large anticyclonic Haida and Sitka eddies, which are well reproduced by the model hindcast (white lines on Fig 3.17a). The core of the Haida and Sitka eddies correspond to local maxima in passive tracer concentrations. This confirms that the model adequately reproduces the offshore transport of coastal water, here represented by the passive tracer, within the core of the large-scale eastern basin eddies.

The westward transport associated with the modeled eastern eddies for August 1998 is evident in vertical section across the Haida eddy core (black transect Fig 3.17a) of tracer concentration (Fig 3.17c), Temperature (Fig 3.17d) and Salinity (Fig

3.17e). In agreement with observational studies (Crawford, 2002 [23]; Tabata, 1982 [97]), Haida eddies (and Sitka not shown here) are characterized by an anticyclonic rotation, represented in Fig 3.17a by a positive SSH anomaly. These eddies show a warmer and less saline core than the surrounding water (Fig 3.17d-e), with a local maximum in temperature around 100m depth. The vertical section of the passive tracer (Fig 3.17c) shows that the excess of heat and fresh water in the eddy core is advected from coastal region. This also suggests that other important biochemical quantities can be advected from the coast into the gyre interior, both at the surface and in the subsurface. In the model experiments, the passive tracer is initially set to 1 within a volume that extends 50km from the coast and 50m below the surface. Therefore the presence of a coastal passive tracer (Fig 3.17c) below 50m confirms the results by Combes and Di Lorenzo (2007) [20], who suggest that eastern eddies develop and propagate offshore following a downwelling event at the coast. Finally, Fig 3.17b quantifies the excess of heat inside this particular Haida eddy. Identical to Crawford (2005) [24], the excess of heat in the first 500m is calculated as the excess of heat within a volume associated with a Gaussian function (red fitted curve in Fig 3.17b). Consistent with the results of Crawford (2005) [24], the excess of heat is estimated at around $100 \ 10^{18}$ J between the surface and 500m deep.

Confident that the model realism is adequate to investigate the cross-shelf transport statistics, we consider the transport of the passive tracer across a transect that follows the coast along the edge of the region of high SSH standard deviation (Fig 3.16d, black line). The cross-shelf exchange across this transect is defined as the advection of the surface passive tracer (P) by the component of the surface velocity normal to the transect (U), where a positive value of the passive tracer flux UP is directed towards the gyre interior. The temporal evolution of the total surface flux across this transect, as visualized by a Hovmuller diagram from 1965-2004 (Fig 3.18a), shows significant interannual variability and little spatial coherence along the

transect. We now decompose the total flux into:

$$UP = \bar{U}\bar{P} + U'\bar{P} + \bar{U}P' + U'P'$$

where the anomalies (U', P') are defined by removing the monthly cycle (latter called "seasonal cycle") $(\bar{U}, \bar{P})$. The time average of the flux terms $\overline{UP} = \overline{\bar{U}\bar{P}} + \overline{U'P'}$ (Fig 3.18b), show that the mean total advection at the surface is mainly explained by its seasonal mean $(\overline{\bar{U}\bar{P}})$. Along the eastern basin, the negative value of $\overline{\bar{U}\bar{P}}$ along the transect corresponds to an on-shore advection and is consistent with previous papers showing predominant downwelling conditions at the coast. Fig 3.18b also shows that the mean offshore advection is associated with the mean eddy-flux $(\overline{U'P'})$. In the western basin, both the advection of tracers by the average flow and the mean eddy fluxes contribute to the mean offshore advection. The seasonality of $\bar{U}\bar{P}$ and $U'P'$ is illustrated in Fig 3.18c at five locations along the transect. The budget of tracer advection integrated over the top 100m (not shown here) has also been performed and shows similar results.

The spatial patterns of the surface passive tracer seasonal variability can be summarized by the March and September means (Fig 3.19a and b). A strong seasonal variability of the surface passive tracer is evident both in the southern edge of the Alaskan Stream and off the Vancouver Island, consistent with the advection of tracer across the transect (Fig 3.18). South of the Alaskan Peninsula, the surface passive tracer is advected southward with a maximum advection in September. Off the Vancouver Island the passive tracer is advected offshore toward the interior of the GOA basin in September (Fig 3.19b), whereas in March (Fig 3.19a), the surface passive tracer is confined along the coast. The seasonal patterns of the passive tracer closely track the ones observed in satellite Chlorophyll-a (measured by SeaWiFS satellite; Fig 3.19c and d), supporting the hypothesis that offshore transport is the primary mechanism controlling the seasonal Chlorophyll maxima in the offshore waters of the
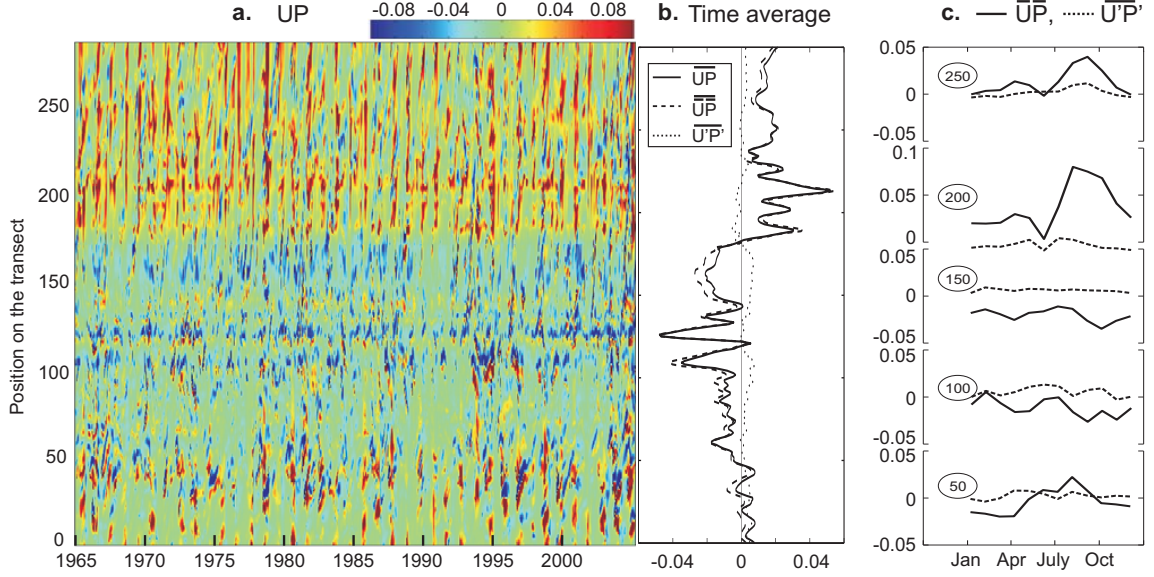
Figure 3.18: (a) Hovmoller diagram of the tracer advection (UP) (ms^{-1}). (b) The time average of UP, $\bar{U}\bar{P}$, and $U'P'$ along the transect. (c) The seasonal variability of $\bar{U}\bar{P}$ and $\overline{U'P'}$ at locations 50, 100, 150, 200, and 250 on the transect (black line in Fig 3.16d).

GOA (Crawford et al., 2005 [25]). It is important to note that Fig 3.19 shows a comparison between a surface passive tracer with an active tracer (chlorophyll-a), which can explain the difference observed off the Vancouver Island.

To explore the interannual variability of the cross-shelf transport, we examine the time series of tracer and tracer flux concentration anomalies, where the anomalies are defined by removing the seasonal cycle ($(UP)_{anomaly} = U'\bar{P} + \bar{U}P' + (U'P')_{anomaly}$). The interannual variability of the flux term ($(UP)_{anomaly}$; Fig 3.20), shows that the dominant term is anomalous advection acting on the mean tracer concentration ($U'\bar{P}$; blue line) with important contribution also from the eddy flux anomaly ($(U'P')_{anomaly}$; black line). This result is consistent along all the locations on the transect, both in the eastern (Fig 3.20a) and western basins (Fig 3.20b). Okkonen et al (2001) [72] show that eddy variability does not correlate with large scale atmospheric forcing in the western basin while in the eastern basin eddy variability is modulated by changes in the surface winds. In particular Okkonen et al (2001) [72] and Combes and Di
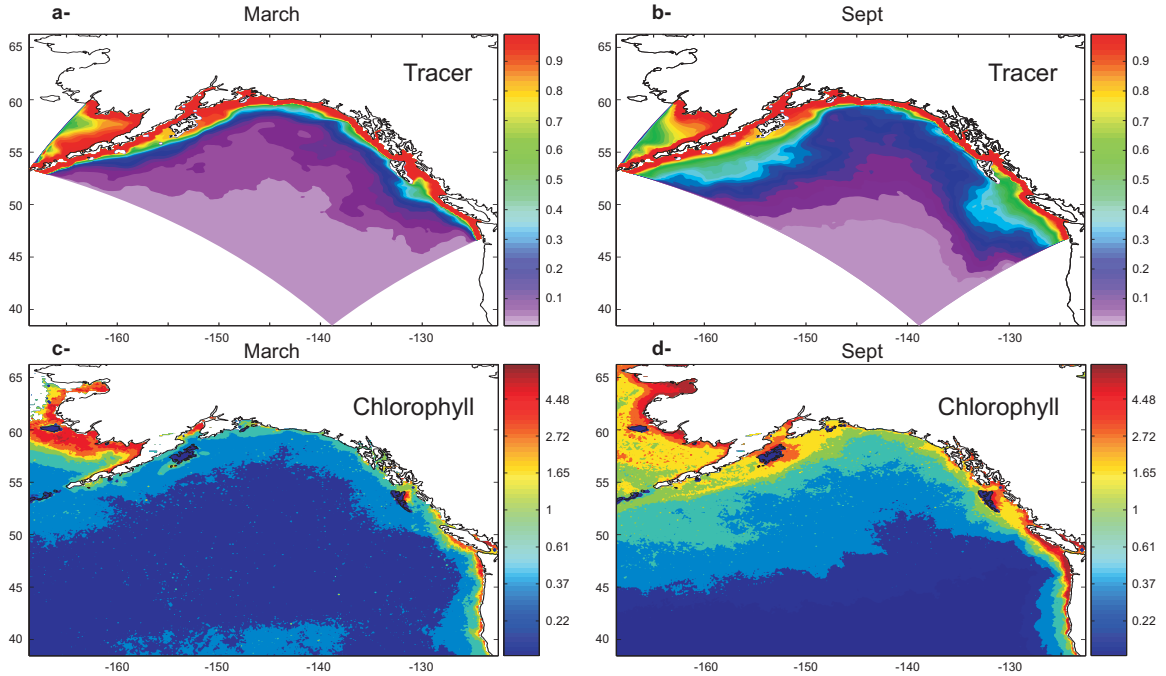
Figure 3.19: Surface passive tracer for (a) March and (b) September. Observed surface chlorophyll concentrations (mg.m^{-3}) for (c) March and (d) September.

Lorenzo (2007) [20] show strong mesoscale eddy activity in the eastern basin during years in which wind forcing promotes strong downwelling. When discussing eddy transport, it is better to use the depth-integrated passive tracer rather than a tracer concentration at the surface or at a certain depth. From now, the term "Tracer" will refer to the depth-integrated tracer over the entire water column.

We first explore regions of high SSH standard deviation in the western basin. Fig 3.21a shows the time series of tracer anomaly for the location represented by a black star on fig 3.21b lag zero (153.28W, 55.11N) from 1965 to 2004 and exhibits a strong interannual variability. Fig 3.21b (lag 0) shows a composite analysis of the SSH during times when the depth integrated tracer concentration anomalies at (153.28W, 55.11N) are greater than 90 (red line on Fig 3.21a). The sequence of maps of SSH at different lag with respect to the time when the tracer anomaly is high, shows the formation and propagation of an anticyclonic eddy-like feature, implying that high anomalous coastal passive tracer found along the western basin is mainly associated with eddy
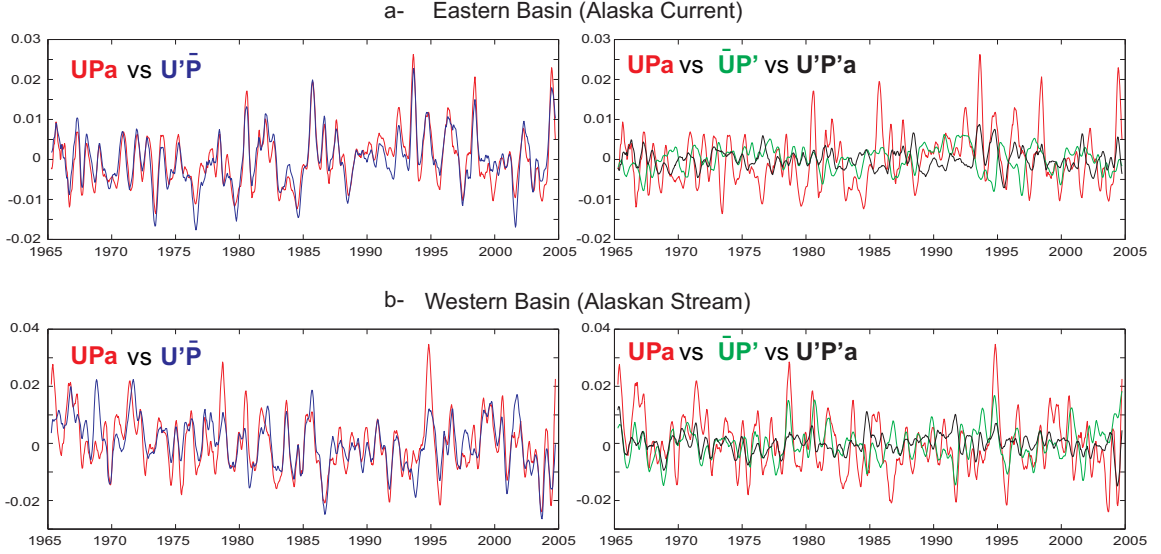
Figure 3.20: Components of UP anomaly (UPa; red line) along the (a) Alaska Current and (b) Alaskan Stream

variability. These types of features are found all along the western basin and advect coastal water, both in their center and periphery, along the Alaskan Stream.

Previous studies have suggested that variability in oceanic circulation and eddies generated on the eastern GOA is modulated by changes in the wind stress (Melsom et al, 1999; [66] Combes and Di Lorenzo, 2007 [20]). On a decadal time scale, along the Alaska Current, changes in wind stress are associated with changes in the PDO index. The PDO index is negative from 1950 to 1976 and principally positive from 1977 to 2000. The positive phase of the PDO is associated with an enhancement of the Aleutian low pressure system over the North Pacific.

To establish the link between the different phases of the PDO and offshore transport, the changes in tracer concentration are computed as the difference between the passive tracer distribution in the period 1977-82 and in the period 1971-76. The eastern GOA shows a significant change in tracer distribution following the 76-77 climate shift (Fig 3.22a). Fig 3.22a shows an increase of passive tracer advection to the interior of the gyre when the Aleutian low pressure is strengthening. The advection is more pronounced west of the Sitka region and west of the Queen Charlotte

54
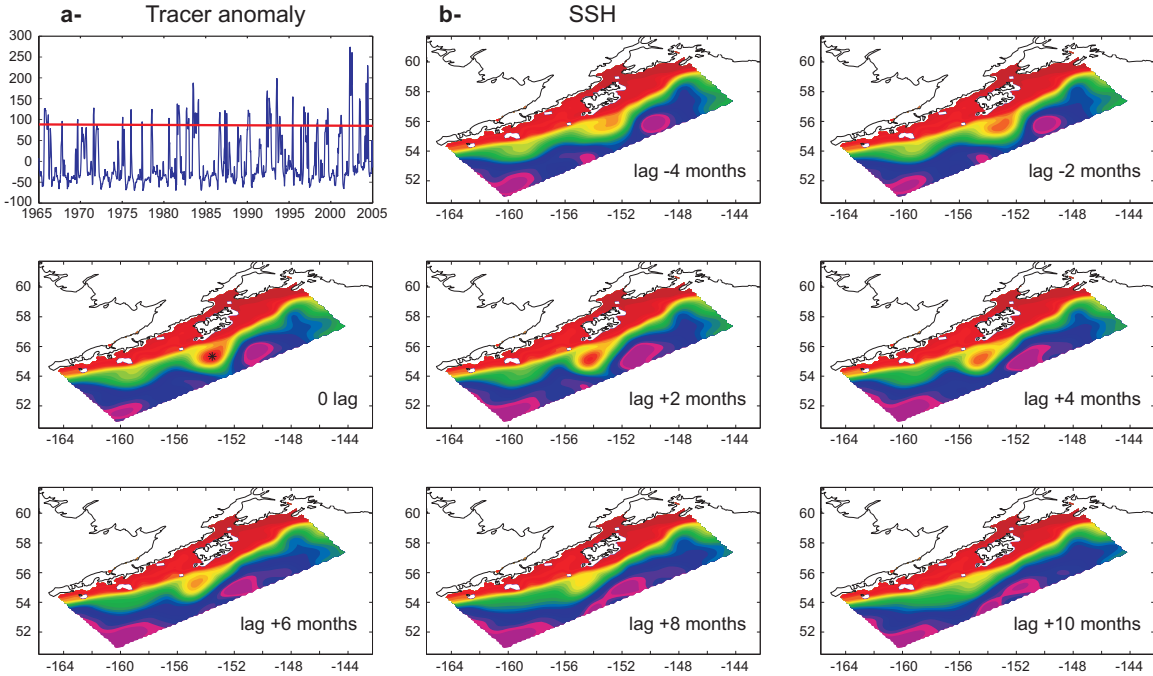
Figure 3.21: (a) Tracer concentration anomaly at (55.11N, 153.28W) [black star in (b)]. (b) SSH composite maps for tracer anomaly. 90 [red line in (a)].

Island, where Sitka and Haida eddies are generated. Changes in atmospheric forcing also produce a change of the surface coastal current. An intensification of the surface current is found in the eastern basin, associated with the 76-77 climate shift, leading to a stronger advection of passive tracer. In contrast in the western basin, interannual variability in the tracer concentration (shown previously) does not seem to respond to changes of surface forcing associated with the climate shift.

To further clarify the relationship between tracer distribution and PDO, we quantify the PDO effect by correlating the tracer concentration with the PDO index (Fig 3.22b). Fig 3.22b shows the spatial distribution of tracer 2 months after the PDO affects the ocean surface. The map shows principally two regions of high correlation between the tracer and PDO. These regions are located on the path of the Haida and Sitka eddies which advect the passive tracer trapped in their core. This is also evident in timeseries of SSH, tracer concentration along the path of the Haida and Sitka eddies and the PDO index (Fig 3.22c and d). These results corroborate the hypothesis
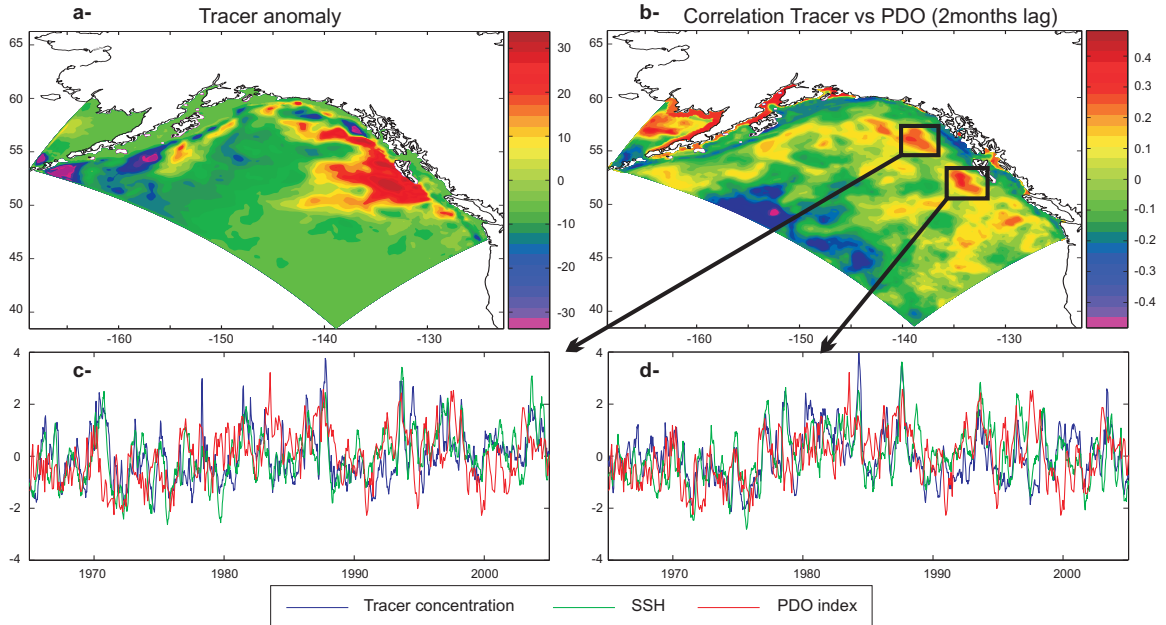
Figure 3.22: (a) Tracer distribution associated with the 1976 77 climate shift. (b) The correlation between the PDO index and tracer concentration (lag 2 months). Comparison between the tracer (blue), SSH (green), and PDO index (red) at (c) Sitka and (d) Haida

that the PDO explains much of the decadal variability of the in the eastern basin, and suggest an increase in the mean offshore transport from the eastern coast after 1976-77 climate shift. The weaker correlation between tracer concentration and PDO time series, observed in Fig 3.22c and d after 1998, may be due to the dominance in recent decades of the second mode of variability, known as the Victoria (Bond et al., 2003 [9]) or NPGO mode (Di Lorenzo et al. 2008 [30]).

3.3.3 Conclusions

The passive tracer simulation, analyzed in this section, provides a method to explore the evolution and distribution of coastal water masses into the gyre interior. The general features of the model circulation of the GOA shows consistent results with observational data, in particular both model and satellite data reveal high EKE regions in the western basin, the northern GOA and in the eastern basin where anticyclonic Haida and Sitka eddies develop. Throughout the coastal Gulf of Alaska,

56

the presence of passive tracer within the core of the anticyclonic eddies confirms that eddies advect coastal waters into the gyre interior. This result implies that, in addition to warm and fresh water, eddies also transport oxygen-poor water and important biochemical quantities such as chlorophyll-a (Crawford et al, 2005 [25]), nutrients and micronutrients (e.g. iron), essential for productivity. Along the eastern side of the GOA basin north of the Vancouver Island, the passive tracer analysis shows on average that while the advection of tracers by the average flow at the surface is directed towards the coast consistent with the dominant downwelling regime of the GOA, it is the mean eddy fluxes that contribute to offshore advection into the gyre interior. In the western basin, both the advection of tracers by the average flow and the mean eddy fluxes contribute to the mean offshore advection. The passive tracer distribution in the GOA also exhibits a strong seasonal variability both in the eastern and western basin. On the seasonal timescales, passive tracer is clearly advected toward the interior of the gyre in September. Significant tracer is transported westward, off the Vancouver Island (eastern basin), and southward, south of the Alaskan Peninsula (western basin).

On interannual timescales, the cross-shelf transport in the western region (along the Alaskan Stream) is mainly associated with intrinsic eddy variability. In contrast along the eastern boundary in the Alaska Current region, stronger offshore transport of the passive tracer coincide with periods of stronger downwelling conditions, which trigger the development of stronger eddies. For instance, after the 1976-77 climate-shift when the Aleutian low pressure intensifies and stronger coastal downwelling conditions become predominant throughout the GOA, stronger advection of coastal passive tracer is found in the eastern basin (Fig 3.22a), in particular in the path of coastal eastern eddies, such as Haida and Sitka eddies.

Our results indicate that coastal water, and therefore biochemical quantities, are advected both vertically (upwelling and downwelling) and horizontally (advection by

surface current or eddies) in the Gulf of Alaska. This cross-shelf and vertical transport are essential for the productivity in the basin. The relation between eddy transport and biota has already been observed in the western basin (Okkonen et al., 2003 [73]) and eastern basin (Mackas and Galbraith, 2002). Therefore the increase in cross-shelf transport after 1976-77 climate shift may provide an additional mechanism to explain shifts in species distribution and fish abundance (Mantua et al., 1997 [58]; Litzow et al., 2006 [55]).

CHAPTER IV

THE CALIFORNIA CURRENT SYSTEM (CCS)

4.1 Introduction

The California Current System (CCS) has been extensively studied through several long-term and regional sampling programs and satellite analyses, providing complete physical, chemical and biological data. The CCS has therefore been identified as a typical eastern boundary current system of the North Pacific. The California Current (CC) is a broad (1000 km offshore), shallow (surface to 500 m), relatively slow (10 cm.s-1) and equatorward flow. In the subsurface, the California Under Current (CUC) is a relatively narrow (10-40 km width) and weak (2 - 10 cm.s-1) poleward flow centered between 100 - 300m depth (Hickey 1979 [39], Hickey 1998 [40]). Despites the vast amount of information provided by the California Cooperative Oceanic Fisheries Investigation (CalCOFI), the coarse spatial and temporal resolution of the sampling leave us with an incomplete understanding of the cross-shore transport dynamics of surface and subsurface water masses.

On interannual time scales, large-scale climate modes such as the Pacific Decadal Oscillation (PDO) (Mantua et al., 1997 [58]) and the El Nio Southern Oscillation (ENSO) are often used to explain physical fluctuations in the Northeast Pacific Ocean, through local changes in surface wind stress and poleward coastally trapped Kelvin waves (Enfield, 1987 [31]). However, those two atmospheric modes usually fail to explain important physical or biogeochemical variables variations such as salinity or nutrients upwelling. Di Lorenzo et al (2008) [30] show that, the North Pacific Gyre Oscillation (NPGO) is the primary mode of interannual and decadal variations of salinity, nutrients upwelling, and surface chlorophyll-a in the Northeast Pacific. The

ecosystem in the CCS, characterized by a high productivity driven by the upwelling of cold and nutrient-rich coastal water, also tends to respond to those modes of climate variability. Indeed, changes in ecosystem have already been reported in previous studies and found to be related to large-scale climate variations in the North Pacific such as the PDO (Mantua et al., 1997 [58]; Chavez et al., 2003 [17]; Lavaniegos and Ohman, 2003 [52]), ENSO (Bograd and Lynn, 2001 [8]), the greenhouse warming (Roemmich and McGowan, 1995 [78]; McGowan et al., 2003 [63]) or the NPGO (Di Lorenzo et al., 2008 [30]).

The cross-shore transport variability of coastal water masses, critical in understanding ecosystem dynamics, is examined using a model passive tracer, continuously released at the coast. In order to separate the offshore advection of the surface coastal waters from the offshore advection of the upwelled coastal water, tracer is released separately both at the surface layer and in the subsurface. Therefore, we use the passive tracer as a proxy for offshore transport, coastal upwelling strength and Ekman transport efficiency, which describes the transport of nutrient-rich coastal waters. Finally a south-north exchange, through transport of water masses by the subsurface flow, is also pointed out in this study.

This paper is organized as follows. Section 4.2 describes the model experiments and tracer approach used in this study. Section 4.3 uses the passive tracer statistics to focus on the upwelling low-frequency variability and cross-shore transport of surface and subsurface water masses and in the California Current. Finally, section 4.4 provides a summary and discussion of the Ekman versus Eddy regimes.

4.2   Model and Tracer experiment setup

The upwelling variability and offshore transport dynamics in the CCS is investigated using ROMS ocean model, described in chapter 2. Among others, Marchesiello et al. (2003) [61] or Di Lorenzo et al. (2005) [29] have already used successfully ROMS in

the CCS eastern boundary current system.

Throughout the chapter, the CCS is defined as our model domain that extends westward from the coast of California to 140ºW and northward from 27ºN to 42ºN (fig 4.1). The grid has an average horizontal resolution of 10km with 30 levels in the vertical. The bathymetry of that region is a smoothed version of ETOPO5 (NGDC, 1988). The initial and boundary conditions are obtained from an outer ROMS simulation that encompassed the entire North East Pacific (fig 4.1; westward from the coast to 180ºW and northward from 25ºN to 61ºN). The outer experiment, with same spatial and vertical resolution, has been forced with the last 58 years of monthly-mean wind stress and surface heat flux forcing from the NCEP/NCAR (Kalnay et al. 1996) and uses Levitus Climatology for the initial and boundary conditions. A 58 years spinup run has first been performed. The model experiment for the CCS uses the same surface wind forcing and a corrected heat and freshwater fluxes derived from the outer experiment. Figure 4.1 compares the standard deviation of relative vorticity between the model output and satellite AVISO data. In particular, the California Current System shows high value offshore both in the model and satellite data. South of 30ºS, differences may be due to the effect of the model southern boundary. However, both the spatial pattern and amplitude give confidence in the degree of realism of the model simulation.

The California Current System is a highly productive region, resulting from strong coastal upwelling (Barber and Smith, 1981 [4]). As seen in Combes et al. (2009) [21] for the dynamics of the Gulf of Alaska circulation or in Combes et al. (submitted) for the Peru-Chile Current system variability, the upwelling/downwelling variability is characterized using a passive tracer advection-diffusion equation (chapter 2). To characterize the transport and upwelling of subsurface rich water in the CCS, we choose the source term (Q) such that the passive tracer (P) is set to 1 to the coastal regions, illustrated by the white boxes on each figure, and in the subsurface from
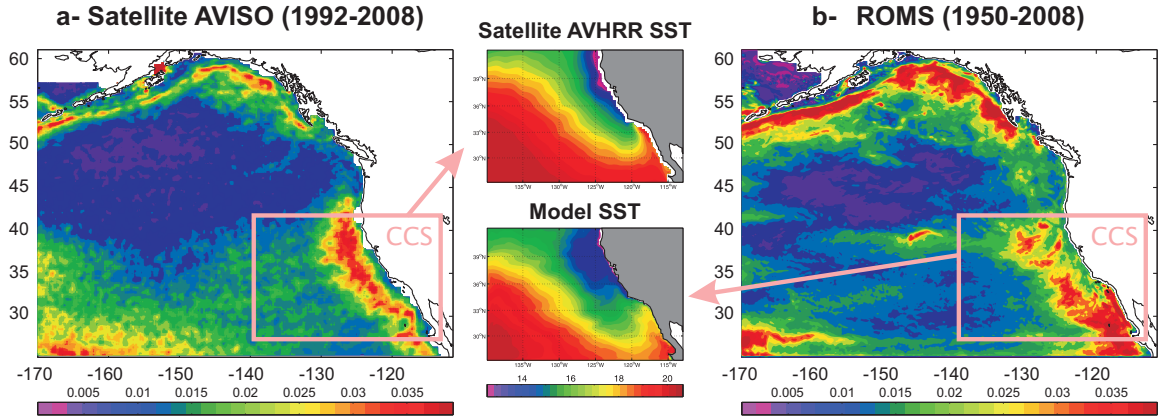
Figure 4.1: Standard deviation of Relative Vorticity for (a) satellite data and (b) ROMS output for the outer grid 2nd column shows AVHRR satellite and model mean summer sea surface temperature (^oC

150 to 250m depth. We decide to separate the two upwelling cells in order to also identify North/South exchanges. Since the tracer is continuously released in the subsurface, the concentration of that tracer found at the surface will be considered as a measure of upwelling. To illustrate the passive tracer approach, figures 4.2a-b shows the distribution of passive tracer continuously released in the subsurface and in the southern region (south of the California bite; white box on fig 4.2a), after fifty seven years of model integration (March 2007). Figure 4.2a shows an advection of tracer at 170m depth both westward and northward. Those south-north and east-west exchanges will be diagnosed in the results section. The vertical section (fig 4.2d) illustrates the importance of mesoscale eddies in the transport of coastal water to the offshore region (positive tracer concentration). Figure 4.2b also indicates that both cyclonic ('C') and anticyclonic ('A') are able to transport coastal water in their core. Later in the study, we will see that most of the tracer is actually advected offshore by cyclonic eddies rather than anticyclonic eddies.

March 2007

a- Tracer concentration at 170 m depth

b- Tracer concentration at 170 m depth

c- Sea Surface Height

d- Vertical section of tracer at 35N
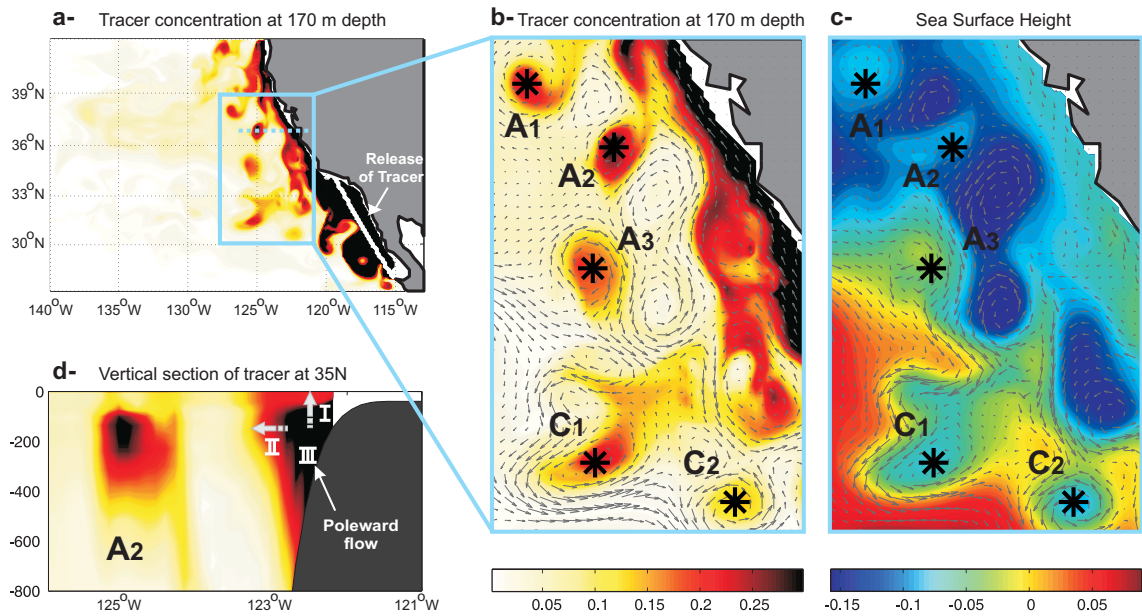
Figure 4.2: White box indicates the region where the tracer has been released in the SUBSURFACE. (a-b) show the tracer concentration at 170m depth for March 2007. (c) shows the sea surface height (in meter) for the same time. A and C on (b) highlight respectively anticyclonic and cyclonic circulations. Arrows correspond to ocean current at (b) 170m depth and at (c) the surface. (d) Vertical tracer section along the blue dash line on (a).
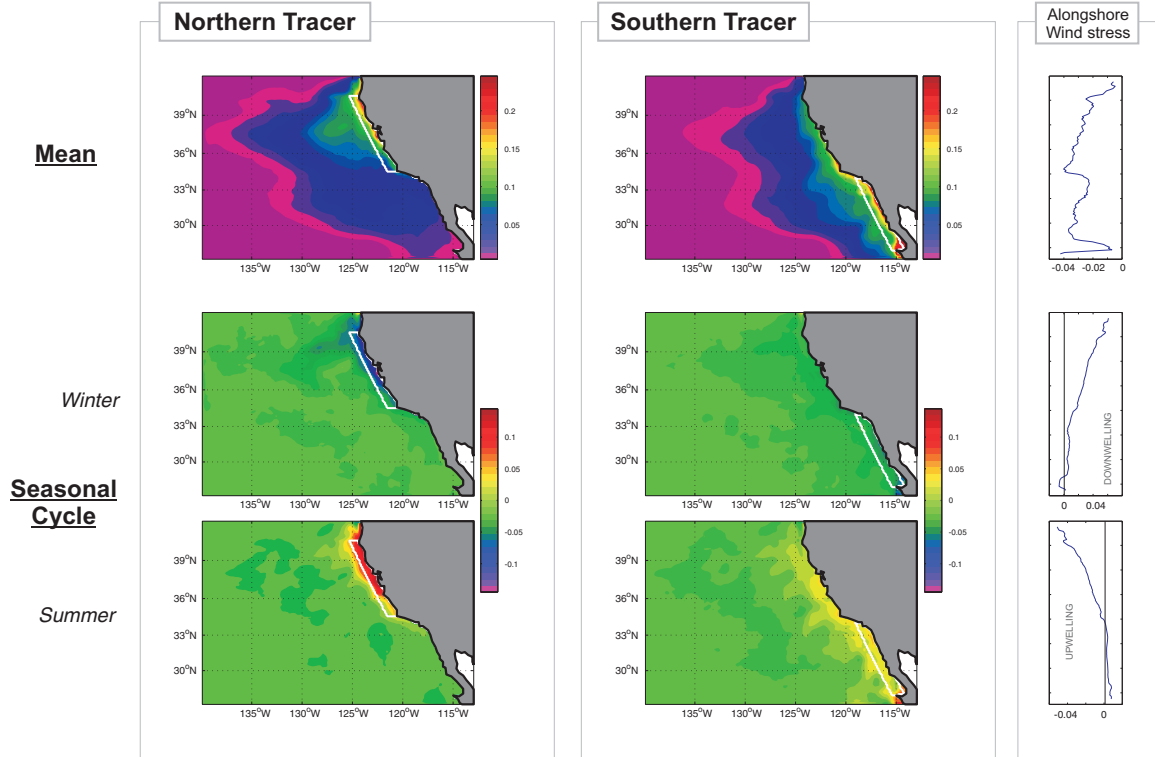
Figure 4.3: White boxes indicate the regions where the tracer has been released in the SUBSURFACE. Mean (1st row) and Seasonal Cycle (winter: 2nd row; summer 3rd row) of the northern tracer in surface (1st column), the southern tracer in surface (2nd column), and the alongshore wind stress (N.m^{-2}; 3rd column).

4.3   Eddy Regime vs Ekman Regime

This study aims to quantify the low frequency dynamic of the cross-shore and along-shore transport in the California Current System. As explained in the previous section, the approach to this problem is to use a regional ocean model and inject a passive tracer, so that the tracer gets advected by the flow field. The source of the tracer is chosen such that the tracer's concentration found at the surface corresponds to an upwelled coastal water mass.

The first row on figure 4.3 shows the mean tracer concentration at the surface for the tracer released in the northern (1st column) and southern (2nd column) regions in the subsurface. Therefore, figure 4.3 shows how much of that tracer has upwelled, averaged over the time of integration. For the northern tracer, we find that, on

average, the tracer is advected offshore after it has upwelled at the coast, rather than in the south, not only do we observe a coastal upwelling but we also find concentration of that tracer in the northern region. Later in the results section, we observe that most of that tracer is carried by the subsurface poleward flow which then upwells in the dominant northern cell.

We now concentrate on the seasonal variability (2nd and 3rd rows on fig 4.3), defined as the anomaly from the mean (1st row on fig 4.3), as explained previously. During the winter season, negative tracer anomalies are found in the northern region, meaning that less upwelling occurs, while in the southern region no evident upwelling/downwelling takes place. During summer, the opposite patterns are observed, with a stronger (from the mean) upwelling in the northern region (positive tracer anomalies). The intensification of upwelling during summer in the northern region can be tracked both with the tracer injected in the north (which directly upwell at the coast) but also with the tracer injected in the south (advected by the subsurface poleward flow and upwell in the northern region during summer). This view of the seasonal upwelling variability, given by the passive tracer approach, is consistent with the seasonal variability in the alongshore wind stress (3rd column on fig 4.3). Indeed the wind stress also shows a strong seasonal variability, in particular in the northern region, with an upwelling favourable anomaly during summer (negative alongshore wind stress).

To explore the link between the upwelling dynamics and the cross-shore transport on the interannual timescale, all following time series are anomalous time series, where the anomalies are defined by removing the mean and seasonal cycle (fig 4.3). Figure 4.4c shows the time series of tracer at the surface, averaged over the white box in figures 4.4a and 4.4b (above the region where the tracer is released), both for the tracer injected in the southern region (green line) and northern region (blue line), which illustrates the amount of subsurface water that upwells into that box.
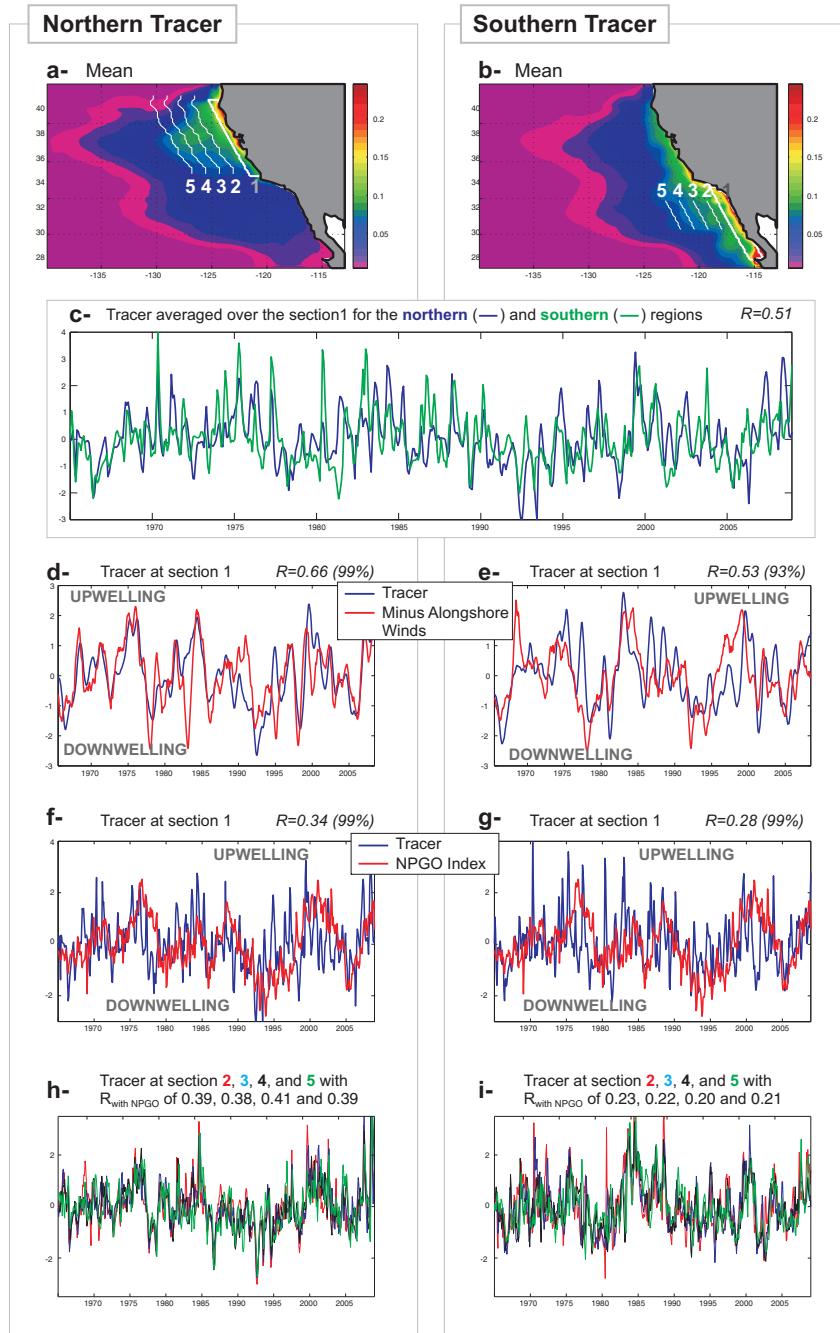
Figure 4.4: The Ekman regime: White boxes indicate the regions where the tracer has been released in the SUBSURFACE. (a) Mean northern tracer and (b) mean southern tracer, as in Fig 4.2. (c) Times series of tracer averaged over the section 1 (coast) for the northern (blue line) and southern (green line) tracers. (d) and (f) compare the norther tracer averaged over section1 with alongshore wind stress and NPGO index (1 year lowpass filter). (h) compares the tracer concentration averaged over each of the transects (correlations are made with NPGO index). (e), (g) and (i) same as (d), (f) and (h) for the southern tracer. Significance of the correlation is shown in parenthesis

66

Both regions exhibit a low frequency variability, raising the question whether these two upwelling centers are actually coherent and whether it is consistent with Ekman dynamics. Figure 4.4c indicates that there is in fact a strong coherence in the upwelling between those two regions with a significant correlation of 0.51 between the tracer concentration averaged over the white box of the northern region (blue line) and southern region (green line). To address whether this upwelling is consistent with Ekman dynamics, we compare the previous time series with the time series of alongshore wind stress (fig 4.4d-e). We find that the interannual variability in the passive tracer concentration and alongshore wind stress are highly correlated for the northern region with a significant correlation of 0.66 and a weaker but still significant correlation of 0.53 for the southern region. Previous studies suggested that the upwelling dynamics in the central and southern California is linked to large-scale climate variability, and in particular with the mode of climate variability, associated with the the North Pacific Gyre Oscillation (NPGO). In our model experiment, we also find significant correlation (0.34 for the northern region and 0.28 for the southern region) between the tracer time series and the NPGO index (fig 4.4f-g). Furthermore, neither the PDO nor the ENSO modes significantly explain the variability of tracer concentration found at the surface.

To identify how much coastal upwelled water is advected in the cross-shore direction, the concentrations of tracer reaching five transects parallel to and at various distances (100-500 km) offshore were computed (fig 4.4). Both in the northern and southern regions, there is significant correlation between the tracer concentration time series at each transect, suggesting that the upwelled coastal water is advected in the cross-shore direction. However, in order to look only at the surface transport dynamics, a similar tracer experiment was performed, in which the same tracer was released in the surface layer, thus removing the upwelling component. Time series of the mean northern and southern tracer concentrations released only in the surface layer (Fig
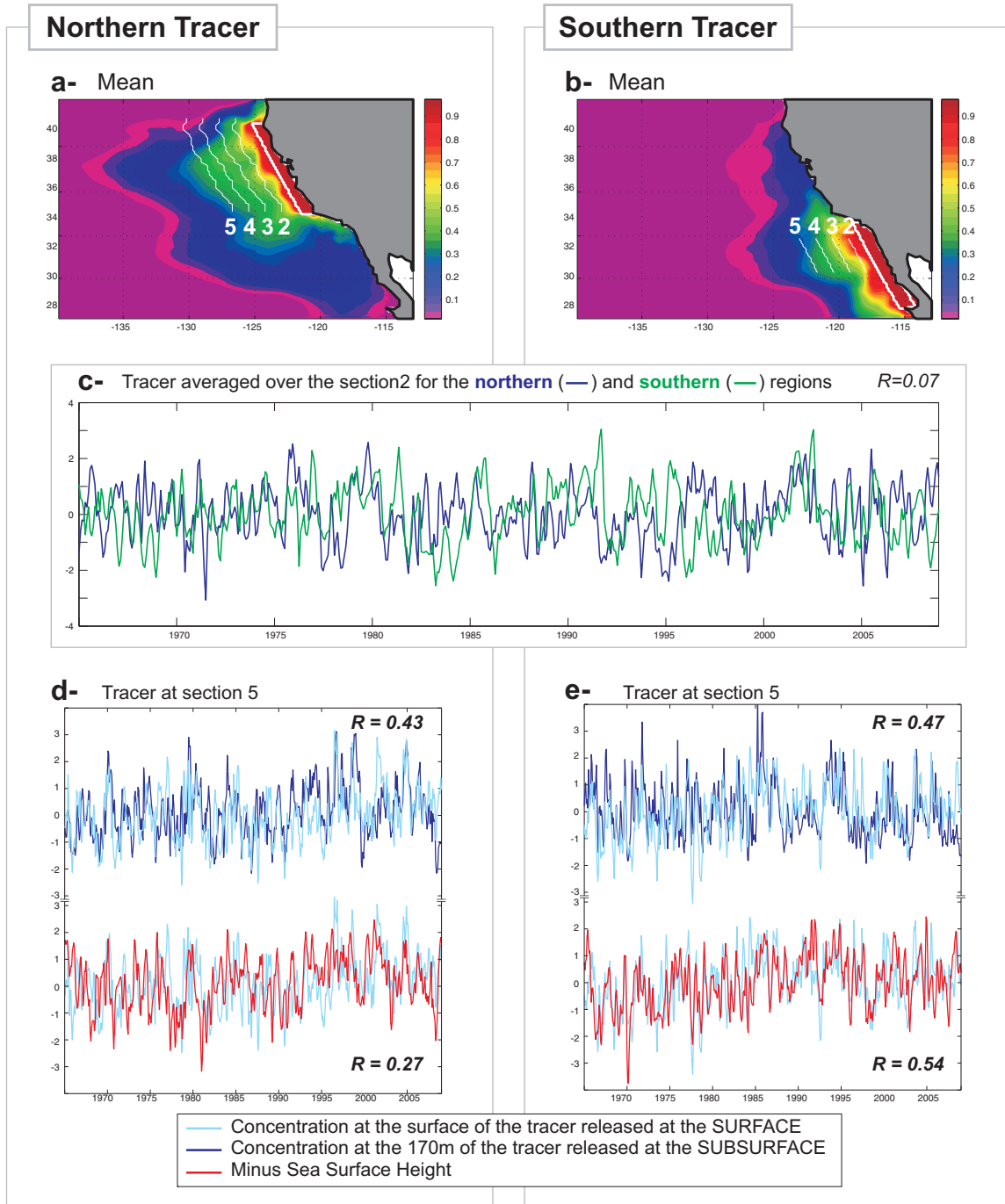
Figure 4.5: The eddy regime: White boxes indicate the regions where the tracer has been released in the SURFACE. (a) Mean northern tracer and (b) mean southern tracer. (c) Times series of tracer averaged over the section 2 (200 km from the coast) for the northern (blue line) and southern (green line) tracers. (d) compares the Sea Surface Height (red line) to the concentration at the surface of the tracer released at the surface (light blue line) and to the concentration at 170m depth of the tracer released at the subsurface (dark blue line), averaged over the section 5. (e) same as (d) for the southern tracer.

4.5a-b) are similar to the mean tracer concentrations released in the subsurface (fig 4.4a-b). For example, the alongshore advection of tracer is less pronounced since it will not be carried by the subsurface poleward flow. By looking at the tracer now released at the surface, the low correlation coefficient on figure 4.5c (R=0.07) indicates that the offshore advection of the coastal water mass is no longer coherent between the southern (green line) and northern regions (blue line). This also suggests that the amount of tracer released at the surface that is advected offshore is not necessarily consistent with the amount of tracer released in the subsurface that is brought to the surface layer by Ekman upwelling. This raises the question of what dynamics control surface transport. There is evidence to suggest that mesoscale eddies, and in particular cyclonic eddies (negative sea surface height anomalies), play an important role in offshore transport dynamics. Indeed, if we compare the concentration of tracer, released in the surface layer (fig 4.5f-g; light blue) and the negative SSHa (fig 4.54f-g; red blue), averaged over the transect 5, we find a significant correlation coefficient of 0.27 (northern tracer) and 0.54 (southern tracer). Figures 4.5f-g also indicate that the surface offshore transport of surface coastal water (light blue line) is significantly correlated to the subsurface offshore transport of subsurface coastal water (dark blue line).

To further illustrate both surface (light blue) and subsurface (dark blue) transport by mesoscale eddies, figure 4.6a shows a composite analysis of vorticity, SSH and tracer concentration (from tracer released at the surface in the northern region) anomalies during times when vorticity anomalies (at 31.5^oN,122.3^oW; white star) are greater than $3.10^{-6}ms^{-2}$ (red line). The SSHa and tracer composite maps imply that high vorticity anomalies are mainly associated with cyclonic eddies (vectors correspond to surface current composite, where vectors are only plotted for positive vorticity or negative SSH composites). The same composite analyses (not shown here) have also been made during times when vorticity is less than $-3.10^{-6}ms^{-2}$,

69
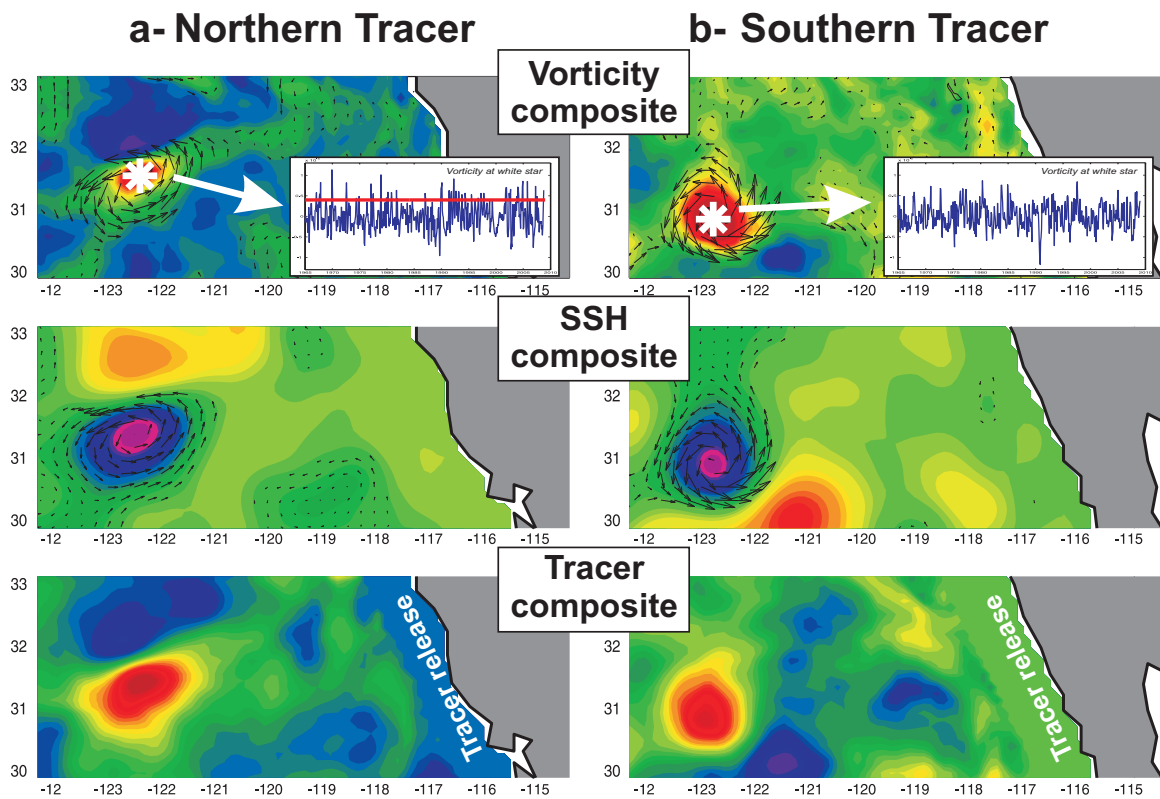
Figure 4.6: 1st, 2nd and 3rd row show composite maps respectively of Vorticity, SSH, and Tracer anomalies during time when vorticity, at the white star, is greater than $3.10^{-6}\mathrm{ms}^{-2}$ (red line on the time series).

and show that on average strong anticylonic eddy features transport negative tracer concentration anomalies. Similar patterns are observed in bothe the northern and southern regions. However, as shown in figure 4.5b, particular events (March 2007) illustrate that anticyclonic eddies ('A1','A2' and 'A3') also transport coastal water (positive tracer concentration). The scatter plots on figures 4.7a-b show the relationship between tracer concentration anomalies (from tracer released in the surface layer) and Okubo-Weiss parameter for each time and point along the transect #5. The Okubo-Weiss parameter (OW) is here defined by:

$$OW = \left[\frac{\partial u}{\partial x} - \frac{\partial v}{\partial y}\right]^2 + \left[\frac{\partial v}{\partial x} + \frac{\partial u}{\partial y}\right]^2 - \left[\frac{\partial v}{\partial x} - \frac{\partial u}{\partial y}\right]^2$$

where a negative Okubo-Weiss parameter corresponds to a high vorticity event. For $OW \leq 10^{-11}ms^{-4}$ and $|Traceranomaly| \geq 0.1$, figures 4.7a-b also separate cyclonic (red circles; positive vorticity) from anticyclonic (blue circles; negative vorticity) events. It clearly shows that most of the eddies transporting coastal waters (positive tracer concentration) are cyclonic (83% in the northern region and 97% in the southern region). This is consistent with the composite analyses described previously, and also points out that some of the tracer can be carried by anticlonic eddies (blue circles), as expected from fig 4.2b. On the contrary, most of anticyclonic eddies transport negative tracer anomalies offshore (82% in the northern region and 88% in the southern region). To illustrate the previous scatter plots, figures 4.7c-e compare southern tracer, Okubo-Weiss parameter and vorticity anomaly fields for the month of March 2007. This comparison highlights a horizontal transport of positive (negative) tracer anomaly by cyclonic (anticyclonic) eddies, where positive tracer concentration is associated with coastal water masses.

A large fraction of tracer released in the subsurface southern region is subsequently found in the northern region (fig 4.8a). Figure 4.8b presents the vertical section of the mean southern tracer at 35ºN (white line on fig 4.8a; no tracer has been released at
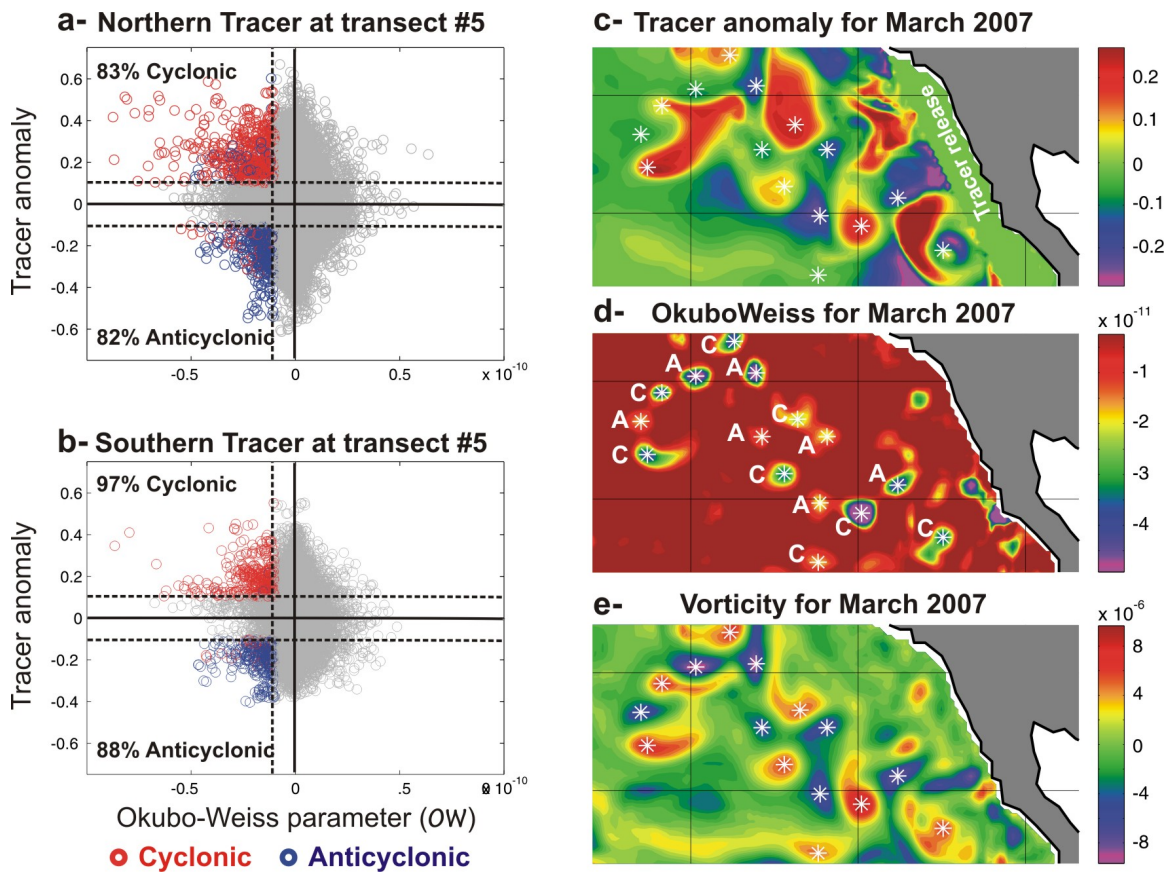
Figure 4.7: 1st column shows a scatter plot, Okubo-Weiss parameter vs. Tracer anomaly at the transect #5, both in the northern (a) and southern (b) regions. A red (Blue) circle corresponds to cyclonic (anticyclonic) circulation. The 2nd column shows a snapshot of Tracer (c), OkuboWeiss parameter (d; in s^{-2}) and Vorticity (e; in s^{-1}) anomalies for March 2007. C and A stand for Cyclonic and Anticyclonic circulation
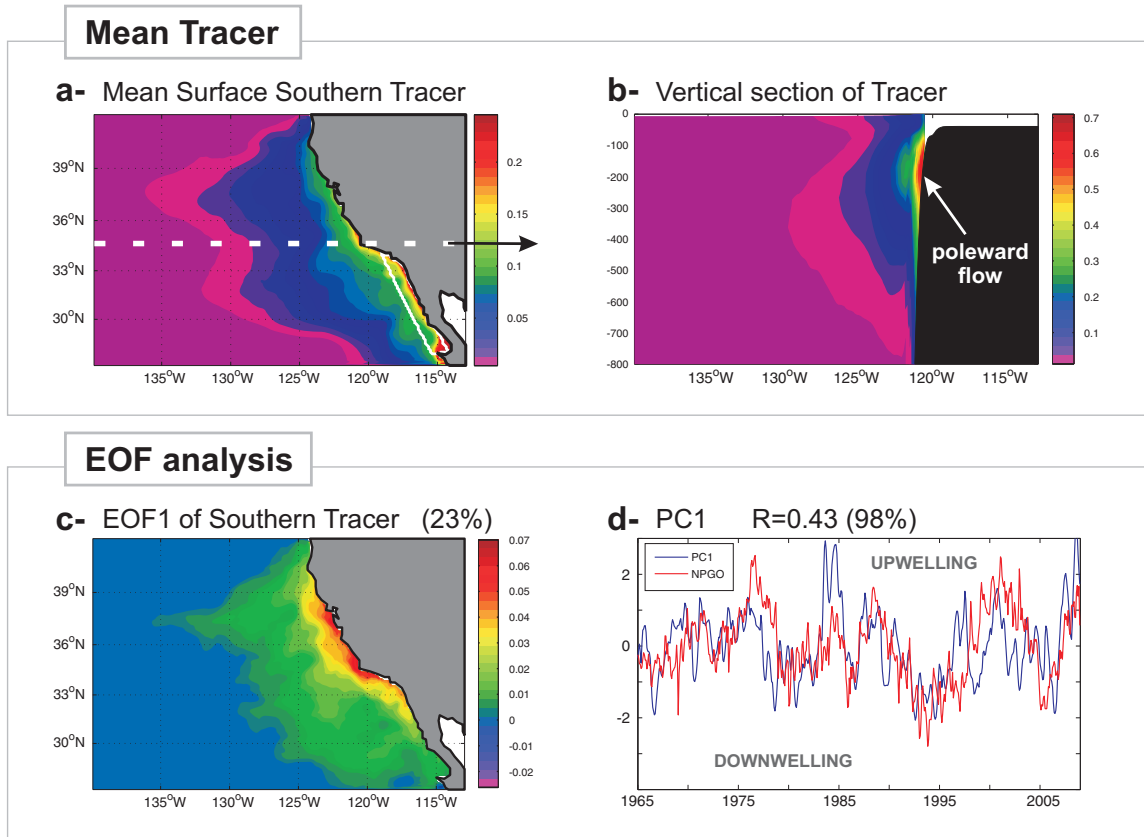
Figure 4.8: White boxes indicate the regions where the tracer has been released in the SUBSURFACE. (a) Mean surface southern tracer. (b) Vertical section of tracer along the dash white line on (a). (c) and (d) shows the first EOF and first Principal Component of the southern tracer

that latitude), showing a strong subsurface south-north exchange (positive value) and the signature of the California Under Current. An Empirical Orthogonal Function analysis (fig 4.8c; EOF) of the anomalous passive tracer concentration shows that the first mode of variability (which explains 23% of the variance) actually corresponds to upwelling occurring in the northern region (the dominant upwelling cell). The subsurface water is therefore advected to the north via the subsurface poleward flow and then upwelled in the northern upwelling system by Ekman upwelling, as mentioned previously. The principal component (fig 4.8d; PC1) also exhibits a low frequency variability. In fact, the PC1, which shows the temporal modulation of the southern tracer upwelled in the northern region, is correlated with atmospheric winds, and in particular with the NPGO. This also implies that the amount of CUC water that upwells in the northern cell is not determined by the magnitude of CUC transport.

The model conditions in March 2007, depicted in Figure 4.2, serve to summarize our findings. Since no tracer has been injected above 34N, the vertical section of tracer at 35^oN (fig 4.2d) shows the signature of the subsurface poleward flow (labelled 'III'; South-North Exchange). This water, originating in the CUC, is characterized by high nutrients, high salinity and low oxygen, and is either (1) upwelled at the coast (labelled 'I') or (2) advected offshore (labelled 'II'). Figures 4.2b-c again show that these coastal waters (positive Tracer anomaly on fig 4.2d) is transported in the subsurface within the cores of cyclonic eddies (negative SSHa), suggesting an important impact of these features on the pelagic ecosystem. This group of eddies have already been reported and often named according to the location of their formation: Meddies (for Mediterranean Eddies; Richardson et al., 2000), Cuddies (for California Undercurrent Eddies; Garfield et al., 1998), or more generally intrathermocline eddies (Gordon et al., 2002; Hormazabal et al, 2010), all having a characteristic high salinity core. It is therefore critical to understand the dynamics of the cross-shore transport and especially mesoscale physical processes (eg thermocline eddies statistics) in order

to predict how the ecosystem will respond to changes in atmospheric and ocean states both at the coast and in the open ocean.

4.4   Conclusion

In this chapter, we use the Regional Ocean Modeling System (ROMS), forced by NCEP/NCAR reanalysis wind stress, to reproduce the dynamics of the California Current System (CCS) and provide a 58 years variability of the system from 1950 to 2007. We have shown that a 10km spatial resolution allows to simulate the mesoscale activity in this region and to capture the characteristics of eastern boundary systems such as the subsurface poleward flow. More interesting, our numerical simulations present a method to track nutrient-rich coastal waters into the gyre interior. Indeed, the vertical and cross-shore transports of coastal water masses have been explored using a passive tracer continuously released at the coast.

A cross-shore gradient of biological quantities has also been observed in previous studies (Bernal 1981 [6], Mc Gowan et al 1996 [64]) and found to be associated with the cross-shore transport of upwelled nutrient. Figure 4.9 illustrates a conceptual summary of the model dynamics and findings from the passive tracer approach, explained throughout the results section. We have shown here that the cross-shore transport is linked to two different regimes: (1) the Ekman regime at low frequency variability which first brings the subsurface water to the photic zone, and (2) the Eddy regime at high frequency variability in which mesoscale eddies transport offshore coastal water masses trapped in their cores. Both horizontal processes have already been mentioned by Plattner et al. (2005) [77] in the context of nitrogen transport. On interannual time scale, the nitrogen concentration at the surface has been observed to be correlated with the low frequency mode of climate variability, associated with the North Pacific Gyre Oscillation (NPGO; Di Lorenzo et al, 2008 [30]). In our study, the NPGO has also been found to modulate the upwelling and
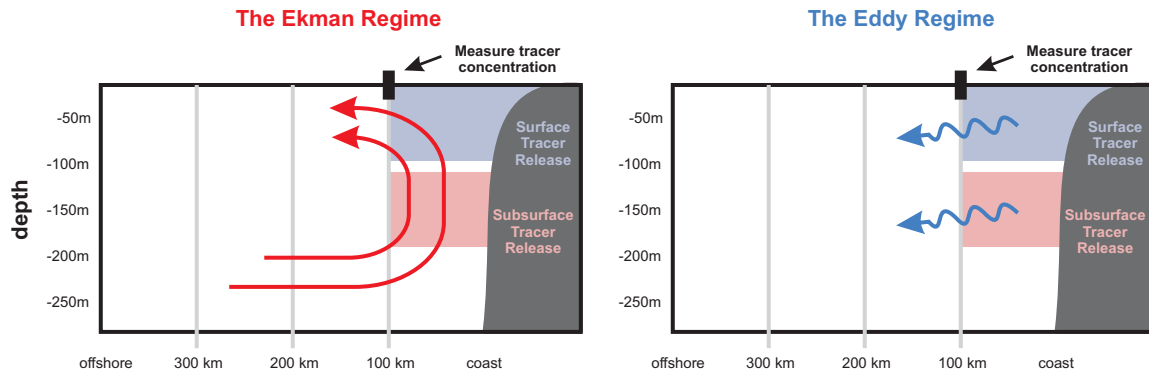
Figure 4.9: Conceptual Summary - Ekman Regime vs Eddy Regime

offshore advection of tracer released in the subsurface. The modeled passive tracer could be considered a proxy for transport of coastal biogeochemical quantities such as silicate, nitrate, or oxygen, which are critical for explaining the CCS ecosystem dynamics.

In addition to a cross-shore exchange, previous studies (Bernal 1981 [6], McGowan et al 1996 [64] ; Venrick, 2002 [102]; Ware and Thomson, 2005 [103]) have also highlighted a northward gradient of some physical, chemical and biological properties in the central and southern CCS. Our results (fig 4.4c) provide evidence that the northern CCS (north of the Southern Californian Bight) is enriched by subsurface coastal water originating in the southern CCS and transported in the core of the subsurface poleward flow. Our simulations also allow to analyze the dispersion and evolution of water having the properties of the subsurface poleward flow, among them high salinity and low oxygen concentration. Our study suggests that some of that nutrient-rich subsurface water is transported offshore by mesoscale eddies both at the surface and in the subsurface.

Information on cross-shore transport statistics is critical for an improved understanding of ecosystem variability. The California Current Ecosystem - Long Term Ecological Research (CCE-LTER) project aims to quantify the cross-shore transport in the southern CCS and its role on retention/loss of nutrients and organisms. Our

study therefore provides a dynamical framework to understand the transport dynamics of the nutrient-rich coastal waters important for biology.

4.5   Current work on the ecosystem variability in the CCS

The Southern California Current Ecosystem has been noticed to respond to low-frequency large-scale climate variability (e.g. PDO, ENSO and NPGO), and by high-frequency mesoscale variability. We will first investigate the change in the ecosystem with respect to the NPGO phases. In collaboration with Fanny Chenillat, we are currently coupling the ROMS ocean model with NEMURO (North Pacific Ecosystem Model for Understanding Regional Oceanography) for the Southern CCS. NEMURO consists of eleven state variables, including two size classes of phytoplankton and three size classes of zooplankton. NEMURO is currently designed for that specific by Qian Li at Scripps Institution of Oceanography. We expect from that modeling study to outline a spatial segregation (inshore/offshore) of the different plankton-size communities, responding to a nutrient gradient in the coastal upwelling region. We therefore also expect that changes in the NPGO phases will enhance/reduce the cross-shore transport of some plankton groups through an Ekman transport and/or an eddy transport. Fanny Chenillat is PhD student from the LEMAR/LPO (Universit de Bretagne Occidentale, France), under the supervision of Dr Pascal Riviere.

CHAPTER V

THE HUMBOLDT CURRENT SYSTEM (HCS)

5.1 Introduction

The eastern boundary system of the Southeast Pacific, referred to as the Humboldt
Current System (HCS; named after the Prussian explorer Alexander von Humboldt),
calls for special consideration due to its high biological productivity and ecosystem
efficiency. The HCS supports approximately 18-20 % of the fish catches worldwide
(http://www.eoearth.org/article/Humboldt_Current_large_marine_ecosystem), for the
most part constituted of anchovies, sardines and jack mackerel (Arcos et al., 2001 [3];
Alheit and Niquen, 2004 [2]). This high productivity region is driven by the upwelling
of cold, nutrient-rich water brought to the surface. Strub et al. (1998) [95] divide the
coastal upwelling system into three different regions according to their disparities in
mean and seasonal cycle. First, an area of year-round upwelling off Peru, which is
stronger in austral winter; secondly, a region of weaker upwelling off northern Chile,
which tends to be stronger in spring and summer; and finally a seasonally strong
upwelling system off central Chile in spring and summer, with downwelling in fall
and winter.

On interannual time scales, the El Nino Southern Oscillation (ENSO) is the lead-
ing mode of variability of the HCS. Previous studies (Hormazabal et al., 2002 [42])
suggest that poleward propagating coastally trapped Kelvin waves, generated at the
equator, play an important role in the upwelling variability. These waves are espe-
cially strong during El Nino events. Shaffer et al., (1997) [84] also speculate on the
possible effects of remote ocean forcing on the marine living resources. For example,
during the waves' downwelling phase, the deepening of the thermocline tends to make

the upper layer warmer and deprived of nutrients, reducing biological productivity.

The open ocean is a nutrient limited region. There is evidence that mesoscale eddies play an important role in the offshore transport of coastal waters, enhancing phytoplankton productivity. Off Central Chile, previous studies using satellite data have shown that the mesoscale eddy activity is associated with higher chlorophyll concentration (Thomas, 1999 [98]) and contributes significantly to the offshore expansion of the area of high chlorophyll concentration (Correa-Ramirez et al. 2007 [22]). The main eddy characteristics (length scales, rotation period, swirl and translation velocities) in the Southeast Pacific are described by Chaigneau and Pizarro (2005) [15] using satellite altimetry and drifter datasets. Characteristics include an offshore velocity varying from $\sim$3 cm.s^{-1} south of 30°S to $\sim$6 cm.s^{-1} north of 15°S. Chaigneau and Pizarro (2005) [15] also point a difference in the orientation of the path between cyclonic and anticyclonic eddies. While cyclonic vortices propagate westward, anticyclonic eddies seems to travel northwestward. Cyclonic and anticyclonic propagation can significantly impact the ecosystem (Levy et al., 2001 [56]) respectively by uplifting nutrient-rich waters to the euphotic zone and pushing nutrient-poor waters out the euphotic zone.

This study aims to better characterize both the interannual coastal upwelling variability and offshore transport statistics. A model passive tracer is used to track coastal subsurface waters. The passive tracer can therefore be used as a proxy for coastal upwelling strength and for transport of nutrient-rich coastal waters. Another objective of this study is to quantify the influence of the equatorial Kelvin waves, in particular their influence during El Nino events when strong downwelling Kelvin waves travel along the coast of South America.

This paper is organized as follows. Section 2 describes the model experiments and the tracer approach used in this study. Section 3 discusses the mean circulation, interannual upwelling variability and cross-shore transport of surface and subsurface

water masses of the HCS. Section 3 will also try to estimate the effects of remote ocean forcing on the upwelling variability. Section 4 provides a summary of the results.

5.2 Upwelling and cross-shore transport interannual variability in the Humboldt Current System

5.2.1 Model and Tracer experiment setup

As for the California Current System and Gulf of Alaska, the ROMS ocean model is used to simulate the HCS. The grid extends southward from 3ºS to 47ºS and westward from the west coast of South America to 92ºW. Based on the spatial pattern of the mean upwelling, we refer to the Peruvian coast as the region between 5ºS-18ºS, the northern Chilean coast as the region between 18ºS-27ºS, and the central Chilean coast as the region between 27ºS and 40ºS. The grid has an average horizontal resolution of 10 km with 30 levels in the vertical and a minimum depth for the model bathymetry of 10m. The resolution is found to be sufficient for capturing mesoscale eddy features (the baroclinic Rossby radius of deformation beeing ∼30km off central Chile and roughly ∼100km off central Peru).

We conduct different model experiments to explore the sensitivity of the HCS upwelling to different air-sea fluxes of momentum and to its remote connection to ENSO, both atmospheric and oceanic (Table 4.1). The model was first spun up for 56 years (EXP_SPIN) with monthly-mean surface forcing from the National Center for Environmental Prediction/National Center for Atmospheric Research reanalysis (NCEP/NCAR; Kalnay et al. 1996 [44]) and initial and boundary conditions from a high-resolution MOM3-based Ocean General Circulation Model (OGCM) code optimized for the Earth Simulator (OFES; Masumoto et al., 2004 [62]; Sasaki et al., 2004 [83]; Sasaki et al., 2006 [82]). The OFES simulation uses a nearly-global domain which extends from 75ºS to 75ºN, with a horizontal resolution of 0.1º and 54 vertical levels, forced by daily-mean surface wind stress, heat, and freshwater fluxes derived from the NCEP/NCAR reanalysis. For the experiments named EXP_NCEP, EXP_ECMWF,

Table 5.1: Table of Experiments

	Run Length	Forcing (Fluxes)	Forcing (Wind)	Initial	Boundary
EXP_SPIN	*1950 - 2005*	*NCEP*	*NCEP*	*From OFES*	
EXP_NCEP	*1950 - 2007*		*NCEP*	*From EXP_SPIN*	
EXP_ECMWF	*1958 - 2002*	*Corrected NCEP*	*ECMWF*		
EXP_NCEP_BRY	*1950 - 2007*		*NCEP*	*From EXP_SPIN*	*Climatology (No Kelvin waves)*

EXP_NCEP_BRY (Table 4.1), the freshwater surface fluxes are set to a corrected monthly climatology derived from EXP_SPIN in which the surface salinity is nudged to the observed climatology and the resulting flux correction is saved. EXP_ECMWF and EXP_NCEP use the final state of EXP_SPIN as initial condition and the output of the OFES experiment as lateral open ocean boundary condition. EXP_ECMWF differs from EXP_NCEP in their surface momentum fluxes, which are prescribed to wind stress derived from the European Centre for Medium-Range Weather Forecasts (ECMWF or ERA40; Uppala et al., 2005 [101]). Finally EXP_NCEP_BRY differs from EXP_NCEP in the boundary condition. While EXP_NCEP uses a time-dependent open ocean boundary condition, EXP_NCEP_BRY uses a climatology state which does not include the presence of equatorial Kelvin waves, in particular important during El Nino years.

The Humboldt Current System (HCS) is a highly productive region, resulting from strong coastal upwelling (Strub et al., 1998 [95]). The upwelling variability, critical to the understanding of the ecosystem dynamics, is characterized using a passive tracer advection-diffusion equation with a decay term as in Combes et al., 2009 (as in chapter 3 and 4). The source term is here such that the passive tracer is set to 1 over a region from the coast to 50 km offshore and in the subsurface from

Spatial distribution of Tracer concentration at 170m for December 2001 from EXP_ECMWF
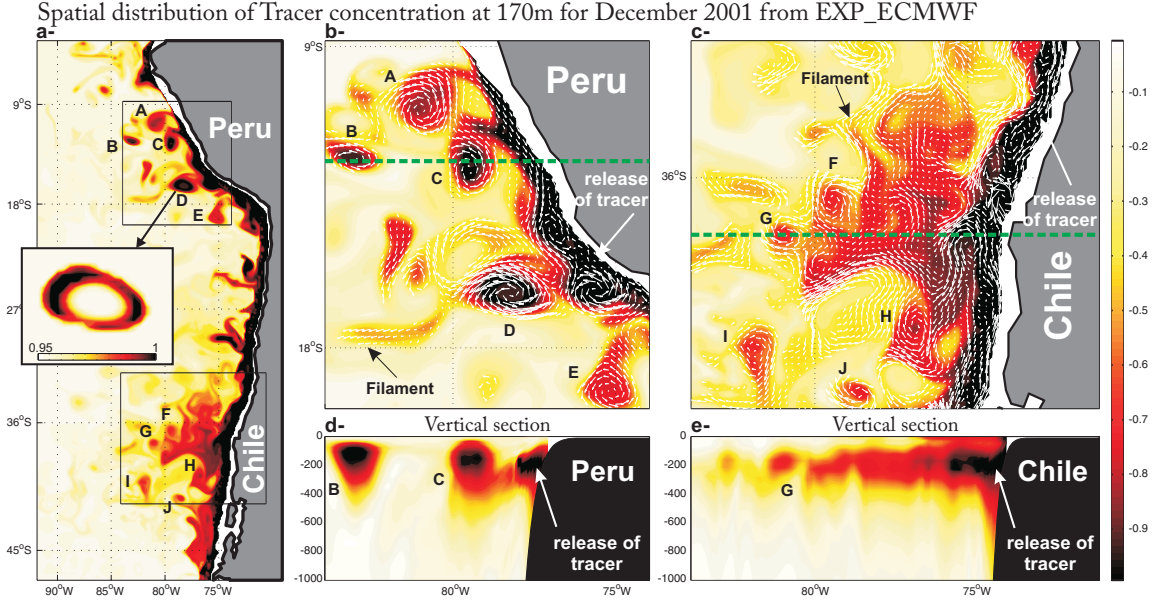
Figure 5.1: (a-c) Tracer concentration field at 200m from EXP_ECMWF for December 2001. White arrows correspond to current velocity at 170m, only plotted when tracer is greater than 0.3. (d) and (e) are the vertical section of tracer along the dashed green lines on (b) and (c)

150m to 250m depth. These depths were chosen to mimic the distribution of nutrient-rich water that is brought to the surface during normal upwelling, while remaining below the pycnocline including when the pycnocline deepens during El Nino events and the passage of coastally trapped waves. We will consider the concentration of tracer found at the surface as a measure of coastal upwelling and refer to it using the term "upwelling". We ask the reader to remember that the terms "upwelling" and "downwelling" indicate the net response in the ocean, rather than the forcing by winds and CTW's.

Figure 5.1 illustrates the passive tracer approach and shows a snapshot from EXP_ECMWF of the passive tracer concentration, averaged over the month of December 2001. The injection of the passive tracer at the coast and in the subsurface, described in the previous paragraph, is clarified on figure 5.1b-e. Figure 5.1a-c shows the subsurface advection of tracer by the flow field (white vectors, only plotted for tracer ≥ 0.3). More specifically, off Peru and Central Chile, figure 5.1b-c points

mesoscale eddies associated with tracer concentration (labelled "A" to "J"), indicating the advection of coastal waters trapped in the eddy cores. Filaments also seem to play an important role in advecting the tracer. The offshore eddy-transport can also be noticed in the vertical section of tracer across mesoscale eddies "B", "C" and "G" on figure 5.1d-e, suggesting the important impact of such features on the offshore mixing of nutrient rich coastal waters (Correa-Ramirez et al., 2007 [22]). Despite a 10km spatial resolution model grid, some of the larger eddies show that the higher concentration of tracer is actually found in the ring of the eddy rather than in the center (eddy "D" in figure 5.1a). This feature is also described by Lvy et al (2001) [56] who show an increase of the phytoplankton biomass in the eddy rings. However, a much higher resolution simulation is necessary to better resolve these sub-mesoscale dynamics.

5.2.2 Mean Circulation of the HCS

Previous modelling and observational studies (Strub et al., 1998 [95]; 5.2) depict the HCS, also known as the Peru-Chile current system (PCCS), as an interaction of three majors and permanent ocean currents: At approximately 45°S, a broad eastward current (West Wind Drift, WWD) diverges into the poleward Cape Horn Current (CHC, south of our model domain) and the equatorward Peru Current (PC). Specific to eastern boundary current systems, a permanent polweward flow also develops in the subsurface off the coast of Peru and Chile, known as the Peru-Chile Under Current (PCUC). It is usually identified by its water mass characteristics (Gunther, 1936 [35]): saltier, richer in nutrients and lower in oxygen than the surrounding water. The principal atmospheric systems that influence those surface currents are the Intertropical Convergence Zone (ITCZ) close to the equator, the South Pacific High in the midlatitudes and polar front storms in the high latitudes (Strub et al., 1998 [95]).
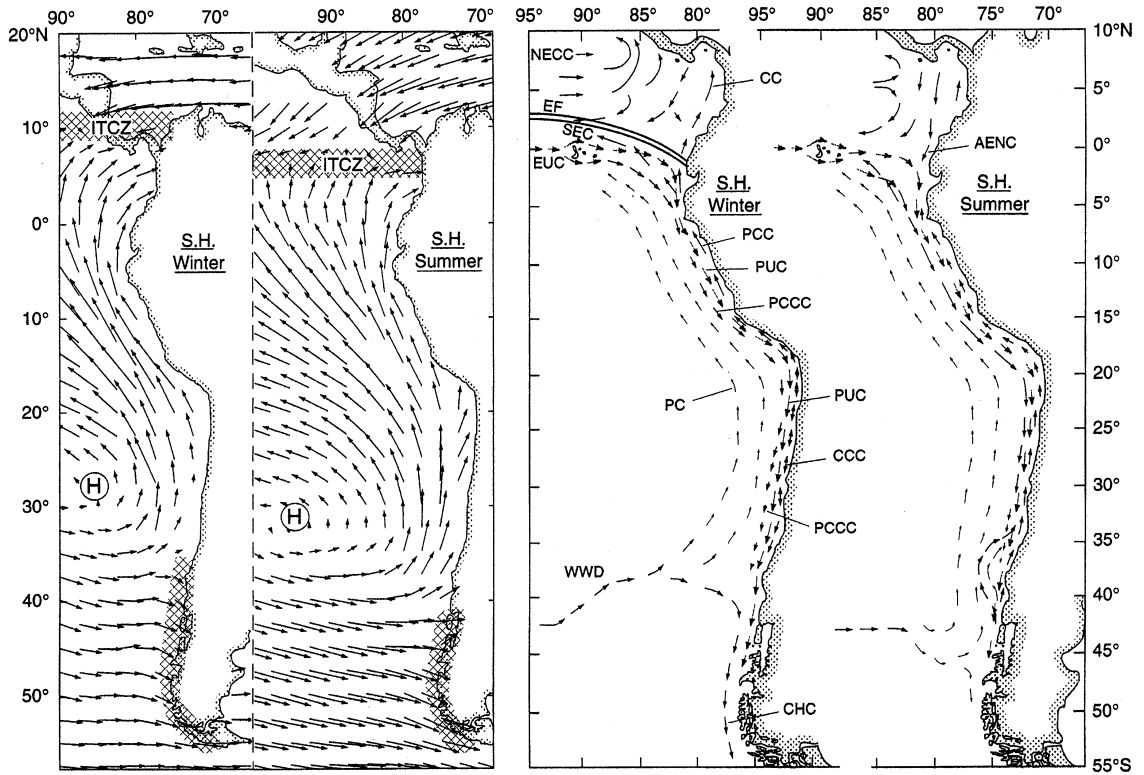
Figure 5.2: Fig 10.2 of Strub et al 1998: Climatological winds and currents during austral winter and summer. Winds are from the NCEP reanalysis at 1000mb, averaged over austral summer (December-February) and winter (June-August). Regions of heavy precipitation are shown by hatching. Schematic vectors are drawn to indicate the location and relative strengths of the currents. Subsurface currents are shown in gray. The primary currents of interest (starting offshore) are the West Wind Drift (WWD), the Peru Current (PC), the Peru Chile Countercurrent (PCCC), the Poleward Undercurrent (PUC), the Peru Coastal Current (PCC), the Chile Coastal Current (CCC) and the Cape Horn Current (CHC)
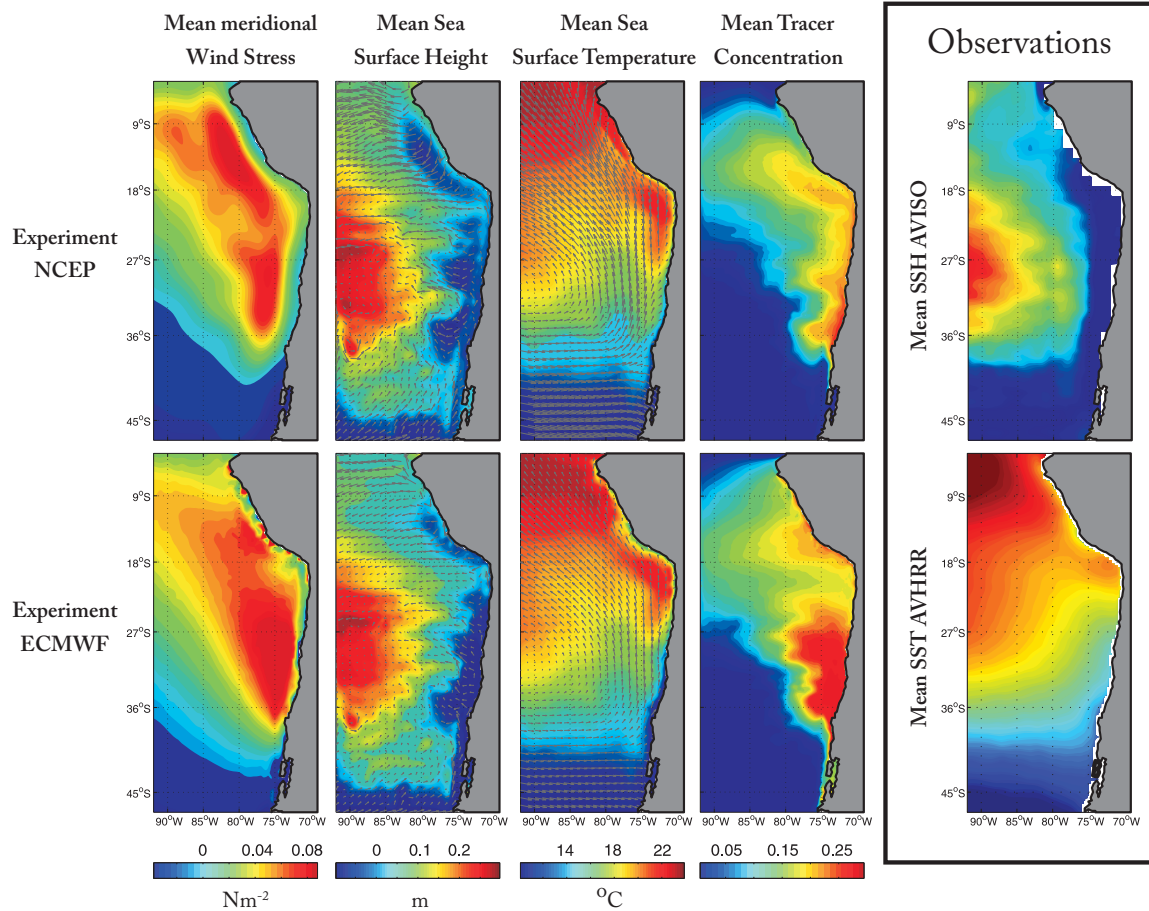
Figure 5.3: Means of meridional surface wind stress (1st column), sea surface height (SSH, 2nd column), sea surface temperature (SST, 3rd column) and surface tracer concentration (4th column), both from EXP_NCEP (1st row) and EXP_ECMWF (2nd row). Maps of AVISO SSH and AVHRR SST satellite are shown on the 5th column. Superimposed on the SSH and SST fields, vectors show respectively the mean surface current and mean surface wind stress

The mean of the meridional component of the surface wind stress used to force the model experiments is shown in Figure 5.3 (1st column). The ECMWF satellite mean meridional wind stress shows three distinct regions at the coast, with local maxima of upwelling-favorable winds off Peru (around 14ºS) and central Chile (around 30ºS) and a region of weak positive (equatorward) meridional wind off northern Chile. In particular off Chile, we can notice a narrow decrease next to the coast of the meridional winds. This view is also consistent with wind stress derived from the QuikSCAT/SeaWinds Scatterometer Data Products (not shown here). Even if satellite QuikSCAT wind stress is known to provide a more accurate and realistic coastal wind stress, its time range (September 1999 to Present) is less appropriate in the discussion of the interannual ocean variability, and also misses the strong El Nino events in 1982-83 and 1997-98. Therefore no experiment using QuikSCAT surface forcing will be analyzed in this study. While the spatial pattern of the ECMWF wind reanalysis is consistent with that from QSCAT, important differences appear with the NCEP mean meridional wind stress at the coast. Those differences in the air-sea fluxes of momentum between NCEP and ECMWF are reflected in the coastal SSH (Figure 5.3; 2nd column). For EXP_ECMWF, the mean SSH response in Figure 5.3 shows a band of negative anomalies along the coast and at the southern boundary, which generates the equatorward PC and the eastward WWD at the surface. This spatial SSH pattern is consistent with satellite observations (5th column on figure 5.3, derived from AVISO satellite maps available at http://www.jason.oceanobs.com) and surface drifters (Niiler et al., 2003 [71]). Off the coast of Peru, this minimum in SSH is nevertheless slightly located offshore in EXP_NCEP, consistent with the curl of the NCEP surface wind stress. Even though the mean SSH from EXP_NCEP has major coastal differences with observations, we will see later that its temporal variability is highly correlated with coastal in-situ data.

By using the presence of passive tracer at the surface to indicate upwelling, experiments EXP_ECMWF suggests that those atmospheric conditions produce a mean strong upwelling off Peru, persistent but weaker upwelling off northern Chile, and strong upwelling off central Chile (Fig 2; 4th column), also suggested by Strub et al., 1998 [95]. On the other hand, the weak coastal NCEP wind stress clearly does not allow distinguishing those three regions from the mean surface tracer. The same difference in the upwelling cells can also be observed in the mean Sea Surface Temperature (SST) fields (Figure 5.3; 3rd column). Indeed while EXP_ECMWF show bands of cold water off the coasts of Peru and central Chile (consistent with AVHRR-AMSR SST satellite maps, 5th column), the mean SST from EXP_NCEP does not capture the mean Peruvian upwelling cell (as suggested by the surface tracer concentration).

5.2.3 Interannual Variability of the Peru and Central Chile upwelling systems

To explore the interannual upwelling variability in the Humboldt Current System, we examine the time series of SSH anomalies (SSHa) and tracer concentration anomalies, where the anomalies are defined by removing the monthly mean seasonal cycles. Figure 5.4 shows a comparison of the model coastal sea level height anomalies (blue lines for EXP_NCEP and green lines for EXP_ECMWF) with in situ records (red lines; provided by The University of Hawaii Sea Level Center available at http://ilikai.soest.hawaii.edu/uhslc/data.html) at six different locations along the coast off Peru and Chile: Lobos de Afuera (6°56'S), Callao (12°03'S), Arica (18°28'S), Antofagasta (23°39'S), Valparaiso (33°02'S) and Talcahuano (36°42'S). While figure 5.3 shows the poor representation of the mean spatial pattern of SSH in EXP_NCEP, figure 5.4 indicates that both EXP_ECMWF and (in particular) EXP_NCEP model hindcasts are nevertheless able to explain a significant fraction of the in situ sea level variance, especially off Peru. For example, the model SSHa captures the major positive ENSO events (1982; 1998), represented by a positive peak in the SSHa,
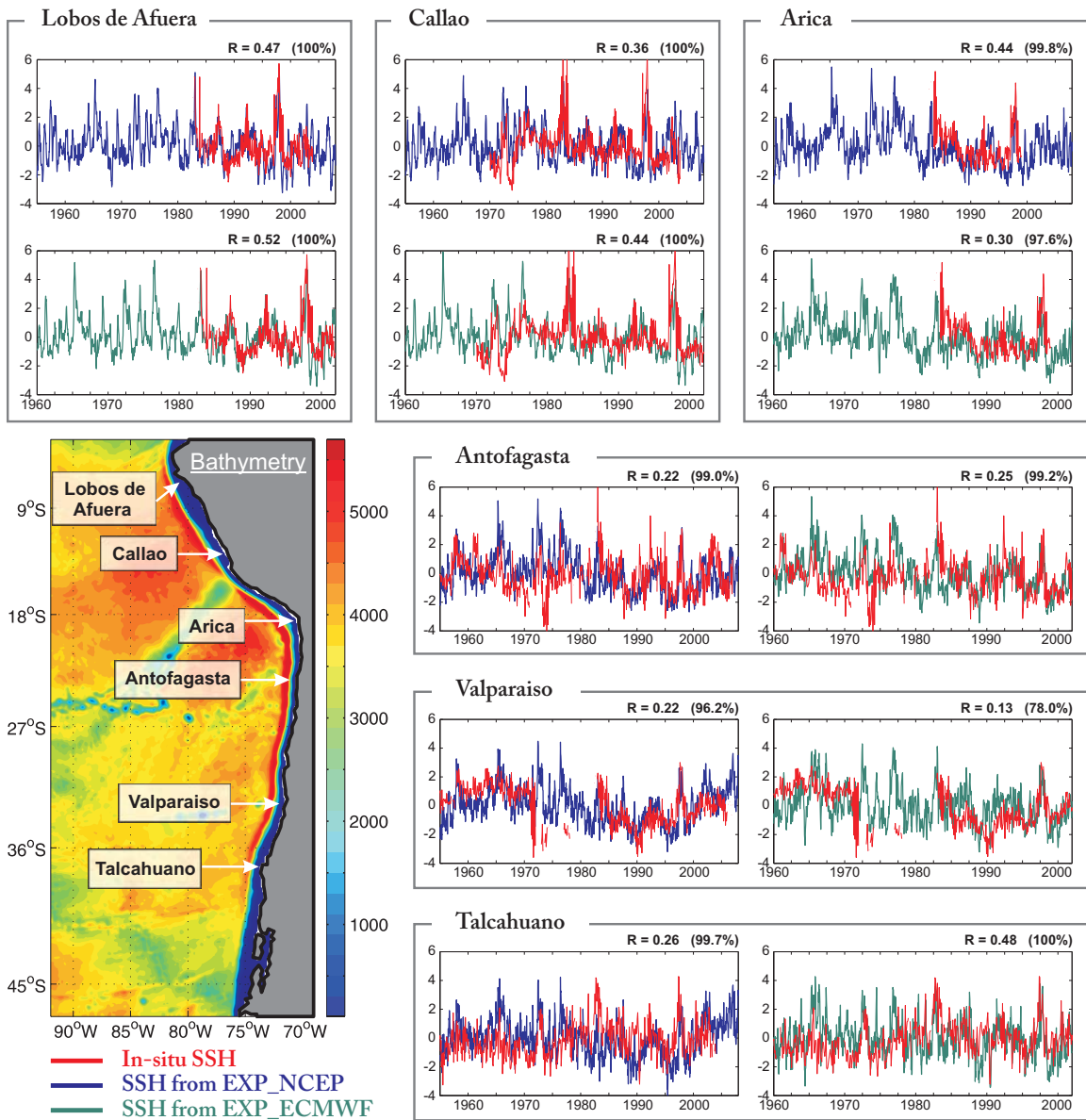
Figure 5.4: Comparison of the coastal deseasonalized SSH for Lobos de Afuera, Callao, Arica, Antofagasta, Valparaiso and Talcahuano between the EXP_NCEP (blue lines), EXP_ECMWF (green lines) output and in situ tide gauge data (red line). Correlations (R) and their significance (in parenthesis) are located above each time series. The ocean bathymetry is shown on the bottom left
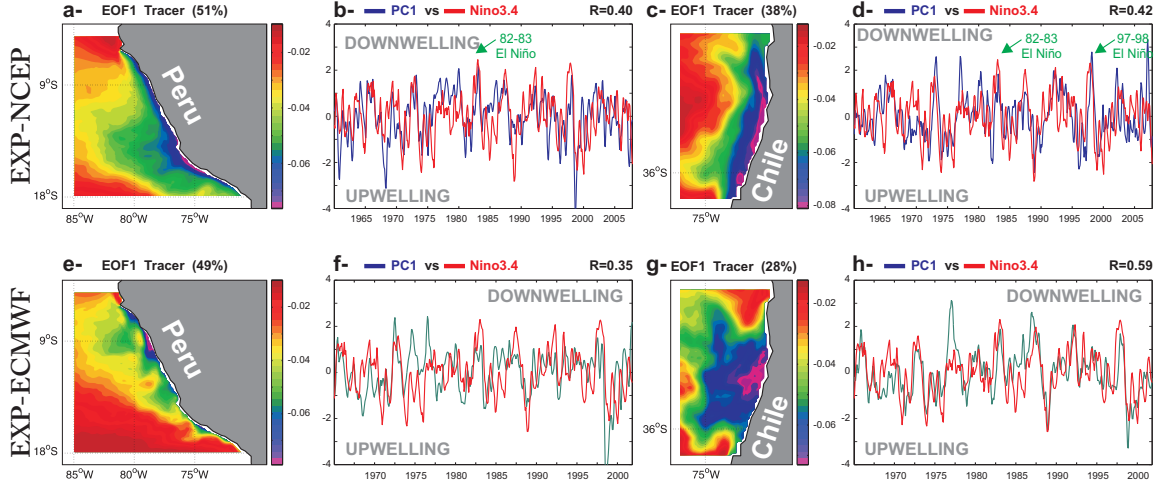
Figure 5.5: Empirical Orthogonal Function (EOF) analysis. First EOF and Principal Component (PC) of passive tracer anomaly concentration off Peru (a-b) and off central Chile (c-d) for EXP_NCEP. (e-h) same as (a-d) but for EXP_ECMWF. The PCs are compared with the Nino 3.4 index (red line)

characteristic of an anomalous downwelling condition.

Confident that the model adequately reproduces interannual variability in upwelling for EXP_ECMWF and EXP_NCEP, we perform an empirical orthogonal function (EOF) analysis of the passive tracer concentration anomaly off Peru and central Chile (fig 5.5). Off Peru, the leading EOF (fig 5.5a,e) explains more than ~50% of the variance and shows a similar spatial pattern between the output of EXP_NCEP (fig 5.4a) and EXP_ECMWF (fig 5.5e) with negative values off the coast. The temporal modulations of these patterns, which are represented by the principal component time series (PC 1; fig 5.5b,f), reflect the variability of the strength of the anomalous coastal upwelling (negative values of PC 1) and downwelling (positive values of PC 1). Both EXP_NCEP and EXP_ECMWF shows that the first mode of variability of the passive tracer (PC 1; fig 5.5b,f) is significantly correlated with the Nino 3.4 index (red lines; R=0.40 for EXP_NCEP, R=0.35 for EXP_ECMWF) with downwelling conditions during positive ENSO events (positive index). Off central Chile, both EXP_NCEP and EXP_ECMWF (fig 5.5c and 5.5g) also displays a first mode correlated with the ENSO (R=0.42 and R=0.59).

5.2.4 Effects of remote oceanic forcing

The previous section illustrated that much of the interannual upwelling variability off Peru and central Chile is caused by the ENSO cycle, using a passive tracer approach. ENSO impacts the circulation through local changes in surface wind stress (Halpern, 2002 [37]) and via coastally trapped Kelvin waves (Pizarro et al., 2002 [76]). Off Peru, the deepening of the thermocline is mostly related to coastal trapped waves of equatorial origin (Hill et al., 1998 [41]), with actually little strengthening of equatorward winds (Halpern, 2002 [37]). Spillane et al. (1987) [91] also supports this hypothesis by looking at the sea level variability and shows that intraseasonal variability (∼50-days fluctuations) off the South American coast is linked primarily to poleward coastally trapped Kelvin waves forced by eastward wind events in the western and central Pacific, more prominent during the onset of El Nio events.

Using the model experiments we now separate the effects of remote oceanic forcing (waves generated at the equator) from local changes in the air-sea momentum flux on the interannual upwelling variability. To do so, we perform two experiments with the same surface forcing and initial condition, one using time-dependent ocean boundary conditions (EXP_NCEP, used in the previous analysis) and the other with prescribed climatological boundary conditions (EXP_NCEP_BRY; see Table 1). In other words, while EXP_NCEP possesses poleward-driven coastally trapped Kelvin wave pulses in its northern ocean boundary, EXP_NCEP_BRY filters the wave signals from the boundaries by prescribing monthly climatological values at the oceanic open boundaries. Since the previous section shows that the interannual variability of SSH from EXP_NCEP shows a good agreement with coastal in-situ measurements, we decide to continue in this section with NCEP surface forcing to be consistent with the OFES run (also forced by NCEP winds) which provides the boundary condition for each of our simulations.

To compare EXP_NCEP_BRY and EXP_NCEP, we first perform the same EOF
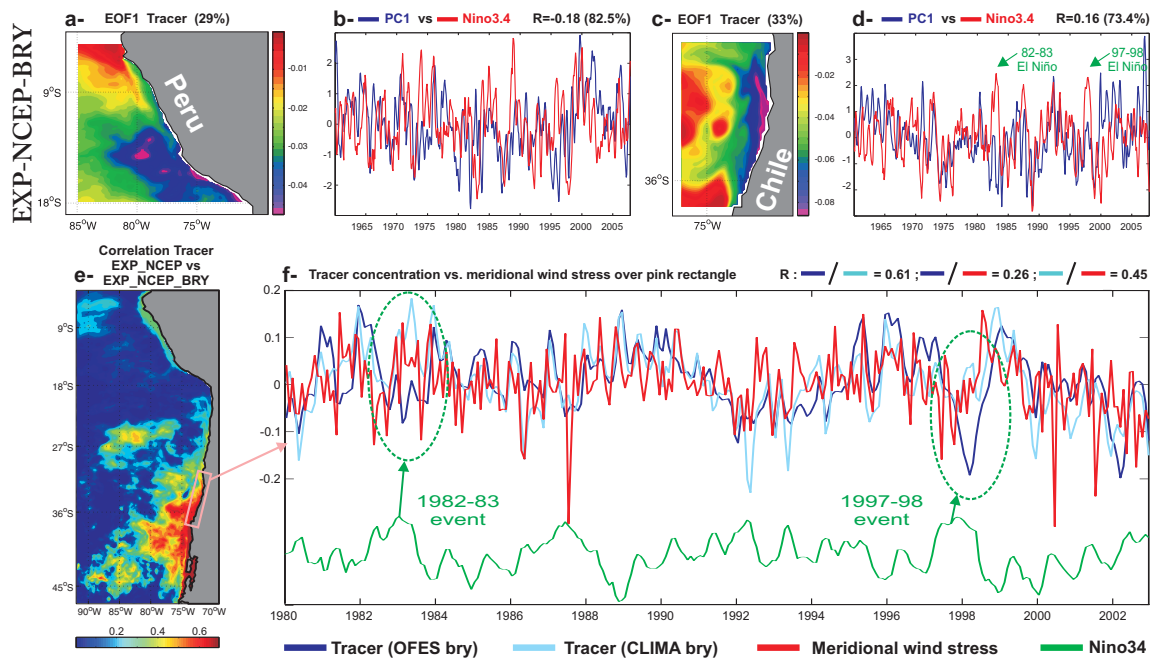
Figure 5.6: (a-d) same as figure 4(a-d) but for EXP_NCEP_BRY. (e) spatial correlation coefficient between the tracer concentration time series of EXP_NCEP and EXP_NCEP_BRY. Averaged over the pink box in (e), (f) compares the time series of anomalous tracer concentration from EXP_NCEP (dark blue) and from EXP_NCEP_BRY (light blue) with the NCEP surface meridional wind stress (red)

analysis for EXP_NCEP_BRY (Fig 5.6a-d) as seen in figure 5.5a-d for EXP_NCEP. Off Peru, the first mode (EOF 1) of anomalous tracer concentration shows a similar spatial pattern between EXP_NCEP (Fig 5.5a) and EXP_NCEP_BRY (Fig 5.6a). However the temporal modulation of that mode (PCs 1; Fig 5.5b and Fig 5.6b), which corresponds to an upwelling variability at the coast, is different. Indeed. when the experiment incorporates waves crossing the model boundaries (EXP_NCEP), we saw (section 3b; Fig 5.5b) that the first mode of upwelling variability is significantly correlated with the ENSO cycle (Fig 5.5b; R=0.40). This relationship does not appear anymore when the experiment excludes remote ocean forcing (Fig 5.6b; with a non significant correlation coefficient of -0.18). Winds drive those patterns of upwelling in both cases. But the equatorial signals modulate the strength of that upwelling by depressing or lifting the local pycnocline.

Off central Chile, the same observation can be made. The first mode of tracer concentration displays a comparable spatial pattern between the two model experiments (Fig 5.5c and Fig 5.6c). However, the correlation between the PCs and the Nino 3.4 index drops from R=0.42 in EXP_NCEP (Fig 5.5d) to R=0.16 in EXP_NCEP_BRY (Fig 5.5d), confirming that this region is also very sensitive to coastally trapped Kelvin waves generating at the equator, in particular during strong El Nino events. Compared to figure 5.5d (EXP_NCEP), figure 5.6d (EXP_NCEP_BRY) indicates in the PC1 that, during both the 1982 and 1998 El Nino events, the strength of the anomalous downwelling is greatly reduced without the presence of those downwelling equatorial Kelvin waves.

To assess the degree of importance of those waves in explaining the coastal upwelling variability, we compute the correlation of the tracer concentration time series between EXP_NCEP and EXP_NCEP_BRY (Fig 5.6e). Figure 5.6e indicates that the equatorial trapped Kelvin waves explain more upwelling variability (low correlation coefiicient) at lower latitude along the coast, decreasing the correlation coefficient

from around 0.7 off Central Chile (south of 30S) to a non significant correlation off Peru. However, even though the correlation off central Chile is as high as 0.7, the temporal upwelling variability is strongly affected by the presence of those waves during strong El Nino events, as seen in the EOF analyses. Indeed figure 5.6f compares the time series of the surface tracer concentration anomaly between EXP_NCEP (dark blue line) and EXP_NCEP_BRY (light blue line), focused on the period 1980-2007 when two major El Nino events occurred (1982 and 1998). The non-perfect correlation (R=0.61) between EXP_NCEP (dark blue) and EXP_NCEP_BRY (light blue) supports the previous idea that the choice of the boundary condition is important in reproducing the upwelling circulation even as south as 35S. The major differences arise during the strong El Nino years (green circles; 1982 and 1998). For example, during the years 1997-98, the surface tracer concentration in EXP_NCEP_BRY (light blue line) increases as a direct response to an increase (ie upwelling-favorable) of the meridional surface wind stress (red line). At the same time, EXP_NCEP (dark blue line) shows a more downwelling condition (decrease of tracer concentration), reflecting the presence of the strong downwelling coastally trapped Kelvin propagating poleward during the El Nino event. Similar dynamic relationships can be seen during the 1982-83 El Nino event. Finally the correlation between the SSH from EXP_NCEP_BRY and coastal in-situ SSH is not anymore significant. Respectively at [Lobos de Afuera, Callao, Arica, Antofagasta, Valparaiso and Talcahuano], the correlation drops from [0.47, 0.36, 0.44, 0.22, 0.22, 0.26] in EXP_NCEP (Fig 5.4) to [-0.06, -0.18, -0.08, -0.04, 0.19, 0.14] in EXP_NCEP_BRY, confirming the high impact of coastally trapped Kelvin waved in the upwelling variability (here in the SSH variability).
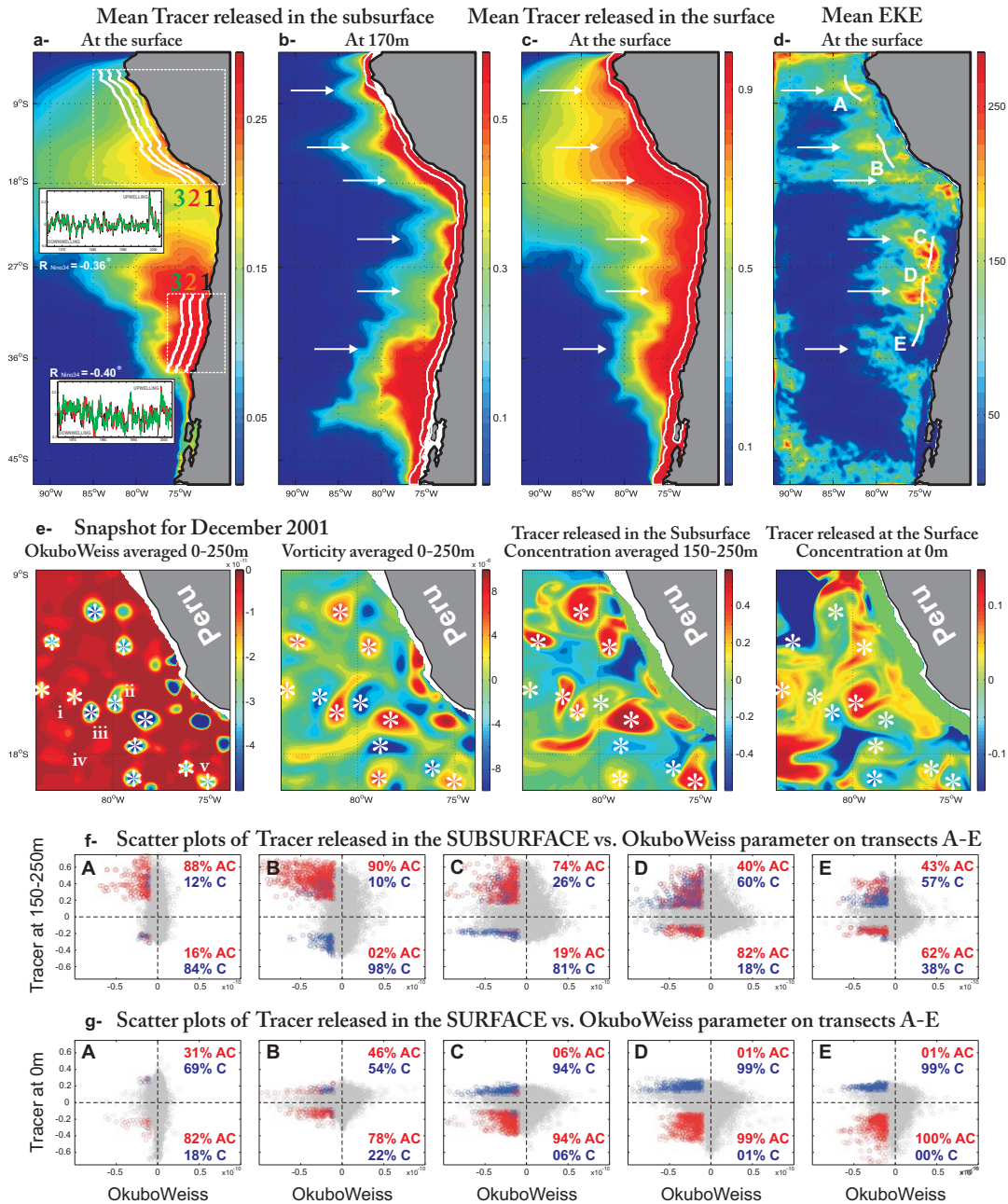
Figure 5.7: Means of (a) "subsurface tracer" at the surface, (b) "subsurface tracer" at 170m, (c) "surface tracer" at the surface and (d) Eddy Kinetic Energy (EKE in cm^{2}s^{-2}). (e) compares for December 2001, the OkuboWeiss parameter (s^{-2}) with the vorticity (s^{-1}), the "subsurface tracer" in the subsurface and the "surface tracer" at the surface. (f) scatter plots of subsurface concentration of "subsurface tracer" vs OkuboWeiss parameter on transects A-E (defined on (d)). (g) same as (f) but for the surface concentration of "surface tracer". Time series on (a) are the "subsurface tracer" concentration at the surface averaged over the transects 1 to 3, off Peru and Central Chile

5.2.5 Offshore transport statistics

For clarity, we will only analyze the output of EXP_ECMWF which has a better mean than EXP_NCEP. However EXP_NCEP show similar results (not shown here). We previously quantified how much subsurface coastal water reaches the surface off the coasts of Chile and Peru (mean field shown in figure 5.7a). However is upwelling a good indicator of how much tracer is advected to the open ocean? Time series on figure 5.7a correspond to the time series of the amount of anomalous tracer reaching the transects "1", "2" and "3", respectively located ∼100km, ∼200km and ∼300km offshore. Both off Peru and Central Chile, we find significant correlation between those different time series suggesting that the upwelled water is then advected to the cross-shore direction.

In order to look at the offshore transport of both subsurface and surface waters, we performed a similar experiment where passive tracer is now released continuously in the surface layer. We will refer to the tracer respectively released in the subsurface and at the surface as "subsurface tracer" and "surface tracer". Surface tracer is used as it removes the coastal upwelling component. Figure 5.7b shows the mean subsurface tracer concentration at the depth of 170m, whereas figure 5.7c corresponds to the mean surface tracer concentration at the surface. Figure 5.7a and 5.7b therefore correspond to the mean offshore propagation of subsurface and surface coastal waters and exhibit a similar spatial pattern. The surface advection of surface tracers is however more important compared to the subsurface advection of subsurface tracers, due to stronger surface ocean currents. Some of the offshore maximum transport seems to be located in regions of high Eddy Kinetic Energy (EKE, white arrows on figure 5.7d), suggesting that mesoscale eddies contribute to a net offshore advection.

There are plenty of evidences to suggest that mesoscale eddies play an important role in the offshore transport dynamics. Indeed, previous studies have shown than the majority of the long-lived eddies are formed near the coast in the Humboldt

Current System where the EKE is higher (Chaigneau and Pizarro, 2005; Hormazabal et al., 2004). Using satellite and drifters data Chaigneau and Pizarro (2005) derive a westward migration of ∼3 cms^{-1} south of 30°S to more than 6 cms^{-1} north of 15S. However the number of cyclonic vs anticyclonic eddies remains unclear. As pointed out by Chaigneau and Pizarro (2005), "about 2/3 of the vortices identified from drifter data are anticyclonic, whereas 2/3 of the long-lived eddies tracked from altimetry measurements are cyclonic". Another study, conducted by Correa-Ramirez et al. (2007), suggest that the same amount of cyclonic and anticyclonic eddies are responsible of the offshore advection of chlorophyll in the coastal transition zone of the HCS. In our study we use the OkuboWeiss (OW) parameter to characterize the eddy field. We define the OW by:

$$OW = \left[\frac{\partial u}{\partial x} - \frac{\partial v}{\partial y}\right]^2 + \left[\frac{\partial v}{\partial x} + \frac{\partial u}{\partial y}\right]^2 - \left[\frac{\partial v}{\partial x} - \frac{\partial u}{\partial y}\right]^2$$

where a negative Okubo-Weiss parameter corresponds to a high vorticity event. The sign of the vorticity will then allow to differentiate anticyclonic (Vorticty ≥ 0) from cyclonic (Vorticity ≤ 0) circulation. In order to obtain a smoother field of the OW, we assume that mesocale eddies conserve its circulation in the first 300m and we define the OW as the averaged OW from the surface to 300m depth. The vorticity is also averaged over the first 300m. Off Peru and for December 2001, Figure 5.7e compares the fields of the OW (only negative OW is plotted), Vorticity, subsurface tracer concentration anomaly averaged between 150 and 250m and the surface tracer concentration at the surface. The transport of coastal waters (tracer) can be understood, by looking at five different eddies labelled i, ii, iii, iv and v on figure 5.7e. (i) corresponds to a cyclonic eddy transporting subsurface waters but no surface water. In opposition, the cyclonic eddy (ii) transports surface waters rather than subsurface waters. Anticyclonic eddies, such as (iii), can also transport coastal waters (here in the subsurface). (iv), characterized by an OW≥0 (red colour),

show that filaments also contributes to the offshore advection of tracer. Finally, some surface tracer propagate between mesoscale eddies (v). The complexity of the offshore transport statistics is also found off Central Chile.

We now try to quantify only the advection of coastal waters (positive tracer concentration) by mesoscale eddies (negative OkuboWeiss) in the HCS. We choose five transect off Peru and Chile where high EKE is observed (labelled "A", "B", "C", "D" and "E" on figure 5.7d). These transects are located 300km off the coast. The scatter plots on figures 5.7f-g show the relationship between tracer concentration anomalies (both from surface tracer and subsurface tracer) and the OW parameter for each time and point along the transects. We choose OW$\leq$-10^{-11} m^{2}s^{-4} to identify strong eddy features. For OW$\leq$-10^{-11} m^{2}s^{-4} and $|Traceranomaly|$ greater than twice the standard deviation of the tracer time series (to characterize a significant concentration of tracer), figures 5.7f-g also separate anticyclonic (red circles; positive vorticity) from cyclonic (blue circles; negative vorticity) circulations. Differences arise between the surface and subsurface offshore dynamics. In particular off Chile (sections B, C and D) while the eddies that transport surface tracer are mainly cyclonic (blue circles), we observe that both cyclonic and anticyclonic seems to advect positive tracer anomalies subsurface. On the contrary, most of anticyclonic eddies (red circles) transport negative surface tracer anomalies offshore (eg. 99% of the events across transect D). Off Peru (transect B), our results suggest the anticyclonic are mainly responsible in the advection of tracer concentration anomaly.

5.2.6 North-South transport statistics

Eastern boundary current systems, such the HCS, share a subsurface poleward flow. Originated at the equator, this feature is an important mechanism to transport water to the lower latitudes in the subsurface. Some of its characteristics include a more saline and lower oxygen concentration core than the surrounding waters. To illustrate
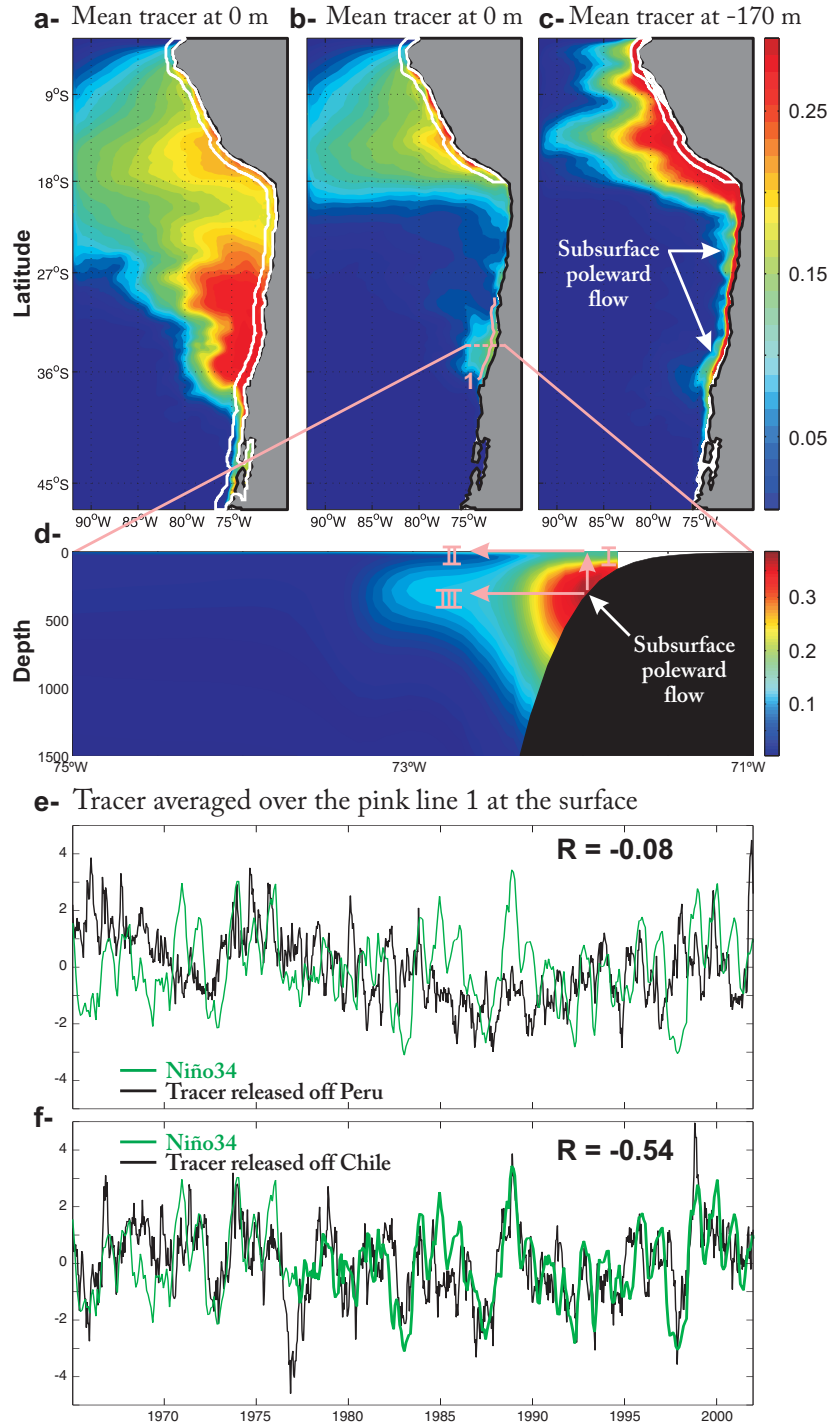
Figure 5.8: Means of (a) "subsurface tracer" at the surface, (b) "Peruvian subsurface tracer" at the surface and (c) "Peruvian subsurface tracer" at the 170m depth. White frames on (a-c) correspond to the regions where the tracers were released in the subsurface. (d) Vertical section of the "Peruvian subsurface tracer" concentration at the dashed pink line. (e) compares the "Peruvian subsurface tracer" (black line) at the surface with the Nino 3.4 index (green line). (f) same as (e) but for the "subsurface tracer"

the advection, we released the tracer in the subsurface but now only off Peru in EXP_ECMWF (white frame on figure 5.8b; named "Peruvian tracer"). On average, Peruvian tracer is found at the surface both off Peru but also off Central Chile (Figure 5.8b). Tracer concentration found at the surface off Peru is consistent with the Peruvian upwelling cell, as seen in the previous sections and in Figure 5.8a, when tracer was released all along the coast. Maximum Peruvian tracer concentration found at the surface off Central Chile, suggests that the tracer is first transported southward before being upwelled off Central Chile (as in figure 5.8a). Figure 5.8c shows the mean Peruvian tracer field at 170m deep and clearly exhibits the subsurface poleward advection. The vertical section of the Peruvian tracer at 34ºS (figure 5.8d; no tracer has been released at that latitude) also shows the strong subsurface south-north exchange (positive value), signature of the Peru-Chile UnderCurrent (PCUC). As seen in the previous sections and now on figure 5.8d, the tracer is then either upwelled ("I") and transported offshore ("II") at the surface or advected offshore in the subsurface ("III"; pink arrows on figure 5.8d).

The variability of the upwelled tracers anomalies, averaged over the pink dashed line on figure 5.8b off Central Chile, are shown on figure 5.8e for the Peruvian tracer and on figure 5.8f for the Chilean tracer (tracer analyzed in the previous sections). While the Chilean tracer at the surface is significantly modulated by ENSO (R=-0.54; as described previously), the Peruvian tracer is not anymore correlated by ENSO (R=-0.08). This implies that the amount of tracer of undercurrent water that upwells off Central Chile also depends on the amount of the undercurrent transport. The interannual variability of the PUC has also being observed by Pizzaro et al, 2002 [76].

5.2.7 Conclusion

The eastern boundary Humboldt Current System is the site of strong coastal up-welling and exceptionally high biological productivity (Ryther, 1969 [79]). In this

study, the upwelling variability has been investigated using a free-surface, hydrostatic, eddy-resolving primitive equation model forced with two different sets of surface momentum fluxes (ECMWF and NCEP). The statistics of the upwelled coastal waters were computed using a model passive tracer. Consistent with satellite observations and previous descriptions of the circulation in the HCS region, we find that the mean SSH and SST are well reproduced in EXP_ECMWF. The presence of the passive tracer shows the coast of Peru and central Chile as two intense (and consequently highly productive) upwelling regions. We also find that even though EXP_NCEP does not clearly capture the upwelling cells in the mean SST and shows significant differences in the mean SSH, due to a poor representation of the mean coastal NCEP winds, the non-seasonal temporal variability shows a good agreement with coastal in-situ measurements.

On the interannual time scale, much of the variability is caused by the ENSO cycle both through local changes in the surface wind stress and via the propagation of coastally trapped Kelvin waves, generated at the equator. Indeed, off Peru, an EOF analysis on the passive tracer at the surface shows that the first mode of variability is significantly correlated with the Nino 3.4 index. Off central Chile the first mode also reveals the ENSO variability.

The studies from Brink (1982) [12], focused on the Peru region, and Leth and Middleton (2006) [53], focused on Central Chile, show that the coastal trapped waves have an important contribution to the upwelling variability in those regions, which often dominate the effect of local winds, especially off Peru. The passive tracer approach used in our study also supports that view. We find that the correlation between the interannual upwelling variability and ENSO drops considerably when the model boundaries do not transmit the equatorial Kelvin waves. In particular off Peru, when the first mode of upwelling variability is strongly correlated with the Nino 3.4 index in presence of equatorial coastally trapped Kelvin waves, they become

uncorrelated without. Those differences in upwelling strength are clearly seen during strong El Nino events (1982, 1997), both off Peru and central Chile.

Our study also focused on the offshore transport of the coastal nutrient-rich waters. Results show that while the surface offshore transport of upwelled water is correlated with the ENSO cycle, the net offshore propagation of coastal waters is a complex combination of mesoscale eddies and filaments, both at the surface and in the subsurface. Off Chile, cyclonic eddies seems to dominate the offshore advection of surface tracer (compared to anticyclonic eddies). Nevertheless, both anticyclonic and cyclonic mesoscale eddies contribute to the subsurface offshore transport of subsurface tracer. This study had also emphasized the south-north transport by the poleward undercurrent (PCUC). Our results provide evidences that the central Chile upwelling cell is enriched by the subsurface coastal waters originated in the Peruvian coast and transported in the core of the PCUC.

The passive tracer experiments, performed in this study, provide a dynamical framework to interpret (and predict) how the upwelling of nutrient-rich coastal water has (and will) respond to atmospheric and oceanic forcing and therefore also allows predictions of changes in vertical and offshore advection of other important biochemical quantities. This variability could have strong impacts in the Peru-Chile upwelling ecosystem. Earlier studies have shown that the ENSO interannual variability strongly modulates the biological productivity, species distribution and community structure in the coastal pelagic ecosystem (Ulloa et al., 2001 [100]; Escribano et al., 2004 [32]; Bertrand et al., 2008 [7]). However, the underlying mechanism associated to this variability remains poorly described. In this context, the use of ocean modeling became an important tool to understand the forces driving the fluctuations in the Humboldt ecosystem.

5.3 Biophysical modeling of mackerel in the southeastern Pacific and its impact on the chilean fishing resources

This 3-years project is currently conducted by El Insitituto de Investigación Pesquera Octava Región S.A. (INPESCA), based in Concepción, Chile. INPESCA is a chilean private company, focused on marine scientific research, with an emphasis on the analysis of pelagic and benthic fisheries and also on monitoring of fisheries and stock assessment. The goal of that particular study is to implement a modeling approach, coupling 3D hydrodynamic models with biological models, to understand the spatial and temporal dynamics of the mackerel community in the southeast Pacific. The expected results include:

- A validation of the physical-biological model for the resource of the mackerel in the Eastern Pacific.

- A better understanding of the spatial and temporal dynamics of the concentration of mackerels associated with mesoscale eddies.

- An evaluation of the connectivity between the open ocean and nursing coastal regions, as well as the dynamics of the young fishes in the nursing regions.

- An improvement of the forecast of more productive fishing areas which will help the decision-making of the fishing industries.

ROMS will first be used as the physical model to reproduce the dynamics of the HCS on a 10km spatial resolution grid from 2000 to 2007. The grid extends from the coast to -130°W and from 5°N to 50°S (labeled PCCS_WEST on figure 2.1). An experiment has already beeing performed forced by daily QSCAT wind stress, climatology heat and fresh water fluxes from NCEP/NCAR reanalysis and monthly OFES boundary conditions.

Figure 5.9 a-d show a comparison between the means ROMS model (left column) output with the WOA data (right column), for both the sea surface temperature and sea surface salinity for the new domain. The model SST field clearly shows the

surface signature of the Peruvian and Central Chile upwelling cells, as seen in section
. In addition to the coastal upwellings, a strong opean ocean upwelling is present
along the equator. This equatorial upwelling is associated with the the Intertropical
Convergence Zone and with the convergence of the trade winds from the northern and
southern hemisphere. Easterly winds blowing along the ITCZ, in both the Pacific and
Atlantic Basins, tend to drive the water away from the equator due to the coriolis
effect. This phenomenon therefore results in a divergence, with denser, nutrient-rich
water being upwelled from below. Figure 5.9 e-f show the vertical profiles of the mean
SSS along the white dashed line. The presence of the high salinity around 200m at
the coast (signature of the poleward Peru-Chile undercurrent) is an important feature
of the salinity field. When σ-coordinated ocean models tended to mix in the vertical,
the scheme of temperature and salinity vertical mixings described by Marchesiello et
al, 2009 [59] therefore seems to be able to maintain a tongue of higher salinity in the
vertical. The location and the scale of the salinity, associated with the poleward flow,
are comparable with the WOA data. Figure 5.9e also exhibits an offshore extension
of that specific high salinity. As seen previously, some of the high salinity originated
at the poleward flow is trapped inside the core of mesoscale eddies and transported
offshore.

The biological model consists of a stochastic individual-based model (IBM) currently adapted to this specific region by Dr Carolina Parada (based in Concepción, Chile).
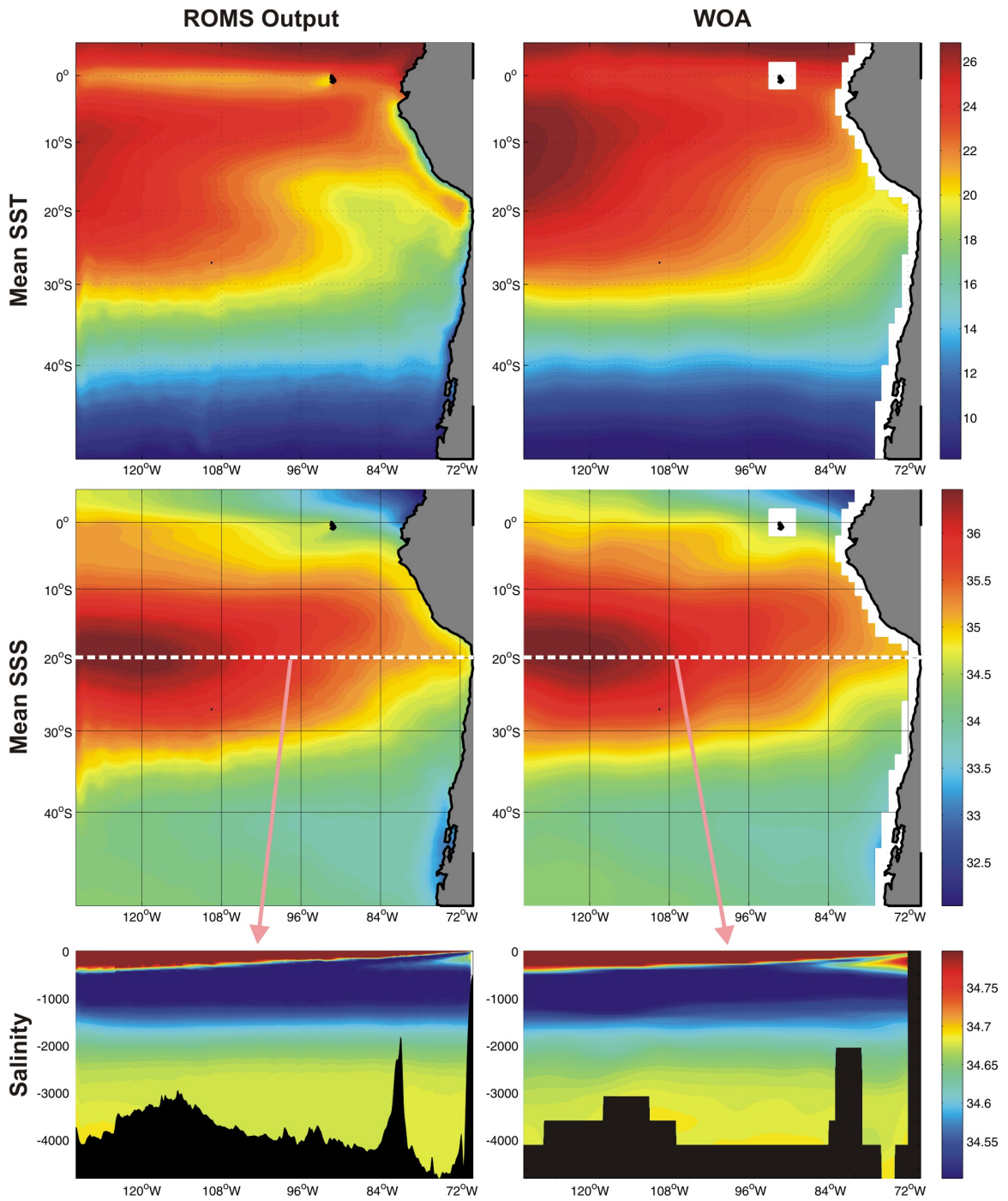
Figure 5.9: Means of the ROMS modeled sea surface temperature (a; SST) and sea surface salinity (c; SSS). (e) shows the vertical profile of the mean SSS along the white dashed line. (b), (d), (f) same as (a), (c), (e) but from the WOA

CHAPTER VI

CONCLUSION

Early comparisons of eastern boundary coastal upwelling systems can be found in Sverdrup et al., 1942 ([96]). Sverdrup et al., 1942 ([96]) had already noticed the strong coupling between atmospheric forcings and coastal ocean circulation: "The temperature close to the coast (of Northwest Africa) is also lowered by upwelling from moderate depths due to the action of prevailing northwesterly winds, but this upwelling does not exercise influence as widespread as does corresponding upwelling off the coasts of southwest Africa or, particularly, as does that off the west coasts of North and South America." The upwelling, which brings cold but also deep nutrient-rich waters and full of dissolved organics matter, results in high levels of primary productivity and fishery production. This dissertation focuses on the two eastern boundary currents of the Pacific: the California Current System (CCS) and the Peru-Chile Current System (HCS). The ROMS ocean model (chapter 2) has been chosen to investigate the dynamics of those regions. The experiments, exposed in the dissertation, have in common a passive tracer approach to characterize the dispertion of coastal waters in the CCS and HCS.

A detailed discussion and summary of the results have been provided in each chapter. Off the coast of California, we find that the low-frequency upwelling and the surface offshore transport of the upwelled nutrient-rich coastal water are strongly correlated with the NPGO index, and is coherent between the central and southern CCS. The offshore transport of the surface coastal water is nevertheless not coherent between those two regions, and has been found to be associated with mesoscale eddy activity, where both surface and subsurface waters propagate offshore mainly through

cyclonic eddies. Our results also show that the poleward California Under Current, at about 200m depth, affects the alongshore transport and provides rich waters to the Central California upwelling system.

For the HCS, both changes in surface wind and coastally trapped Kelvin waves control the variability of the coastal upwelling. The effect of ocean remote forcing is assessed by comparing the output of two model simulations which selectively include or exclude the effects of coastally trapped waves at the model open boundaries. The passive tracer approach indicates that, off the coast of Peru, the El Nino Southern Oscillation (ENSO) strongly modulates the strength of coastal upwelling principally due to the propagation of downwelling equatorial Kelvin waves rather than changes in the local wind stress. Our results indicate that the central Chile upwelling region is also very sensitive to Kelvin waves generated at the equator, and is considerably reduced during strong El Nino events. Different model experiments have also been conducted to explore the sensitivity of the HCS upwelling to air-sea fluxes of momentum (ECMWF vs NCEP surface wind stress forcings). Similar to the CCS region, we find that mesoscale eddies play an important role in the offshore advection of nutrient-rich coastal waters.

In opposition to the upwelling conditions off the coast of Central Chile, Peru and California, the coast of the Gulf of Alaska is mainly associated with downwelling conditions. The marine ecosystem of the Gulf of Alaska is very rich despite an open ocean characterized by high nutrient and low-chlorophyll-a (HNLC) concentration with iron limitation. Recent observational studies suggest that advection of iron-rich coastal water to the HNLC open ocean is the primary mechanism controlling open ocean productivity and play an important role in maintaining a high chlorophyll concentration. On average along the Alaska Current, we find that at the surface while the advection of tracers by the average flow is directed towards the coast consistent with the dominant downwelling regime of the GOA, it is the mean eddy fluxes that

contribute to offshore advection into the gyre interior. South of the Alaskan Peninsula, both the advection of tracers (coastal water masses) by the average flow and the mean eddy fluxes contribute to the mean offshore advection. On interannual and longer timescales, the offshore transport of the passive tracer in the Alaskan Stream does not correlate with large scale atmospheric forcing, nor with local winds (intrinsic vairiability). In contrast in the Alaska Current region (forced variability), stronger offshore transport of the passive tracer coincides with periods of stronger downwelling (in particular during positive phases of the Pacific Decadal Oscillation), which trigger the development of stronger eddies.

This dissertation has been conducted under the Pacific Ocean Boundary Ecosystem and Climate Study (POBEX; www.pobex.org), which investigates the mechanisms of climate-related variability in the Pacific boundary ecosystems (GOA, CCS, PCCS and also the Kuroshio-Oyashio Extension region). The results from this thesis, along with the model passive tracers data archive, provide the basis to quantify the relationship between ocean transport statistics and ecosystem variations in the eastern boundary regions, a central focus of POBEX. The regional model simulations that result from this dissertation will be combined with existing historical time series of phytoplankton and zooplankton to determine if changes in regional processes (e.g. coastal upwelling, mesoscale eddies transport) exert a direct control (bottom-up forcing) on the lower trophic ecosystems of the Pacific boundary current systems. There is growing evidence suggesting that horizontal transport variability, together with upwelling, is important in understanding the long-term lower trophic ecosystem dynamics (e.g. zooplankton and fish). Given the limited amount of long term observations of ocean horizontal transport, this dissertation provides for the first time a coherent assessment along the entire eastern boundary of how large-scale climate forcing and regional dynamics impact the ocean advection statistics. However, the limited amount of observations also limits our ability to assess the degree of realism

and uncertainties of the ocean model simulations.

Future numerical studies in the GOA, CCS and PCCS systems, will require an improvement of several components of the ocean modeling framework. These include a river input module that was not included in the ROMS simulations presented in the dissertation. The large amount of freshwater provided by rivers such as the Columbian river (Washington State, USA) or the Bio-bio river (Central Chile) should have a significant impact on the stratification and baroclinic structure of the coastal velocity field in these regions. Along the coast of Alaska, the presence of the rivers in the ROMS experiments should also play an important role in the change of coastal ocean dynamics in a global warming scenario, in which the melting of numerous glaciers of Alaska will provide a significant amount of fresh water at the coast. The representation of the coastally trapped Kelvin waves, which primarily control the coastal upwelling variability off Peru (Chapter 5), also need some improvement in the model configuration. Our experiments use monthly average boundary forcing to simulate the presence of the coastally trapped waves, generated at the equator and propagating through the northern boundary. Knowing that those waves dominate the intraseasonal band (30 to 70 days), a higher frequency boundary forcing would clearly give more realistic results. Using monthly average forcings (e.g. open and surface boundary conditions) may also limit the degree of realism of the low frequency regional ocean circulations. The experiments have been designed under the assumption that high frequency forcing does not substantially change the low frequency character of the ocean response. However high frequency winds and heat fluxes have a direct impact on the structure of the ocean mixed layer and hence of the mean density structure, which in turn can affect the statistics of instabilities (e.g. mesoscale eddies) as well as the structure of the upwelling cell response to low frequency climate forcing. The uncertainties deriving from these configuration issues need to be carefully considered and evaluated in future modeling work.

REFERENCES

[1] A., H. S. and Thomas, A. C., "A census of oceanic anticyclonic eddies in the gulf of alaska," *Deep Sea Research Part I: Oceanographic Research Papers*, vol. 55, no. 2, pp. 163–176, —2008—.

[2] Alheit, J. and Niquen, M., "Regime shifts in the humboldt current ecosystem," *Progress in Oceanography*, vol. 60, no. 2-4, pp. 201–222, —2004—.

[3] Arcos, D. F., Cubillos, L. A., and Nunez, S. P., "The jack mackerel fishery and el nino 1997-98 effects off chile," *Progress in Oceanography*, vol. 49, no. 1-4, pp. 597–617, —2001—.

[4] Barber, R. T. and Smith, R. L., "Coastal upwelling ecosystems," *Analysis of Marine Ecosystems, edited by A. R. Longhurst, Academic Press, San Diego, Calif., 31-68*, —1981—.

[5] Batten, S. D. and Crawford, W. R., "The influence of coastal origin eddies on oceanic plankton distributions in the eastern gulf of alaska," *Deep-Sea Research Part Ii-Topical Studies In Oceanography*, vol. 52, no. 7-8, pp. 991–1009, —2005—.

[6] Bernal, P., "Low-frequency response of california california current pelagic ecosystem," *Calif. Coop. Oceanic Fish. Invest. Rep*, vol. 22, —1981—.

[7] Bertrand, S., Dewitte, B., Tam, J., Diaz, E., and Bertrand, A., "Impacts of kelvin wave forcing in the peru humboldt current system: Scenarios of spatial reorganizations from physics to fishers," *Progress in Oceanography*, vol. 79, no. 2-4, pp. 278–289, —2008—.

[8] Bograd, S. J. and Lynn, R. J., "Physical-biological coupling in the california current during the 1997-99 el nino-la nina cycle," *Geophysical Research Letters*, vol. 28, no. 2, pp. 275–278, —2001—.

[9] Bond, N. A., Overland, J. E., Spillane, M., and Stabeno, P., "Recent shifts in the state of the north pacific," *Geophysical Research Letters*, vol. 30, no. 23, p. 4, —2003—.

[10] Boyd, P. W., Law, C. S., Wong, C. S., and et al., "The decline and fate of an iron-induced subarctic phytoplankton bloom," *Nature*, vol. 428, pp. 549–553, —2004—.

[11] Brickley, P. J. and Thomas, A. C., "Satellite-measured seasonal and inter-annual chlorophyll variability in the northeast pacific and coastal gulf of alaska,"

Deep-Sea Research Part Ii-Topical Studies in Oceanography, vol. 51, no. 1-3, pp. 229–245, —2004—.

[12] BRINK, K. H., "A comparison of long coastal trapped wave theory with observations off peru," *Journal of Physical Oceanography*, vol. 12, no. 8, pp. 897–913, —1982—.

[13] CAPOTONDI, A., ALEXANDER, M. A., DESER, C., and MILLER, A. J., "Low-frequency pycnocline variability in the northeast pacific," *Journal Of Physical Oceanography*, vol. 35, no. 8, pp. 1403–1420, —2005—.

[14] CARTON, J. A., CHEPURIN, G., CAO, X. H., and GIESE, B., "A simple ocean data assimilation analysis of the global upper ocean 1950-95. part i: Methodology," *Journal of Physical Oceanography*, vol. 30, no. 2, pp. 294–309, —2000—.

[15] CHAIGNEAU, A. and PIZARRO, O., "Eddy characteristics in the eastern south pacific," *Journal of Geophysical Research-Oceans*, vol. 110, no. C6, —2005—.

[16] CHAVEZ, F. P. and MESSIE, M., "A comparison of eastern boundary upwelling ecosystems," *Progress in Oceanography*, vol. 83, no. 1-4, pp. 80–96, —2009—.

[17] CHAVEZ, F. P., RYAN, J., LLUCH-COTA, S. E., and NIQUEN, M., "From anchovies to sardines and back: Multidecadal change in the pacific ocean," *Science*, vol. 299, no. 5604, pp. 217–221, —2003—.

[18] CHELTON, D. B. and SCHLAX, M. G., "Global observations of oceanic rossby waves," *Science*, vol. 272, no. 5259, pp. 234–238, —1996—.

[19] COLLINS, W. D., BITZ, C. M., BLACKMON, M. L., BONAN, G. B., BRETHERTON, C. S., CARTON, J. A., CHANG, P., DONEY, S. C., HACK, J. J., HENDERSON, T. B., KIEHL, J. T., LARGE, W. G., MCKENNA, D. S., SANTER, B. D., and SMITH, R. D., "The community climate system model version 3 (ccsm3)," *Journal Of Climate*, vol. 19, no. 11, pp. 2122–2143, —2006—.

[20] COMBES, V. and DI LORENZO, E., "Intrinsic and forced interannual variability of the gulf of alaska mesoscale circulation," *Progress in Oceanography*, vol. 75, no. 2, pp. 266–286, —2007—.

[21] COMBES, V., DI LORENZO, E., and CURCHITSER, E., "Interannual and decadal variations in cross-shelf transport in the gulf of alaska," *Journal of Physical Oceanography*, vol. 39, no. 4, pp. 1050–1059, —2009—.

[22] CORREA-RAMIREZ, M. A., HORMAZABAL, S., and YURAS, G., "Mesoscale eddies and high chlorophyll concentrations off central chile (29 degrees-39 degrees s)," *Geophysical Research Letters*, vol. 34, no. 12, p. 5, —2007—.

[23] CRAWFORD, W. R., "Physical characteristics of haida eddies," *Journal of Oceanography*, vol. 58, no. 5, pp. 703–713, —2002—.

[24] CRAWFORD, W. R., "Heat and fresh water transport by eddies into the gulf of alaska," *Deep-Sea Research Part Ii-Topical Studies In Oceanography*, vol. 52, no. 7-8, pp. 893–908, —2005—.

[25] CRAWFORD, W. R., BRICKLEY, P. J., PETERSON, T. D., and THOMAS, A. C., "Impact of haida eddies on chlorophyll distribution in the eastern gulf of alaska," *Deep-Sea Research Part Ii-Topical Studies In Oceanography*, vol. 52, no. 7-8, pp. 975–989, —2005—.

[26] CRAWFORD, W. R., CHERNIAWSKY, J. Y., and FOREMAN, M. G. G., "Multi-year meanders and eddies in the alaskan stream as observed by topex/poseidon altimeter," *Geophysical Research Letters*, vol. 27, no. 7, pp. 1025–1028, —2000—.

[27] CUMMINS, P. F. and LAGERLOEF, G. S. E., "Wind-driven interannual variability over the northeast pacific ocean," *Deep-Sea Research Part I-Oceanographic Research Papers*, vol. 51, no. 12, pp. 2105–2121, —2004—.

[28] DI LORENZO, E., FOREMAN, M. G. G., and CRAWFORD, W. R., "Modelling the generation of haida eddies," *Deep-Sea Research Part Ii-Topical Studies In Oceanography*, vol. 52, no. 7-8, pp. 853–873, —2005—.

[29] DI LORENZO, E., MILLER, A. J., SCHNEIDER, N., and MCWILLIAMS, J. C., "The warming of the california current system: Dynamics and ecosystem implications," *Journal Of Physical Oceanography*, vol. 35, no. 3, pp. 336–362, —2005—.

[30] DI LORENZO, E., SCHNEIDER, N., COBB, K. M., FRANKS, P. J. S., CHHAK, K., MILLER, A. J., MCWILLIAMS, J. C., BOGRAD, S. J., ARANGO, H., CURCHITSER, E., POWELL, T. M., and RIVIERE, P., "North pacific gyre oscillation links ocean climate and ecosystem change," *Geophysical Research Letters*, vol. 35, no. 8, p. 6, —2008—.

[31] ENFIELD, D. B., "The intraseasonal oscillation in eastern pacific sea levels - how is it forced," *Journal of Physical Oceanography*, vol. 17, no. 11, pp. 1860–1876, —1987—.

[32] ESCRIBANO, R., DANERI, G., FARIAS, L., GALLARDO, V. A., GONZALEZ, H. E., GUTIERREZ, D., LANGE, C. B., MORALES, C. E., PIZARRO, O., ULLOA, O., and BRAUN, M., "Biological and chemical consequences of the 1997-1998 el nino in the chilean coastal upwelling system: a synthesis," *Deep-Sea Research Part Ii-Topical Studies in Oceanography*, vol. 51, no. 20-21, pp. 2389–2411, —2004—.

[33] FAIRALL, C. W., BRADLEY, E. F., HARE, J. E., GRACHEV, A. A., and EDSON, J. B., "Bulk parameterization of air-sea fluxes: updates and verification for the coare algorithm," *Journal of Climate*, vol. 16, pp. 571–591, —2003—.

[34] Gower, J. F. R. and Tabata, S., "Measurement of eddy motion in the north-east pacific using the geosat altimeter," *In Satellite Remote Sensing of the Oceanic Environment, ed. by I. S. F. Jones, Y. Sugimori and R. W. Stewart, Seibutsu Kenkyusha, Tokyo*, p. 375382, —1993—.

[35] Gunther, E. R., "A report on oceanographical investigation in the peru coastal current," *Discovery Rep.*, vol. 13, pp. 107–276, —1936—.

[36] Haidvogel, D. B., Arango, H. G., Hedstrom, K., Beckmann, A., Malanotte-Rizzoli, P., and Shchepetkin, A. F., "Model evaluation experiments in the north atlantic basin: simulations in nonlinear terrain-following coordinates," *Dynamics Of Atmospheres And Oceans*, vol. 32, no. 3-4, pp. 239–281, —2000—.

[37] Halpern, D., "Offshore ekman transport and ekman pumping off peru during the 1997-1998 el nino," *Geophysical Research Letters*, vol. 29, no. 5, p. 4, —2002—.

[38] Harrison, P. J., Boyd, P. W., Varela, D. E., and Takeda, S., "Comparison of factors controlling phytoplankton productivity in the ne and nw subarctic pacific gyres," *Progress In Oceanography*, vol. 43, no. 2-4, pp. 205–234, —1999—.

[39] Hickey, B., "The california current system - hypotheses and facts," *Progress in Oceanography*, vol. 8, pp. 191–279, —1979—.

[40] Hickey, B., "Coastal oceanography of western north america from the tip of baja california to vancouver island," *In The Sea (A.R. Robinson, A.R. and K.H. Brink eds.). New York: Wiley and Sons, 11 345-393*, —1998—.

[41] Hill, A. E., Hickey, B. M., Shillington, F. A., Strub, P. T., Brink, K. H., Barton, E. D., and Thomas, A. C., "Eastern ocean boundaries," *The Sea, vol. 11, edited by A. R. Robinson and K. H. Brink, pp. 29- 67, John Wiley, Hoboken, N. J.*, —1999—.

[42] Hormazabal, S., Shaffer, G., and Pizarro, O., "Tropical pacific control of intraseasonal oscillations off chile by way of oceanic and atmospheric pathways," *Geophysical Research Letters*, vol. 29, no. 6, —2002—.

[43] Johnson, W. K., Miller, L. A., Sutherland, N. E., and Wong, C. S., "Iron transport by mesoscale haida eddies in the gulf of alaska," *Deep-Sea Research Part Ii-Topical Studies In Oceanography*, vol. 52, no. 7-8, pp. 933–953, —2005—.

[44] Kalnay, E., Kanamitsu, M., Kistler, R., Collins, W., Deaven, D., Gandin, L., Iredell, M., Saha, S., White, G., Woollen, J., Zhu, Y., Chelliah, M., Ebisuzaki, W., Higgins, W., Janowiak, J., Mo, K. C., Ropelewski, C., Wang, J., Leetmaa, A., Reynolds, R., Jenne, R.,

and Joseph, D., "The ncep/ncar 40-year reanalysis project," *Bulletin Of The American Meteorological Society*, vol. 77, no. 3, pp. 437–471, —1996—.

[45] LaCasce, J. H. and Pedlosky, J., "The instability of rossby basin modes and the oceanic eddy field," *Journal Of Physical Oceanography*, vol. 34, no. 9, pp. 2027–2041, —2004—.

[46] Ladd, C., "Interannual variability of the gulf of alaska eddy field," *Geophysical Research Letters*, vol. 34, —2007—.

[47] Ladd, C., Kachel, N. B., Mordy, C. W., and Stabeno, P. J., "Observations from a yakutat eddy in the northern gulf of alaska," *Journal of Geophysical Research-Oceans*, vol. 110, no. C3, —2005—.

[48] Ladd, C., Stabeno, P., and Cokelet, E. D., "A note on cross-shelf exchange in the northern gulf of alaska," *Deep-Sea Research Part Ii-Topical Studies In Oceanography*, vol. 52, no. 5-6, pp. 667–679, —2005—.

[49] Lagerloef, G. S. E., "Interdecadal variations in the alaska gyre," *Journal of Physical Oceanography*, vol. 25, no. 10, pp. 2242–2258, —1995—.

[50] Large, W. and Yeager, S., "Diurnal to decadal global forcing for ocean and sea-ice models: the data sets and flux climatologies. ncar technical note: Ncar/tn-460+str.," *CGD Division of the National Center for Atmospheric Research*, —2004—.

[51] Large, W. G., McWilliams, J. C., and Doney, S. C., "Oceanic vertical mixing: A review and a model with a nonlocal boundary layer parameterization," *Rev. Geophys.*, vol. 32, no. 4, pp. 363–403, —1994—.

[52] Lavaniegos, B. E. and Ohman, M. D., "Long-term changes in pelagic tunicates of the california current," *Deep-Sea Research Part Ii-Topical Studies in Oceanography*, vol. 50, no. 14-16, pp. 2473–2498, —2003—.

[53] Leth, O. and Middleton, J. F., "A numerical study of the upwelling circulation off central chile: Effects of remote oceanic forcing," *Journal of Geophysical Research-Oceans*, vol. 111, no. C12, —2006—.

[54] Levitus, S., Burgett, R., and Boyer, T., "World ocean atlas 1994," *World Ocean Atlas 1994. NOAA Atlas NESDIS 4, US Government Printing Office, Washington, DC, pp. 3-4.*, —1994—.

[55] Litzow, M. A., Bailey, K. M., Prahl, F. G., and Heintz, R., "Climate regime shifts and reorganization of fish communities: the essential fatty acid limitation hypothesis," *Marine Ecology-Progress Series*, vol. 315, pp. 1–11, —2006—.

[56] LVY, M., KLEIN, P., and TREGUIER, A. M., "Impacts of sub-mesoscale physics on phytoplankton production and subduction," *J. Mar. Res.*, vol. 59, pp. 535–565, —2001—.

[57] MACKAS, D. L. and GALBRAITH, M. D., "Zooplankton distribution and dynamics in a north pacific eddy of coastal origin: 1. transport and loss of continental margin species," *Journal Of Oceanography*, vol. 58, no. 5, pp. 725–738, —2002—.

[58] MANTUA, N. J., HARE, S. R., ZHANG, Y., WALLACE, J. M., and FRANCIS, R. C., "A pacific interdecadal climate oscillation with impacts on salmon production," *Bulletin Of The American Meteorological Society*, vol. 78, no. 6, pp. 1069–1079, —1997—.

[59] MARCHESIELLO, P., DEBREU, L., and COUVELARD, X., "Spurious diapycnal mixing in terrain-following coordinate models: The problem and a solution," *Ocean Modelling*, vol. 26, pp. 156–169, —2009—.

[60] MARCHESIELLO, P., MCWILLIAMS, J. C., and SHCHEPETKIN, A., "Open boundary conditions for long-term integration of regional oceanic," *Ocean Modelling*, vol. 3, pp. 1–20, —2001—.

[61] MARCHESIELLO, P., MCWILLIAMS, J. C., and SHCHEPETKIN, A., "Equilibrium structure and dynamics of the california current system," *Journal of Physical Oceanography*, vol. 33, no. 4, pp. 753–783, —2003—.

[62] MASUMOTO, Y., SASAKI, H., KAGIMOTO, T., KOMORI, N., ISHIDA, A., SASAI, Y., MIYAMA, T., MOTOI, T., MITSUDERA, H., TAKAHASHI, K., SAKUMA, H., and YAMAGATA, T., "A fifty-year eddy-resolving simulation of the world ocean preliminary outcomes of ofes (ogcm for the earth simulator)," *Journal of the Earth Simulator,*, vol. 1, pp. 35–36, —2004—.

[63] MCGOWAN, J., BOGRAD, S., LYNN, R., and MILLER, A., "he biological response to the 1977 regime shift in the california current," *Deep Sea Research Part II-Topical Studies in Oceanography*, vol. 50, pp. 2567–2582, —2003—.

[64] MCGOWAN, J. A., CHELTON, D. B., and CONVERSI, A., "Plankton patterns, climate, and change in the california current," *California Cooperative Oceanic Fisheries Investigations Reports*, vol. 37, pp. 45–68, —1996—.

[65] MELLOR, G. L., EZER, T., and OEY, L. Y., "The pressure-gradient conundrum of sigma coordinate ocean models," *Journal Of Atmospheric And Oceanic Technology*, vol. 11, no. 4, pp. 1126–1134, —1994—.

[66] MELSOM, A., MEYERS, S., HURLBURT, H., METZGER, E., and O'BRIEN, J., "Enso effects on gulf of alaska eddies," *Earth Interactions 3 (1), (available at http://earthinteractions.org/)*, —1999—.

[67] MEYERS, S. D. and BASU, S., "Eddies in the eastern gulf of alaska from topex poseidon altimetry," *Journal Of Geophysical Research-Oceans*, vol. 104, no. C6, pp. 13333–13343, —1999—.

[68] MILLER, A. J., CAYAN, D., T., B., N., G., and J., O., "The 1976-77 climate shift of the pacific ocean," *Oceanography*, vol. 7, no. 1, —1994—.

[69] MILLER, A. J., DI LORENZO, E., NEILSON, D. J., KIM, H. J., CAPOTONDI, A., ALEXANDER, M. A., BOGRAD, S. J., SCHWING, F. B., MENDELSSOHN, R., HEDSTROM, K., and MUSGRAVE, D. L., "Interdecadal changes in mesoscale eddy variance in the gulf of alaska circulation: Possible implications for the steller sea lion ecline," *Atmosphere-Ocean*, vol. 43, no. 3, pp. 231–240, —2005—.

[70] MURRAY, C. P., MOREY, S. L., and O'BRIEN, J. J., "Interannual variability of upper ocean vorticity balances in the gulf of alaska," *Journal Of Geophysical Research-Oceans*, vol. 106, no. C3, pp. 4479–4491, —2001—.

[71] NIILER, P. P., MAXIMENKO, N. A., and MCWILLIAMS, J. C., "Dynamically balanced absolute sea level of the global ocean derived from near-surface velocity observations," *Geophys. Res. Lett.*, vol. 30, no. 22, —2003—.

[72] OKKONEN, S. R., JACOBS, G. A., METZGER, E. J., HURLBURT, H. E., and SHRIVER, J. F., "Mesoscale variability in the boundary currents of the alaska gyre," *Continental Shelf Research*, vol. 21, no. 11-12, pp. 1219–1236, —2001—.

[73] OKKONEN, S. R., WEINGARTNER, T. J., DANIELSON, S. L., MUSGRAVE, D. L., and SCHMIDT, G. M., "Satellite and hydrographic observations of eddy-induced shelf-slope exchange in the northwestern gulf of alaska," *Journal of Geophysical Research-Oceans*, vol. 108, no. C2, —2003—.

[74] PENVEN, P., ECHEVIN, V., PASAPERA, J., COLAS, F., and TAM, J., "Average circulation, seasonal cycle, and mesoscale dynamics of the peru current system: A modeling approach," *Journal of Geophysical Research-Oceans*, vol. 110, no. C10, —2005—.

[75] PENVEN, P., ROY, C., BRUNDRIT, G. B., DE VERDIERE, A. C., FREON, P., JOHNSON, A. S., LUTJEHARMS, J. R. E., and SHILLINGTON, F. A., "A regional hydrodynamic model of upwelling in the southern benguela," *South African Journal of Science*, vol. 97, no. 11-12, pp. 472–475, —2001—.

[76] PIZARRO, O., SHAFFER, G., DEWITTE, B., and RAMOS, M., "Dynamics of seasonal and interannual variability of the peru-chile undercurrent," *Geophysical Research Letters*, vol. 29, no. 12, —2002—.

[77] PLATTNER, G., GRUBER, N., FRENZEL, H., and MCWILLIAMS, J. C., "Decoupling marine export production from new production," *Geophysical Research Letters*, vol. 32, no. 11, —2005—.

[78] ROEMMICH, D. and MCGOWAN, J., "Climatic warming and the decline of zooplankton in the california current (vol 267, pg 1324, 1995)," *Science*, vol. 268, no. 5209, pp. 352–353, —1995—.

[79] RYTHER, J. H., "Photosynthesis and fish production in sea," *Science*, vol. 166, no. 3901, pp. 72–76, —1969—.

[80] SANDWELL, D. T. and SMITH, W. H. F., "Marine gravity anomaly from geosat and ers 1 satellite altimetry," *Journal Of Geophysical Research-Solid Earth*, vol. 102, no. B5, pp. 10039–10054, —1997—.

[81] SASAI, Y., ISHIDA, A., SASAKI, H., KAWAHARA, S., UEHARA, H., and YAMANAKA, Y., "A global eddy-resolving coupled physical-biological model: Physical influences on a marine ecosystem in the north pacific," *Simulation-Transactions of the Society for Modeling and Simulation International*, vol. 82, no. 7, pp. 467–474, —2006—.

[82] SASAKI, H., NONAKA, M., MASUMOTO, Y., SASAI, Y., UEHARA, H., and SAKUMA, H., "An eddy-resolving hindcast simulation of the quasi-global ocean from 1950 to 2003 on the earth simulator," *High resolution numerical modelling of the atmosphere and ocean, edited by W. Ohfuchi and K. Hamilton, Springer, New York, accepted*, —2006—.

[83] SASAKI, H., SASAI, Y., KAWAHARA, S., FURUICHI, M., ARAKI, F., ISHIDA, A., YAMANAKA, Y., MASUMOTO, Y., and SAKUMA, H., "A series of eddy -resolving ocean simulations in the world ocean: Ofes (ogcm for the earth simulator)," *project, OCEAN'04, 3*, pp. 1535 –1541, —2004—.

[84] SHAFFER, G., PIZARRO, O., DJURFELDT, L., SALINAS, S., and RUTLLANT, J., "Circulation and low-frequency variability near the chilean coast: Remotely forced fluctuations during the 1991-92 el nino," *Journal of Physical Oceanography*, vol. 27, no. 2, pp. 217–235, —1997—.

[85] SHCHEPETKIN, A. F. and MCWILLIAMS, J. C., "Quasi-monotone advection schemes based on explicit locally adaptive dissipation," *Monthly Weather Review*, vol. 126, no. 6, pp. 1541–1580, —1998—.

[86] SHCHEPETKIN, A. F. and MCWILLIAMS, J. C., "The regional oceanic modeling system (roms): a split-explicit, free-surface, topography-following-coordinate oceanic model," *Ocean Modelling*, vol. 9, no. 4, pp. 347–404, —2005—.

[87] SMITH, R. D. and GENT, P. R., "Reference manual for the parallel ocean program (pop), ocean component of the community climate system model (ccsm2.0 and 3.0)," *Tech. Rep. LA-UR-02-2484, Los Alamos National Laboratory*, vol. Available online at http://www.ccsm.ucar.edu/models/ccsm3.0/pop., —2002—.

[88] SMITH, T. M. and REYNOLDS, R. W., "Improved extended reconstruction of sst (1854-1997)," *Journal Of Climate*, vol. 17, no. 12, pp. 2466–2477, —2004—.

[89] SMITH, W. H. F. and SANDWELL, D. T., "Bathymetric prediction from dense satellite altimetry and sparse shipboard bathymetry," *Journal Of Geophysical Research-Solid Earth*, vol. 99, no. B11, pp. 21803–21824, —1994—.

[90] SONG, Y. and HAIDVOGEL, D. B., "A semi-implicit ocean circulation model using a generalized topography-following coordinate system," *J. Comp. Phys.*, vol. 115, no. 1, pp. 228–244, —1994—.

[91] SPILLANE, M. C., ENFIELD, D. B., and ALLEN, J. S., "Intraseasonal oscillations in sea-level along the west-coast of the america," *Journal of Physical Oceanography*, vol. 17, no. 3, pp. 313–325, —1987—.

[92] STABENO, P. J., BOND, N. A., HERMANN, A. J., KACHEL, N. B., MORDY, C. W., and OVERLAND, J. E., "Meteorology and oceanography of the northern gulf of alaska," *Continental Shelf Research*, vol. 24, no. 7-8, pp. 859–897, —2004—.

[93] STABENO, P. J. and HERMANN, A. J., "An eddy-resolving model of circulation on the western gulf of alaska shelf .2. comparison of results to oceanographic observations," *Journal of Geophysical Research-Oceans*, vol. 101, no. C1, pp. 1151–1161, —1996—.

[94] STRUB, P. T. and JAMES, C., "Altimeter-derived surface circulation in the large-scale ne pacific gyres. part 1. seasonal variability," *Progress in Oceanography*, vol. 53, no. 2-4, pp. 163–183, —2002—.

[95] STRUB, P. T., MESIAS, J. M., MONTECINO, V., RUTLLANT, J., and SALINAS, S., "Coastal ocean circulation off western south america," *The Sea, vol. 11, edited by A. R. Robinson and K. H. Brink, pp. 273- 313, John Wiley, New York*, —1998—.

[96] SVERDRUP, H., JOHNSON, M., and FLEMING, R., "The oceans, their physics, chemistry, and general biology.," *Prentice-Hall Inc.*, —1942—.

[97] TABATA, S., "The anticyclonic, baroclinic eddy off sitka, alaska, in the northeast pacific-ocean," *Journal of Physical Oceanography*, vol. 12, no. 11, pp. 1260–1282, —1982—.

[98] THOMAS, A. C., "Seasonal distributions of satellite-measured phytoplankton pigment concentration along the chilean coast," *Journal of Geophysical Research*, vol. 104, no. C11, pp. 25877–25890, —1999—.

[99] THOMSON, R. E. and GOWER, J. F. R., "A basin-scale oceanic instability event in the gulf of alaska," *Journal Of Geophysical Research-Oceans*, vol. 103, no. C2, pp. 3033–3040, —1998—.

[100] ULLOA, O., ESCRIBANO, N., HORMAZABAL, S., QUINONES, R. A., GONZA-LEZ, R. R., and RAMOS, M., "Evolution and biological effects of the 1997-98 el nino in the upwelling ecosystem off northern chile," *Geophysical Research Letters*, vol. 28, no. 8, pp. 1591–1594, —2001—.

[101] UPPALA, S. M., KALLBERG, P. W., SIMMONS, A. J., ANDRAE, U., BECH-TOLD, V. D., FIORINO, M., GIBSON, J. K., HASELER, J., HERNANDEZ, A., KELLY, G. A., LI, X., ONOGI, K., SAARINEN, S., SOKKA, N., ALLAN, R. P., ANDERSSON, E., ARPE, K., BALMASEDA, M. A., BELJAARS, A. C. M., VAN DE BERG, L., BIDLOT, J., BORMANN, N., CAIRES, S., CHEVALLIER, F., DETHOF, A., DRAGOSAVAC, M., FISHER, M., FUENTES, M., HAGE-MANN, S., HOLM, E., HOSKINS, B. J., ISAKSEN, L., JANSSEN, P., JENNE, R., MCNALLY, A. P., MAHFOUF, J. F., MORCRETTE, J. J., RAYNER, N. A., SAUNDERS, R. W., SIMON, P., STERL, A., TRENBERTH, K. E., UNTCH, A., VASILJEVIC, D., VITERBO, P., and WOOLLEN, J., "The era-40 re-analysis," *Quarterly Journal of the Royal Meteorological Society*, vol. 131, no. 612, pp. 2961–3012, —2005—.

[102] VENRICK, E. L., "Floral patterns in the california current system off southern california: 1990-1996," *Journal of Marine Research*, vol. 60, no. 1, —2002—.

[103] WARE, D. M. and THOMSON, R. E., "Bottom-up ecosystem trophic dynamics determine fish production in the northeast pacific," *Science*, vol. 308, no. 5726, pp. 1280–1284, —2005—.

[104] WHITNEY, F. and ROBERT, M., "Structure of haida eddies and their trans-port of nutrient from coastal margins into the ne pacific ocean," *Journal Of Oceanography*, vol. 58, no. 5, pp. 715–723, —2002—.